American University in Cairo
AUC Knowledge Fountain

Theses and Dissertations

6-1-2017

Plasmonic waveguides and nano-antennas for optical communications

Mai Osama Sallam

Follow this and additional works at: https://fount.aucegypt.edu/etds

Recommended Citation

APA Citation
Sallam, M. (2017).*Plasmonic waveguides and nano-antennas for optical communications* [Master's thesis, the American University in Cairo]. AUC Knowledge Fountain.
https://fount.aucegypt.edu/etds/26

MLA Citation
Sallam, Mai Osama. *Plasmonic waveguides and nano-antennas for optical communications*. 2017. American University in Cairo, Master's thesis. *AUC Knowledge Fountain*.
https://fount.aucegypt.edu/etds/26

This Dissertation is brought to you for free and open access by AUC Knowledge Fountain. It has been accepted for inclusion in Theses and Dissertations by an authorized administrator of AUC Knowledge Fountain. For more information, please contact mark.muehlhaeusler@aucegypt.edu.

THE AMERICAN UNIVERSITY IN CAIRO
الجامعة الأمريكية بالقاهرة

School of Sciences and Engineering

Applied Sciences

Nanotechnology

KU LEUVEN

Arenberg Doctoral School

Faculty of Engineering Science

Department of Electrical Engineering

Plasmonic Waveguides and Nano-Antennas for Optical Communications

Mai Sallam

Supervisors:
Prof. Dr. Ezzeldin A. Soliman
Prof. Dr. Guy A. E. Vandenbosch
Co-Supervisor:
Prof. Dr. Georges Gielen

Dissertation presented in partial fulfilment of the requirements for the degree of Doctor of Applied Science: Nanotechnology (AUC), and Doctor of Engineering Science: Electrical Engineering (KU Leuven)

April 2017

Plasmonic Waveguides and Nano-Antennas for Optical Communications

Mai Sallam

Supervisors:
Prof. Dr. Ezzeldin A. Soliman
Prof. Dr. Guy A. E. Vandenbosch
Co-Supervisor:
Prof. Dr. Georges Gielen

Members of the Examination Committee:
Prof. Dr. Amr Shaarawi (AUC)
Prof. Dr. Alaa Abdelmageed (Cairo University)
Assoc. Prof. Dr. Mohamed Swillam (AUC)
Prof. Dr. Stefan Vandewalle (KUL)
Dr. Vladimir Volskiy (KUL)

Dissertation presented in partial fulfillment of the requirements for the degree of Doctor of Applied Science: Nanotechnology (AUC), and Doctor of Engineering Science: Electrical Engineering (KUL)

April 2017

To my family, mentors, and friends

Acknowledgements

Foremost, I am incessantly thankful and indebted to Allah for guiding and supporting me all the time. No words would ever be enough to express my gratitude.

With my greatest pleasure, I would like to express my sincere appreciation to my advisors Prof. Dr. Ezzeldin Soliman, Prof. Dr. Guy Vandenbosch, and Prof. Dr. Georges Gielen.

I am deeply grateful to Prof. Soliman for the patient guidance, endless support, continuous motivation, and being an extraordinary advisor. Since I joined his research group at AUC in 2008, I learnt a lot from his immense knowledge and invaluable experience. The enthusiasm and dedication he has for research is extremely inspiring. I am also very thankful to him for his confidence and persistence to tackle research challenges faced throughout the Ph.D. journey which has led to a fruitful research outcome. Prof. Soliman profoundly affected my academic life, where he invested in me lots of his time, and experience. He has the credit for introducing me to Prof. Vandenbosch and establishing the collaboration between AUC and KU Leuven. No words would ever be enough to express my indebtedness to him for such great efforts throughout the past years.

My sincere appreciation is due to Prof. Vandenbosch who gave me the great chance to join his research group at KU Leuven. Since the first day, I benefited a lot from his very wide experience and continuous guidance. The regular meetings we had were very constructive where each time I learnt something new. I am extremely inspired by his dynamism, vision, and methodology to overcome any challenge. Prof. Vandenbosch has never saved any time or efforts towards advising or helping me very promptly. His very welcoming personality and sense of humour are unforgettable.

I would like to express my thankfulness to Prof. Gielen for his efforts, motivation, and giving me the opportunity to spend an extra year at KU Leuven and benefit from the research facilities there.

Many thanks are due to Prof. Dr. Femius Koenderink (FOM Institute, AMOLF) and Dr. Xuezhi Zheng (KU Leuven) for their remarkable efforts in the fabrication and characterization of the wire-grid nano-antennas, which is a crucial part of this research.

I would also like to offer my special thanks to my examination committee members: Prof. Dr. Amr Shaarawi, Prof. Dr. Alaa Abdelmageed, Assoc. Prof. Dr. Mohamed Swillam, Prof. Dr. Stefan Vandenwalle, and Dr. Vladimir Volskiy for their time, and efforts in revising my thesis. They provided me with very constructive feedback, helpful comments and insightful questions. I am very much thankful to Dr. Volskiy for his enormous help and significant efforts with me during the time I spent at KU Leuven.

I wish also to express my deep thanks to all my professors who played a major role in my academic life. I would like to address a special thanks to Prof. Dr. Sherif Sedky for his invaluable help, guidance and for introducing me to Prof. Soliman at the early stage of my graduate studies. Regardless of being very busy, Prof. Sedky is very helpful and continually provides me with his sincere advice.

I would like to extend my thankfulness to my colleagues and friends at both AUC and KU Leuven for their support and for the very nice time we spent together. Special thanks to my friends: Huda Alaa, Enas Kandil, Sarah El Shal, and Huda Alkhezaimy.

I would like to acknowledge Mr. Yousef Jameel for the fellowship I obtained during my study at AUC. I would also like to thank FWO foundation for their support during my study at KU Leuven.

My deepest heartfelt appreciation goes to my parents. I am indebted to them for the extraordinary efforts they are constantly exerting with me. Their endless confidence, care, support and prayers are always surrounding me. I was very pleased with their companion when they visited me in Leuven during my study. I would hardly be able to achieve any success without them. I warmly thank my sister Menna and her family for being in my life. My deepest thanks go to my nephews Ahmed and Maya Bahaa, who have a special clue to boost my mood especially at the hardest times.

Finally, I would like to thank all who contributed directly or indirectly in bringing this thesis into completion. I would like to apologize if I was not able to mention all of them in person.

Mai Osama Sallam

April 2017

Abstract

The field of plasmonics has received great attention during the past years. Plasmonic devices are characterized by their small electrical size which enabled researchers to overcome the challenge of the size mismatch between the bulky photonic devices and the small electronic circuits. Plasmonic metals are characterized by their lossy dielectric nature which is different from the highly conductive classical metals. Consequently, the design of plasmonic devices necessitates upgrading the existing solvers to take into consideration their material properties at the optical frequency range. In this thesis, a plasmonic transmission line mode solver is developed in which the propagation characteristics of plasmonic transmission lines/waveguides are calculated. More specifically, the solver calculates the propagation constant, losses, and mode profile(s) of the propagating mode(s). The transmission lines can have any topology and are assumed to be placed within a stack of flat layers. The solver is developed using the Method of Moments technique which is characterized by its tremendously decreased number of unknowns compared to the finite element/difference methods leading to much faster calculation time. The solver is tested on several plasmonic transmission lines of various topologies, number of metallic strips and/or surrounding media. These transmission lines include rectangular strip, circular strip, triangular strip, U-shaped strip, horizontally coupled strips, and vertically coupled strips. The obtained results are compared with those calculated by the commercial tool “CST”. Very good agreement between both solvers is achieved. The second line presented within this thesis is concerned with the design of plasmonic wire-grid nano-antenna arrays. The basic element of this array is a nano-rod, whose propagation characteristics are first obtained using the developed solver. The arrays are then optimized using “CST”. Within the context of this thesis, three nano-antenna arrays are proposed: a five-element wire-grid array, an eleven-element wire-grid array, and a novel circularly polarized wire-grid array. All of these arrays have high directivity and are suitable for inter-/intra-chip optical communication, where they replace the losing transmission lines.

Samenvatting

Het onderzoeksgebied “plasmonics” heeft de laatste jaren grote aandacht gekregen. Plasmonische devices worden gekarakteriseerd door hun kleine elektrische afmetingen, hetgeen onderzoekers toelaat om de dimensionele mismatch tussen vrij grote photonische devices en kleinere elektronische circuits aan te pakken. Plasmonisch metaal wordt gekarakteriseerd door verliezen, die anders zijn dan bij de hooggeleidende klassieke metalen. Bijgevolg is het bij het ontwerp van plasmonische devices nodig om de bestaande ontwerptools te upgraden zodanig dat de materiaaleigenschappen in rekening kunnen gebracht worden in het optische frequentiebereik. In deze thesis wordt een plasmonische transmissielijnsolver ontwikkeld waarbij de propagatiekarakteristieken van plasmonische golfgeleiders worden berekend. Meer specifiek, de solver berekent de propagatieconstante, de verliezen, en het modale profile van de propagerende mode(s). De solver werd ontwikkeld gebruik makende van de momentenmethode en werd getest op verscheidene plasmonische transmissielijnen, onder andere de rechthoekige strip, de circelvormige strip, de driehoekige strip, de U-gevormde strip, horizontale gekoppelde en verticaal gekoppelde strips. De verkregen resultaten worden vergeleken met de resultaten van de commerciele tool “CST”. Een zeer goede overeenkomst wordt bereikt. De tweede researchlijn in deze thesis betreft het ontwerp van plasmonische nano-antenneroosters met als basiselement de nano-rod. De roosters worden eerst ontwerpen aan de hand van de ontworpen solver en worden dan geoptimaliseerd met “CST”. Binnen de context van deze thesis worden drie nano-antenneroosters voorgesteld: een vijf-elementenrooster, een elf-elementenrooster, en een zeer innoverend circulair gepolariseerd rooster. Al deze roosters hebben een hoge directiviteit en zijn geschikt voor inter-/intra-chip optische communicatie, waar ze de verlieslatende transmissielijnen vervangen.

Publication List

Thesis Publications

International Journals

- **M. O. Sallam**, G. A. E. Vandenbosch, G. Gielen, and E. A. Soliman, "Generalized Mode Solver for Plasmonic Transmission Lines Embedded in Layered Media based on the Method of Moments," *Journal of Applied Physics* (submitted).

- **M. O. Sallam**, G. A. E. Vandenbosch, G. Gielen, and E. A. Soliman, "Novel Wire-Grid Nano-Antenna Array with Circularly Polarized Radiation for Wireless Optical Communication Systems," *Plasmonics* (submitted).

- K. Guo, A. Antoncecchi, X. Zheng, **M. O. Sallam**, E. A. Soliman, G. A. E. Vandenbosch, V. V. Moschalkov, and A. F. Koenderink, "Dendritic Optical Antennas," *Scientific Reports* (submitted).

- E. A. Soliman, **M. O. Sallam**, and G. A. E. Vandenbosch, "Plasmonic Grid Array of Gold Nanorods for Point-to-Point Optical Communications," *IEEE Journal of Lightwave Technology*, vol. 32, no. 24, pp. 4296 – 4302, December 2014.

- **M. O. Sallam**, G. A. E. Vandenbosch, G. Gielen, and E. A. Soliman, "Integral Equations Formulation of Plasmonic Transmission Lines," *Optics Express*, vol. 9, no. 19, pp. 22388 – 22402, September 2014.

International Conferences

- **M. O. Sallam**, G. A. E. Vandenbosch, G. Gielen, and E. A. Soliman, "Wire Grid Nanoantenna Array with Parasitic Radiators for Optical Telecommunication Applications," *Proceedings from 2016 SPIE Photonics Europe*, Brussels, Belgium, April 2016.

- **M. O. Sallam**, G. A. E. Vandenbosch, G. Gielen, and E. A. Soliman, "Plasmonic Transmission Line Mode Solver Based on the Method of Moments," *9th European Conference on Antennas and Propagation (EuCAP)*, Lisbon, Portugal, April 2015.

- E. A. Soliman, **M. O. Sallam**, and G. A. E. Vandenbosch, "Novel Wire-Grid Nantenna Array for Optical Communication Systems," *IEEE International Workshop on Antenna Technology (IWAT)*, Karlsruhe, Germany, March 2013.

Other Publications

International Journals

- **M. O. Sallam**, S. M. Kandil, V. Volski, G. A. E. Vandenbosch, and E. A. Soliman, "Wideband CPW-Fed Flexible Bow-tie Slot Antenna for WLAN/WiMax Systems," *IEEE Transactions on Antennas and Propagation* (Accepted).

- **M. O. Sallam**, M. Serry, S. Sedky, A. Shamim, W. De Raedt, G. A. E. Vandenbosch, and E. A. Soliman, "Micromachined On-Chip Dielectric Resonator Antenna Operating at 60 GHz," *IEEE Transactions on Antennas and Propagation*, vol. 63, no. 8, pp. 3410 – 3416, August 2015.

- **M. O. Sallam**, E.A. Soliman, G. A. E. Vandenbosch, and W. De Raedt, "Novel Electrically Small Meander Line RFID Tag Antenna," *International Journal of RF and Microwave Computer-Aided Engineering*, vol. 23, no.6, pp. 639 – 645, November 2012.

- E. A. Soliman, **M. O. Sallam**, W. De Raedt, and G. A. E. Vandenbosch, "Miniaturized RFID Antenna Operating at 915 MHz," *IEEE Antennas and Wireless Propagation Letters*, vol. 11, pp. 1068 – 1071, August 2012.

International Conferences

- **M. O. Sallam**, S. M. Kandil, V. Volski, G. A. E. Vandenbosch, "2.4/5 GHz WLAN Crescent Antenna on Flexible Substrate," *10thEuropean Conference on Antennas and Propagation (EuCAP)*, Davos, Switzerland, April 2016.

- **M. O. Sallam**, S. M. Kandil, V. Volski, G. A. E. Vandenbosch, "Flexible Bow-Tie Antenna for WLAN/Wi-Max Applications," *10th European Conference on Antennas and Propagation (EuCAP)*, Davos, Switzerland, April 2016.

- **M. O. Sallam**, G. A. E. Vandenbosch, W. De Raedt, and E. A. Soliman, "Electrically Small Antennas with Dimensions down to One-Fifteenth and One-Thirtieth of Wavelength," *IEEE Antennas and Propagation Symposium (AP-S)*, Vancouver, Canada, July 2015.

- **M. O. Sallam**, M. Serry, S. Sedky, A. Shamim, W. De Raedt, G. A. E. Vandenbosch, and E. A. Soliman, "High Efficiency On-Chip Dielectric Resonator Antenna using Micromachining Technology," *IEEE Antennas and Propagation Symposium (AP-S)*, Vancouver, Canada, July 2015."

Table of Contents

Acknowledgements iv
Abstract vi
Samenvatting vii
Publication List viii
List of Symbols xiii
List of Acronyms xviii
List of Figures xix
List of Tables xxvi
Chapter 1: Introduction 1
1.1 Classical versus Plasmonics Metals 2
1.1.1 Material Properties 2
1.1.2 Surface versus Volumetric Current 4
1.2 Numerical Techniques 4
1.3 Plasmonic Transmission Lines 6
1.4 Plasmonic Nantennas 7
1.5 Scope of the Thesis 9
Chapter 2: Spectral and Spatial Domain Green's Functions 10
2.1 Problem under Investigation 11
2.2 TE and TM Field Decomposition 14
2.2.1 TE System 14
2.2.2 TM System 15
2.3 TE and TM Current Decomposition 16
2.3.1 Conditions on TE Currents 17
2.3.2 Conditions on TM Currents 18
2.3.3 Combined Current Expressions for the TE and TM Systems 18
2.4 Solutions of the TE and TM systems 19
2.4.1 Solution of the TE System 19
2.4.2 Solution of the TM System 21
2.5 Recombination of the TE and TM Systems 23

2.6 Closed-Form Spectral Domain Green's Functions of Frequently used Layered Media 25
2.6.1 Source Located in Homogeneous Medium 25
2.6.2 Source Surrounded by Top and Bottom Layered Media 25
2.6.3 Half-Space/Source Carrying Layer/Half-Space 29
2.7 Spatial Domain Green's Functions 36
2.8 Conclusions 43
Chapter 3: Formulation of the Method of Moments 45
3.1 Electric Field in terms of Electric Current 46
3.2 Electric Current Expansion 46
3.3 Impedance Matrix Elements 48
3.4 Boundary Conditions along the Metallic Strips 53
3.5 Conclusions 58
Chapter 4: Numerical Examples for Plasmonic Transmission Lines 59
4.1 Plasmonic Transmission Lines in Homogeneous Medium 60
4.1.1 Single Rectangular Strip 60
4.1.2 Horizontally Coupled Strips 62
4.1.3 Vertically Coupled Strips 63
4.1.4 Triangular and Circular Strips 65
4.2 Plasmonic Transmission Lines at the Interface of Two Half-Spaces 66
4.2.1 Single Strip on Top of SiO_2 Substrate 67
4.2.2 Horizontally Coupled Strips on Top of SiO_2 Substrate 69
4.2.3 U-shaped Strip on Top of SiO_2 substrate 70
4.3 Plasmonic Nano-Strip on Top of SiO_2 Layer Backed with Au Ground Layer 71
4.4 Plasmonic Nano-Strip Embedded in SiO_2 Layer Backed with Thick ITO Layer 72
4.5. Conclusions 73
Chapter 5: Plasmonic Nano-Antennas 74
5.1 Wire-Grid Nano-Antenna in Free-Space 75
5.1.1 Reference Dipole Nano-Antenna 76
5.1.2 Structure of the Wire-Grid Nano-Antenna Array 79
5.1.3 Modal Field Distribution along the Wire-Grid Array 81
5.1.4 Radiation Characteristics of the Wire-Grid Array 81
5.1.5 Effect of Adding a Substrate underneath the Wire-Grid Array 82

5.2 Wire-Grid Nano-Antennas on Top of Finite SiO_2 Backed by Plasmonic Metal Layer 83
5.2.1 Single Nano-Dipole Antenna 85
5.2.2 Eleven-Element Wire-Grid Nano-Antenna Array 86
5.2.3 Circularly Polarized Wire-Grid Nano-Antenna Array 90
5.3 Fabrication and Measurements 95
5.4 Conclusions 99
Chapter 6: Conclusions and Future Work 101
6.1 Summary of the Thesis 101
6.2 Future Work 104
Bibliography 106

List of Symbols

Symbol	*Description*
A_{cell}	Area of a unit cell of an array of wire-grid nano-antenna
$a_n\left(a_m\right)$	*x*- centre of the *x*-directed electric current basis (test) function
A_n, B_n, C_n	Expansion coefficients (weights) of the *x*-directed, *y*-directed, and *z*-directed electric current basis functions.
$[A],[B],[C]$	Vector of the expansion coefficient of the *x*-directed, *y*-directed, and *z*-directed electric current densities
$\underline{B}_i$	Magnetic flux density at i^{th} layer
$b_n\left(b_m\right)$	*z*- centre of the *x*-directed electric current basis (test) function
$c_n\left(c_m\right)$	*x*- centre of the *y*-directed electric current basis (test) function
$\underline{D}_i$	Electric flux density at i^{th} layer
$d_n\left(d_m\right)$	*z*- centre of the *y*-directed electric current basis (test) function
$\underline{E}_i$	Spatial domain electric field at i^{th} layer
E_x, E_y, E_z	*x*-, *y*-, and *z*- components of the electric field
E_{zi}^{+}, E_{zi}^{-}	Independent expansion coefficients of the electric field in the ith layer
$ET(u)$	Even triangular function
$ET'(u)$	Derivative of the even triangular function
$e_n\left(e_m\right)$	*x*- centre of the *z*-directed electric current basis (test) function
$f_n\left(f_m\right)$	*z*- centre of the *z*-directed electric current basis (test) function
$G\left(\tilde{G}\right)$	Spatial (Spectral) domain Green's function
$\tilde{G}_{ij}^{E_\ell, J_\ell'}\left(G_{ij}^{E_\ell, J_\ell'}\right)$	Spectral (Spatial) domain Green's function describing a lateral electric field component on the ith interface due to the derivative of the lateral electric current filament on the jth interface.
$\tilde{G}_{ij}^{E_\ell, J_z}\left(G_{ij}^{E_\ell, J_z}\right)$	Spectral (Spatial) domain Green's function describing a lateral electric field component on the ith interface due to a *z*-directed electric current filament on the jth interface.

$\tilde{G}_{ij}^{E_z,J'_\ell}\left(G_{ij}^{E_z,J'_\ell}\right)$	Spectral (Spatial) domain Green's function describing a *z*-directed electric field component on the ith interface due to the derivative of the lateral electric current filament on the jth interface.
$\tilde{G}_{ij}^{E_z,J_z}\left(G_{ij}^{E_z,J_z}\right)$	Spectral (Spatial) domain Green's function describing a *z*-directed electric field component on the ith interface due to *z*-directed electric current filament on the jth interface.
$\tilde{G}_{ij}^{E_z,J'_z}\left(G_{ij}^{E_z,J'_z}\right)$	Spectral (Spatial) domain Green's function describing a *z*-directed electric field component on the ith interface due to the derivative of a *z*-directed electric current filament on the jth interface.
$\tilde{G}_{ij}'^{E_\ell,J'_z}$	Derivative of the spectral domain Green function $\tilde{G}_{ij}^{E_\ell,J'_z}$ with respect to *z*.
$\tilde{G}_{ij}'^{E_z,J'_\ell}$	Derivative of the spectral domain Green function $\tilde{G}_{ij}^{E_z,J'_\ell}$ with respect to *z*.
$\tilde{G}_{ij}'^{E_z,J_z}$	Spectral domain Green's function given by the equation: $\tilde{G}_{ij}'^{E_z,J_z} = \tilde{G}_{ij}^{E_z,J_z} + \dfrac{\partial^2 \tilde{G}_{ij}^{E_z,J'_z}}{\partial z^2}$
k_0	Free-space propagation constant $k_0 = \omega\sqrt{\mu_0\varepsilon_0}$
K_0	Modified Bessel function of second kind and zero order
k_x	Spectral counterpart of the spatial variable *x*
k_y	Spectral counterpart of the spatial variable *y*
k_{zi}	Propagation constant along the direction of stratification for the ith layer
k_ρ	Spectral counterpart of the spatial variable ρ
$\underline{H}_i$	Spatial domain magnetic field at i^{th} layer
H_x, H_y, H_z	*x*-, *y*-, and *z*- components of the magnetic field
H_{zi}^+, H_{zi}^-	Independent expansion coefficients of the magnetic field in the ith layer
$\text{Im}(n)$	Imaginary part of the complex refractive index of a metal
J_x, J_y, J_z	*x*-, *y*-, and *z*- components of the electric current density
$LT(u)$	Left-sided triangular function
$LT'(u)$	Derivative of the left-sided triangular function
N	Number of terms required to approximate a function $f(t)$ using the DCIM method
N_{p1}	Number of samples along the first level of the DCIM
N_{p2}	Number of samples along the second level of the DCIM

N_x, N_y, N_z	Number of basis functions used to approximate the *x*-directed, *y*-directed, and *z*-directed electric current densities of a metallic strip
$RT(u)$	Right-sided triangular function
$RT'(u)$	Derivative of the right-sided triangular function
$T(f)$	Transmittance of an array of nano-antennas as function of frequency
$T(u)$	Triangular function of the basis or test functions
$T_{ref}(f)$	Transmittance of the substrate without the presence of the antenna as function of frequency
$[W]$	Vector of the expansion coefficient of the electric current densities of the metallic strip(s)
w_n	Coefficient term of the nth exponential of the approximated Green's function using the DCIM method
x, y, z	Spatial co-ordinates of an observation point
x', y', z'	Spatial co-ordinates of a source point
(x_n, z_n)	The (*x*,*z*) location of the current basis function
(x_m, z_m)	The (*x*,*z*) location of the current test function
(x'_j, z'_j)	Domain of the current distribution in the *xz*-plane along the cross-section of the jth strip
$[Z_{xx}]$	Impedance matrix (coupling matrix) which describes the *x*- directed electric field due to an *x*- directed electric current density.
$[Z_{xy}]$	Impedance matrix (coupling matrix) which describes the *x*- directed electric field due to a *y*- directed electric current density.
$[Z_{xz}]$	Impedance matrix (coupling matrix) which describes the *x*- directed electric field due to a *z*- directed electric current density.
$[Z_{yx}]$	Impedance matrix (coupling matrix) which describes the *y*- directed electric field due to an *x*- directed electric current density.
$[Z_{yy}]$	Impedance matrix (coupling matrix) which describes the *y*- directed electric field due to a *y*- directed electric current density.
$[Z_{yz}]$	Impedance matrix (coupling matrix) which describes the *y*- directed electric field due to a *z*- directed electric current density.
$[Z_{zx}]$	Impedance matrix (coupling matrix) which describes the *z*- directed electric field due to an *x*- directed electric current density.
$[Z_{zy}]$	Impedance matrix (coupling matrix) which describes the *z*- directed electric field due to a *y*- directed electric current density.
$[Z_{zz}]$	Impedance matrix (coupling matrix) which describes the *z*- directed electric field

	due to a *z*- directed electric current density.
$[Z'_{xx}]$	Impedance matrix (coupling matrix) used to describe the *x*- directed electric field of the ith plasmonic strip due to an *x*- directed electric current density of the same strip.
$[Z'_{yy}]$	Impedance matrix (coupling matrix) used to describe the *y*- directed electric field of the ith plasmonic strip due to a *y*- directed electric current density of the same strip.
$[Z'_{zz}]$	Impedance matrix (coupling matrix) used to describe the *z*- directed electric field of the ith plasmonic strip due to a *z*- directed electric current density of the same strip.
α	Attenuation constant
α_n	Exponent term of the nth exponential of the approximated Green's function using the DCIM method
β	Lateral spectral value
β_1	Maximum lateral spectral value of the first level of the DCIM
β_2	Minimum (Maximum) lateral spectral value of the first (second) level of the DCIM
β_3	Minimum lateral spectral value of the second level of the DCIM
γ	Collision rate
γ_i	Spectral propagation constant in the direction of the stratification $\gamma_i = \sqrt{\beta_i^2 - \omega^2 \mu_i \varepsilon_i}$
Γ_i^{TE}	Reflection coefficient along the direction of stratification along the ith layer for the TE system
Γ_i^{TM}	Reflection coefficient along the direction of stratification along the ith layer for the TM system
δ	Skin depth / Dirac Delta function
Δ_x, Δ_z	Separation between the source and observation points along the *x*-and *z*- axes.
ε_∞	Epsilon at infinite frequency for plasmonic metals
ε_0	Free-space dielectric constant
ε_i	Dielectric permittivity at i^{th} layer or the ith strip
$\hat{\varepsilon}_r$	Relative dielectric permittivity
$\hat{\varepsilon}_{ri}$	Relative dielectric permittivity of the ith plasmonic strip
$\hat{\varepsilon}_{rb}$	Relative dielectric permittivity of the background medium surrounding the ith plasmonic strip

$\hat{\varepsilon}_{r,eff}$	Effective dielectric constant
ε'	Real component of the dielectric permittivity
ε''	Imaginary component of the dielectric permittivity
λ	Wavelength
λ_0	Free-space wavelength
λ_g	Guided wavelength
μ_0	Dielectric permeability of free-space
μ_i	Dielectric permeability at i^{th} layer or i^{th} strip
σ_{ext}	Extinction cross-section
ω	Radial frequency
ω_c	Collision frequency
ω_p	Plasma frequency
$\underline{\nabla}\cdot$	Divergence operator
$\underline{\nabla}\times$	Curl operator

List of Acronyms

Ag	Silver
Al	Aluminium
A.R.	Axial Ratio
Au	Gold
CPS	Coupled Strips
Cu	Copper
DCIM	Discrete Complex Image Method
EIM	Effective Index Method
FDFD	Finite Difference Frequency Domain
FDTD	Finite Difference Time Domain
FEM	Finite Element Method
GPOF	Generalized Pencil Of Function
HEM	Horizontal Electric Dipole
HMD	Horizontal Magnetic Dipole
IL	Insertion Loss
ITO	Indium-Tin Oxide
LHCP	Left-Hand Circular Polarization
LRSPP	Long Range Surface Plasmon Polariton
MAGMAS	Model for the Analysis of General Multilayered Antenna Structures
MoL	Method of Lines
MoM	Method of Moments
PML	Perfectly Matched Layers
Pt	Platinum
RF	Radio Frequency
RHCP	Right-Hand Circular Polarization
SEM	Scanning Electron Microscope
SiO_2	Silicon Dioxide
SPP	Surface Plasmon Polariton
SVD	Singular Value Decomposition
TE	Transverse Electric System
THz	Terahertz
TM	Transverse Magnetic System
VED	Vertical Electric Dipole
VMD	Vertical Magnetic Dipole

List of Figures

Figure 1.1: Surface Plasmon Polariton propagating along the interface between metal and dielectric media [6]..... 2

Figure 1.2: The relative dielectric permittivity functions versus wavelength for plasmonic metals at optical frequencies: (a) real part, and (b) imaginary part..... 4

Figure 1.3: Examples of different fabricated nano-antenna topologies including dipole, bow-tie antennas [49]..... 8

Figure 2.1: Generalized plasmonic transmission line made up of a number of metallic strips with arbitrary cross-section and dimensions, immersed within a stack of flat dielectric or metallic layers. 11

Figure 2.2: Unit current source located at the interface of the layers *j*, and *j*+1..... 12

Figure 2.3: Summary for the inward and outward recurrence techniques used to calculate the spectral domain coefficients of the TE system. 21

Figure 2.4: Summary for the inward and outward recurrence techniques used to calculate the spectral domain coefficients of the TM system. 23

Figure 2.5: Current source located at the interface of two half-spaces. 27

Figure 2.6: The basic Green's function g^{E_ℓ, J_ℓ} for a source located at the interface of two half-spaces (free-space and SiO_2): blue (real part), and red dashed (imaginary part)..... 27

Figure 2.7: The basic Green's function $g^{E_\ell, J_\ell'}$ for a source located at the interface of two half-spaces (free-space and SiO_2): blue (real part), and red dashed (imaginary part)..... 27

Figure 2.8: The basic Green's functions: $g^{E_\ell, J_z'}$, $g^{E_z, J_z'}$ for a source located at the interface of two half-spaces (free-space and SiO_2): blue (real part), and red dashed (imaginary part)..... 28

Figure 2.9: The basic Green's functions: $g^{E_z, J_\ell'}$ for a source located at the interface of two half-spaces (free-space and SiO_2): blue (real part), and red dashed (imaginary part)..... 28

Figure 2.10: The basic Green's functions: g^{E_z, J_z} for a source located at the interface of two half-spaces (free-space and SiO_2): blue (real part), and red dashed (imaginary part)..... 28

Figure 2.11: Current source located at the top layer of a three-layered medium structure..... 29

Figure 2.12: Current source located at the middle layer of a three-layered medium structure. 30

Figure 2.13: The basic Green's functions for a source located in the middle layer of three-layered structure (free-space/SiO_2/ITO) (a) $g_1^{E_\ell,J_\ell}$, (b) $g_2^{E_\ell,J_\ell}$, (c) $g_3^{E_\ell,J_\ell}$, and (d) $g_4^{E_\ell,J_\ell}$: blue (real part), and red dashed (imaginary part). 32

Figure 2.14: The basic Green's functions for a source located in the middle layer of three-layered structure (free-space/SiO_2/ITO) (a) $g_1^{E_\ell,J'_\ell}$, (b) $g_2^{E_\ell,J'_\ell}$, (c) $g_3^{E_\ell,J'_\ell}$, and (d) $g_4^{E_\ell,J'_\ell}$: blue (real part), and red dashed (imaginary part). 33

Figure 2.15: The basic Green's functions for a source located in the middle layer of three-layered structure (free-space/SiO_2/ITO) (a) $g_1^{E_\ell,J'_z}\left(g_1^{E_z,J'_z}\right)$, (b) $g_2^{E_\ell,J'_z}\left(g_2^{E_z,J'_z}\right)$, (c) $g_3^{E_\ell,J'_z}\left(g_3^{E_z,J'_z}\right)$, and (d) $g_4^{E_\ell,J'_z}\left(g_4^{E_z,J'_z}\right)$: blue (real part), and red dashed (imaginary part). 34

Figure 2.16: The basic Green's functions: for a source located in the middle layer of three-layered structure (free-space/SiO_2/ITO) (a) $g_1^{E_z,J'_\ell}$, (b) $g_2^{E_z,J'_\ell}$, (c) $g_3^{E_z,J'_\ell}$, and (d) $g_4^{E_z,J'_\ell}$: blue (real part), and red dashed (imaginary part). 35

Figure 2.17: The basic Green's functions: for a source located in the middle layer of three-layered structure (free-space/SiO_2/ITO) (a) $g_1^{E_z,J_z}$, (b) $g_2^{E_z,J_z}$, (c) $g_3^{E_z,J_z}$, and (d) $g_4^{E_z,J_z}$: blue (real part), and red dashed (imaginary part). 36

Figure 2.18: Sampling path across the k_ρ - plane using the two-level DCIM. 39

Figure 2.19: Sampling path across the k_{zi} - plane using the two-level DCIM 39

Figure 2.20: Exact and DCIM approximation for the basic Green's function g^{E_ℓ,J_ℓ}: (a) real part, and (b) imaginary part..... 42

Figure 2.21: Spatial domain Green's function G^{E_ℓ,J_ℓ} versus the lateral distance between the source and test points $(x-x')$ at 193.55 THz, $k_y = 8.23\times10^6 - j\,3.14\times10^5$ and $z'=0$. 42

Figure 2.22: Spatial domain Green's function G^{E_ℓ,J'_ℓ} versus the lateral distance between the source and test points $(x-x')$ at 193.55 THz, $k_y = 8.23\times10^6 - j\,3.14\times10^5$ and $z'=0$. 42

Figure 2.23: Spatial domain Green's functions $G^{E_\ell,J'_z}, G^{E_z,J'_z}$ versus the lateral distance between the source and test points $(x-x')$ at 193.55 THz, $k_y = 8.23\times10^6 - j\,3.14\times10^5$ and $z'=0$ 43

Figure 2.24: Spatial domain Green's function G^{E_z,J'_ℓ} versus the lateral distance between the source and test points $(x-x')$ at 193.55 THz, $k_y = 8.23\times10^6 - j\,3.14\times10^5$ and $z'=0$. 43

Figure 2.25: Spatial domain Green's function G^{E_z,J_z} versus the lateral distance between the source and test points $(x-x')$ at 193.55 THz, $k_y = 8.23\times10^6 - j\,3.14\times10^5$ and $z'=0$. 43

Figure 3.1: Basis functions used to expand the unknown modal current: (a) *x*-component, (b) *y*-component, and (c) *z*-component. Blue arrows of J_x and J_z denote full roof-top basis functions while green arrows represent half roof-tops basis functions. 48

Figure 3.2: Functions used to represent the basis functions of the current density: (a) rectangular function, $R(u)$, (b) even triangular function, $ET(u)$, (c) left-sided triangular function, $LT(u)$, and (d) right-sided triangular function $RT(u)$. 48

Figure 3.3: Overlap between the basis function (blue and green lines) and the test function (red dashed line) when the basis function is: (a) rectangular prism, (b) even triangular prism, (c) right-hand sided triangular prism, and (d) left-hand sided triangular prism. 54

Figure 3.4: Different cases describing the overlap between the current basis and test functions along the *x*- or *z*-axis: (a) the basis and test functions have the same centre, and the basis function is represented by an even triangular prism (b) the basis and test functions have the same centre, and the basis function is represented by either a right or left triangular prism, (c) the basis and test functions are shifted with a value of Δ_x or Δ_z, and the basis function is represented by an even triangular prism, (d) the basis and test functions are shifted with a value of Δ_x or Δ_z, and the basis function is represented by a right or left triangular prism, (e) the basis and test functions do not overlap. The red dashed colour corresponds to the test function while the blue (green) solid lines correspond to the basis function. 57

Figure 4.1: Plasmonic transmission lines located in free-space under investigation: (a) single rectangular strip, (b) horizontally coupled strips, (c) vertically coupled strips, (d) triangular strip and (e) circular strip. 60

Figure 4.2: Propagation characteristics versus frequency of the propagating mode along the single gold strip of dimensions W = 50 nm, T = 20 nm: (a) effective refractive index, and (b) insertion loss. 61

Figure 4.3: Skin depth of gold metal versus frequency. 61

Figure 4.4: Modal current distribution of the propagating mode supported by the single gold strip of dimensions W = 50 nm and T = 20 nm at 193.55 THz (λ = 1.55 μm): (a) *x*-component (J_x), (b) *y*-component (J_y), and (c) *z*-component (J_z). 62

Figure 4.5: Modal current distribution of the even mode of the horizontally coupled strips of dimensions W = 50 nm, T = 20 nm, and S = 20 nm at 193.55 THz (λ = 1.55 μm): (a) *x*-component (J_x), (b) *y*-component (J_y), and (c) *z*-component (J_z). 63

Figure 4.6: Modal current distribution of the odd mode of the horizontally coupled strips of dimensions W = 50 nm, T = 20 nm and S = 20 nm at 193.55 THz (λ = 1.55 μm): (a) *x*-component (J_x), (b) *y*-component (J_y), and (c) *z*-component (J_z). 63

Figure 4.7: Propagation characteristics versus frequency of the propagating modes along the horizontally coupled strips of dimensions W = 50 nm, T = 20 nm and S = 20 nm: (a) effective refractive index, and (b) insertion loss. 63

Figure 4.8: Modal current distribution of the even mode of the vertically coupled strips of dimensions W = 50 nm, T = 20 nm, and S = 20 nm at 193.55 THz (λ = 1.55 μm) (a) x-component (J_x), (b) y-component (J_y), and (c) z-component (J_z). 64

Figure 4.9: Modal current distribution of the odd mode of the vertically coupled strips of dimensions W = 50 nm, T = 20 nm, and S = 20 nm at 193.55 THz (λ = 1.55 μm): (a) x-component (J_x), (b) y-component (J_y), and (c) z-component (J_z). 64

Figure 4.10: Propagation characteristics versus frequency of the propagating modes along the vertically coupled strips of dimensions W = 50 nm, T = 20 nm, and S = 20 nm: (a) effective refractive index, and (b) insertion loss. 64

Figure 4.11: Propagation characteristics versus frequency of the propagating modes along the triangular (Tri.) and circular (Cir.) strips of dimensions W = 50 nm, H = 25 nm, and R = 50 nm at 193.55 THz (λ = 1.55 μm): (a) effective refractive index, and (b) insertion loss. 65

Figure 4.12: The various plasmonic transmission lines under investigation: (a) single gold strip on top of SiO_2 substrate, (b) horizontally coupled gold strips on top of SiO_2 substrate, and (c) U-shaped plasmonic gold strip placed on top of SiO_2 substrate. 66

Figure 4.13: Propagation characteristics of a single gold strip of dimensions W = 50 nm and T = 20 nm on top of an infinite silicon dioxide substrate: (a) effective refractive index, and (b) insertion loss. 67

Figure 4.14: Current distribution along the plasmonic gold strip of dimensions W = 50 nm and T = 20 nm above the SiO_2 substrate at 193.55 THz (1.55 μm) as obtained using our solver: (a) x-component (J_x), (b) y-component (J_y), and (c) z-component (J_z). 68

Figure 4.15: The effect of varying the strip width (W) of the plasmonic gold strip on top of the SiO_2 substrate on the propagation characteristics as simulated using the MoM-solver at 193.55 THz (1.55 μm) when the strip thickness T = 20 nm: (a) the effective refractive index, and (b) the insertion loss. 68

Figure 4.16: The effect of varying the strip thickness (T) of the plasmonic gold strip on top of the SiO_2 substrate on the propagation characteristics as simulated using the MoM-solver at 193.55 THz (1.55 μm) when the strip width W = 50 nm: (a) the effective refractive index, and (b) the insertion loss. 68

Figure 4.17: Propagation characteristics of the horizontally coupled gold strips of dimensions W = 50 nm, T = 20 nm, and S = 20 nm on top of an infinite silicon dioxide substrate: (a) effective refractive index, and (b) insertion loss. 69

Figure 4.18: Current distribution of the even-mode along the cross-section of the horizontally coupled gold strips (W = 50 nm, T = 20 nm, and S = 20 nm) on top of SiO_2 substrate at 193.55 THz (1.55 μm) as obtained using the MoM technique(a) x-component (J_x), (b) y-component (J_y), and (c) z-component (J_z). 70

Figure 4.19: Current distribution of the odd-mode along the cross-section of the horizontally coupled gold strips (W = 50 nm, T = 20 nm, and S = 20 nm) on top of SiO_2 substrate at 193.55 THz (1.55

μm) as obtained using the MoM technique: (a) x-component (J_x), (b) y-component (J_y), and (c) z-component (J_z). 70

Figure 4.20: Propagation characteristics of a U-shaped gold strip of dimensions: W = 80 nm, T = 20 nm, W_s = 40 nm, and T_s = 10 nm on top of an infinite silicon dioxide substrate: (a) effective refractive index, and (b) insertion loss..... 70

Figure 4.21: Plasmonic gold nano-strip placed on top of SiO_2 substrate backed by gold ground layer. 71

Figure 4.22: Propagation characteristics of a single gold nano-strip of dimensions W = 50 nm and T = 20 nm on top of a 100 nm thick SiO_2 substrate backed with infinite ground gold layer: (a) effective refractive index, and (b) insertion loss..... 71

Figure 4.23: The effect of varying the SiO_2 substrate thickness on the propagation characteristics of the plasmonic gold nano-strip (W = 50 nm and T = 20 nm) as simulated using the MoM-based solver at 193.55 THz (1.55 μm): (a) the effective refractive index, and (b) the insertion loss. 72

Figure 4.24: Plasmonic gold strip placed inside SiO_2 layer backed by ITO half-space. 72

Figure 4.25: Propagation characteristics of a gold nano-strip of dimensions W = 50 nm and T = 20 nm inside 20 nm thick SiO_2 substrate backed with infinite layer of ITO: (a) effective refractive index, and (b) insertion loss. 73

Figure 5.1: Characteristics of the propagation mode of the single strip plasmonic transmission line versus the width and thickness of the strip at 193.55 THz: (a) guided wavelength (nm), and (b) insertion loss (dB/μm). 75

Figure 5.2: Modal current distribution of the propagating mode supported by the single strip at 193.55 THz: (a) x-component, (b) y-component, and (c) z-component. 76

Figure 5.3: Propagation characteristics versus frequency of the propagating mode along 30×30 nm single strip: (a) guided wavelength, and (b) insertion loss..... 76

Figure 5.4: Single gold nano-rod in free-space. 77

Figure 5.5: z-component of the magnetic field in the xy-plane containing the nano-rod at 193.55 THz (log scale): (a) L_{rad} = 175 nm, (b) L_{rad} = 350 nm, (c) L_{rad} = 525 nm, (d) L_{rad} = 700 nm, and (e) L_{rad} = 875 nm. Dark red and dark blue colours represent maximum positive and maximum negative value, respectively. 77

Figure 5.6: 3D directivity pattern of the 350 nm half-wavelength nano-rod calculated at 193.55 THz using CST. 78

Figure 5.7: Radiation patterns along the principal planes of the 350 nm half-wavelength nano-rod at 193.55 THz simulated using both CST and MAGMAS: (a) E-plane, and (b) H-plane. 79

Figure 5.8: Structure of the wire-grid array of five nano-rods. 80

Figure 5.9: Directivity of the nano-wire-grid array versus L_{rad} and L_{con} calculated using CST at 193.55 THz. 80

Figure 5.10: Distribution of H_z along the *xy*-plane of the optimal wire-grid array at 193.55 THz (log scale): L_{rad} = 350 nm, and L_{con} = 325 nm. 81

Figure 5.11: 3D directivity pattern of the proposed wire-grid array at 193.55 THz, L_{rad} = 350 nm and L_{con} = 325 nm, obtained using CST. 82

Figure 5.12: Radiation patterns along the principal planes of the optimum wire-grid array at 193.55 THz simulated using both CST and MAGMAS: (a) *E*-plane, and (b) *H*-plane. 82

Figure 5.13: Radiation patterns along the principal planes of the optimum wire-grid array at 193.55 THz calculated using MAGMAS for different values of the substrate refractive index: (a) *E*-plane, and (b) *H*-plane. 83

Figure 5.14: Structure of the single nano-rod antenna on top of finite SiO_2 substrate backed by silver layer: (a) zoom-out, and (b) zoom-in. 84

Figure 5.15: Effect of varying the nano-rod width on: (a) guided wavelength, and (b) insertion loss. The thickness of the rod is kept constant at T_{line} = 30 nm, while the thickness of the SiO_2 layer is 150 nm. 84

Figure 5.16: Effect of varying the nano-rod thickness on: (a) guided wavelength, and (b) insertion loss. The width of the rod is either W_{line} = 30 nm or W_{line} = 90 nm, while the thickness of the SiO_2 layer is kept fixed at T_{SiO2} = 150 nm. 85

Figure 5.17: Normal component of the magnetic field (H_z) along the *xy*-plane at T_{SiO2} = 150 nm: (a) W_{rad} = 30 nm, L_{rad} = 377 nm and (b) W_{rad} = 90 nm, L_{rad} = 433.5 nm (log scale). 85

Figure 5.18: 3D directivity patterns of the dipole antenna at T_{SiO2} = 150 nm: (a) W_{rad} = 30 nm, L_{rad} = 377 nm and (b) W_{rad} = 90 nm, L_{rad} = 433.5 nm. 86

Figure 5.19: Eleven-element wire-grid nano-antenna array placed on top of a finite SiO_2 substrate backed by Ag layer: (a) Top-view, and (b) Side-view. 87

Figure 5.20: Normal magnetic field component (H_z) along the *xy*-plane and the corresponding 3D directivity radiation pattern for the wire-grid array at 193.55 THz: (a) H_z at $L_{rad} = L_{con}$ = 370 nm (log scale), (b) directivity at $L_{rad} = L_{con}$ = 370 nm, (c) H_z at $L_{rad} = L_{con}$ = 420 nm (log scale), (d) directivity at $L_{rad} = L_{con}$ = 420 nm. 88

Figure 5.21: (a) Normal component of the magnetic field (H_z) at 193.55 THz (log scale), and (b) the directivity of the optimum 11-elements wire-grid nano-antenna array at 193.55 THz for the optimum 11-element wire-grid array where $L_{rad} = L_{con}$ = 395 nm. 89

Figure 5.22: 2D radiation patterns of the optimum 11-elements wire-grid nano-antenna array at 193.55 THz (a) *E*-plane (Phi = 0°), and (b) *H*-plane (Phi = 90°). 90

Figure 5.23: Structure of the proposed circularly polarized wire-grid nano-antenna array: (a) top-view, and (b) side-view. 91

Figure 5.24: Normal component of the magnetic field (H_z) for the optimized circularly polarized nano wire-grid antenna array at 193.55 THz: (a) t = 0, and (b) $t = T/4$ (log scale). 92

Figure 5.25: Contour plot showing the axial ratio of the circularly polarized wire-grid nano-antenna array versus the lengths of the inner radiators L_{rin1} and L_{rin2}. 93

Figure 5.26: 3D radiation pattern of the optimum circularly polarized nano wire-grid antenna array at 193.55 THz. 94

Figure 5.27: 2D radiations pattern of the optimum circularly polarized nano wire-grid antenna array at 193.55 THz (a) Phi = 0˚, and (b) Phi = 90˚. 94

Figure 5.28: Axial Ratio versus frequency of the optimum circularly polarized nano wire-grid antenna array. 95

Figure 5.29: Variation of the directivity, gain and radiation efficiency of the optimum circularly polarized nano wire-grid antenna array versus frequency. 95

Figure 5.30: Structure of the wire-grid nano-antenna arrays: (a) five-elements, and (b) eleven-elements. 96

Figure 5.31: SEM photos for the fabricated wire-grid nano-antenna arrays: (a) five-elements, and (b) eleven-elements. 96

Figure 5.32: Measured (coloured) versus simulated extinction cross-section for the wire-grid arrays: (a) five-elements, and (b) eleven-elements. 97

Figure 5.33: Modal current distribution along the five-element wire-grid array at (a) 96 THz, (b) 274 THz, (c) 358 THz, and (d) 436 THz. 98

Figure 5.34: Modal current distribution along the eleven-element wire-grid array at: (a) 60 THz, (b) 180 THz, (c) 264 THz, and (d) 374 THz. 99

List of Tables

Table 3.1: Different cases and the corresponding values of the impedance matrix elements: Z'_{xx} or Z'_{zz} 56

Table 4.1: Number of unknowns required to calculate the propagation characteristics of the plasmonic transmission lines at 1.55 μm 66

Table 5.1: Sensitivity of the antenna array gain (at 193.55 THz) to 10% perturbation of its geometrical dimensions 88

Table 5.2: Optimum dimensions of the circularly polarized nano wire-grid antenna array 93

Table 5.3: Sensitivity of the axial ratio of the antenna array to 5% perturbation of the array geometrical dimensions 93

Table 5.4: Sensitivity of the gain of the antenna array to 5% perturbation of the array geometrical dimensions 93

Chapter 1: Introduction

With the ever increasing demand of high speed data communication, researchers are seeking the development of miniaturized devices operating at high frequencies. Recent technology has enabled the fabrication of small devices down to the nano-scale. Nevertheless, researchers faced some limitations in designing classical devices operating above the tens of GHz range as a result of power dissipation and RC delays [1]. On the other hand, photonic devices are capable of providing a wide bandwidth. However, their dimensions, being in the order of micrometres, are incompatible with the nano-sized electronic devices [1]. Plasmonic devices operating at optical frequencies offer a solution to this problem [2, 3]. They are characterized by their small dimensions (sub-wavelength), bridging the size gap between optical and electronic devices and enabling the development of components essential for high capacity photonic and electronic circuits [3].

The operation of plasmonic devices is based on Surface Plasmon Polariton (SPP) phenomenon which occurs when light interacts with free electrons of (noble) metals with negative permittivity at the interface with another dielectric medium with positive permittivity. This results in the excitation of an electromagnetic surface wave propagating at the metal/dielectric interface [4]. The excited wave is strongly confined to the interface and exponentially decays away from it with faster decay at the metal side [5]. Figure 1.1 shows an illustration for the SPP wave showing the decay of the field especially at the metal side. SPP phenomenon occurs in the optical frequency range where metal properties are different

from their counterparts in the millimetre (mm)-wave range. The main differences between classical and plasmonic metals will be highlighted in section 1.1.

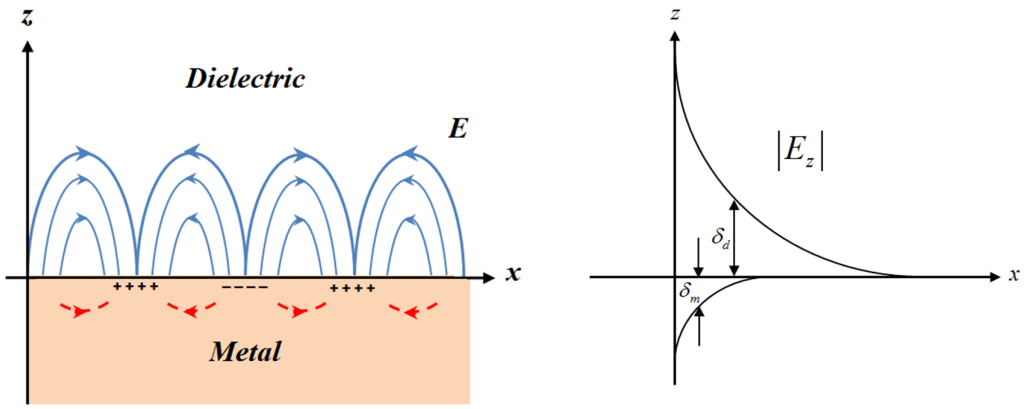

Figure 1.1: Surface Plasmon Polariton propagating along the interface between metal and dielectric media [6].

1.1 Classical versus Plasmonics Metals

1.1.1 Material Properties

Unlike dielectric materials, the properties of metals vary strongly according to the operating frequency. For frequencies below the visible range, metals are extremely reflective and they do not allow the penetration of electromagnetic waves inside them [7]. In the near-infrared and visible range, electromagnetic waves are capable of penetrating metal, which are, but not extremely, lossy. At the ultra-violet region, metals behave like dielectric materials where the electromagnetic waves penetrate the metals with attenuation losses determined based on the electronic band structures. It is worth noting that alkali metals have lots of free-electrons resulting in ultra-violet transparency behaviour. Nevertheless, for noble metals like gold (Au), silver (Ag), and Platinum (Pt), the transition between the electronic bands results in a strong absorption in the ultraviolet regime.

At optical frequencies, plasmonic structures have dimensions in the range of nano-meters. Regardless the small size of these structures, Maxwell's equations are still valid and no quantum effects are necessary for such cases [8]. This is due to the high density of electrons which makes the difference between the energy levels smaller than the thermal energy (k_BT) [9]. The optical behaviour of plasmonic metals can be described by Drude's Model as follows:

$$\hat{\varepsilon}_r(\omega) = \varepsilon' + j\varepsilon'' = \varepsilon_\infty - \frac{\omega_p^2}{\omega(\omega - j\omega_c)} \tag{1.1}$$

where ε_∞ is the epsilon at infinite frequency, ω_p is the plasma frequency, and ω_c is the collision frequency. This "*plasma model*" assumes that free electrons are moving freely against the positive ion cores. In the presence of an electric field $E(t) = E_0 e^{-j\omega t}$, electrons

start to oscillate and they face damping due to collisions with a rate denoted by γ. The equation of motion describing the plasma model is given by:

$$m\ddot{x} + m\gamma\dot{x} = -eE(t) \tag{1.2}$$

where "*m*" is the effective optical mass of each electron. This model can be used to describe alkali metals up to the ultra-violet range while for noble metals, the model is limited at the visible range due to the inter-band transitions which occurs at this range [9].

The solution of equation (1.2) provides a description for the electron oscillation which is given by:

$$x(t) = \frac{e}{m\left(\omega^2 + j\gamma\omega\right)} E(t) \tag{1.3}$$

Thus, the polarization "*P*" can be written as:

$$P = -nex = -\frac{ne^2}{m\left(\omega^2 + j\gamma\omega\right)} E \tag{1.4}$$

The electric displacement "*D*" is given by:

$$D = \varepsilon_0 \left(1 - \frac{\omega_p^2}{\omega^2 + j\gamma\omega}\right) E = \varepsilon_0 \hat{\varepsilon}_{r,eff}\left(\omega\right) E \tag{1.5}$$

where $\omega_p^2 = ne^2/\varepsilon_0 m$ represents the plasma frequency of the free electron gas. This means that the dielectric constant of metals is defined as:

$$\hat{\varepsilon}_{r,eff}\left(\omega\right) = 1 - \frac{\omega_p^2}{\omega^2 + j\gamma\omega} \tag{1.6}$$

Based on Drude's model, Figure 1.2 shows the relative dielectric permittivity, $\hat{\varepsilon}_{r,eff}\left(\omega\right)$, of gold and silver as function of the operating frequency. The figure shows that $\hat{\varepsilon}_{r,eff}\left(\omega\right)$ is dispersive. It consists of a negative real part, ε', representing the polarization strength, in addition to an imaginary part, ε'', representing (metallic) losses. It is worth noting that Drude's model is considered a good approximation for describing the dielectric permittivity of plasmonic materials at optical frequencies. It gives the correct prediction that at low optical frequency range, 180° out-of-phase polarization is achieved when an external field is applied [9]. This is interpreted by the negative sign of the real component of the dielectric constant which indicates high reflectivity.

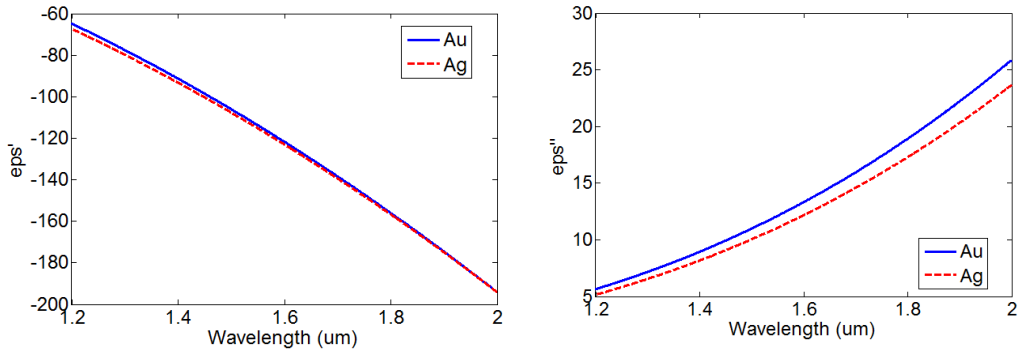

(a) (b)

Figure 1.2: The relative dielectric permittivity functions versus wavelength for plasmonic metals (Au, and Ag) at optical frequencies: (a) real part, and (b) imaginary part.

1.1.2 Surface versus Volumetric Current

When dealing with plasmonic devices, it should be taken into consideration that due to the fabrication limitations of the current available technology, the thickness of plasmonic metals is comparable to their lateral dimensions [10]. Hence, metals cannot be described as 2D sheets like the case of classical metals. Instead, plasmonic metals should be modelled as 3D structures. Additionally, for plasmonic structures, in most cases, their dimensions are comparable with their skin depth. From the modelling point of view, this means that volumetric currents are essentially required to describe currents along plasmonic structures while the approximation of surface currents would not be accurate.

The mentioned differences between classical and plasmonic metals require a more complex description for problems dealing with plasmonic topologies. Therefore, the software that has been developed to solve classical metals based devices should be upgraded to incorporate these differences. The next section will introduce the different numerical techniques that have been implemented in the literature and a comparison between them.

1.2 Numerical Techniques

In this thesis, the main scope is to obtain the mode profiles of plasmonic transmission lines (waveguides) placed in a planar multi-layered system. Additionally, the developed solver should calculate the corresponding propagation characteristics for each mode (i.e. the guided wavelength and the attenuation constant). The aforementioned problem can be solved using either differential or integral techniques. For differential techniques, the unknowns are the electric and magnetic fields along the entire domain surrounding and including the metallic strips, whereas the unknowns for the integral techniques are the electric and magnetic currents along the metallic strips.

Plasmonic waveguides have been previously studied in the literature using various numerical techniques including the Finite-Difference Frequency-Domain (FDFD) [10], Finite-Difference Time-Domain (FDTD) [12], Finite Element Method (FEM) [13], the

Method of Lines (MoL) [14], and the Effective Index Method (EIM) [13, 14]. In [11], the FDFD method is used to calculate the eigenmodes of various plasmonic transmission lines including the symmetric/asymmetric plasmonic slot, modified plasmonic slot, and plasmonic nano-strip waveguide which consists of a metallic strip and metallic substrate. Accurate calculation using the FDFD solver requires a computational domain big enough to ensure that the fields are negligible at the boundaries [11]. In [12], the FDTD method is applied to study the dispersion, dissipation and the fields of asymmetric coupled nano-wedges at various angles. The main disadvantage of the FDTD method is the high need for computational resources, including computer memory and calculation time [15]. This is especially true for plasmonic structures where metals are highly dispersive [16]. In [13], the EIM and the FEM are used and compared for calculating the propagating modes in dielectric-loaded SPP waveguides, whereas in [14], the EIM and the MoL are used to calculate the propagating modes of rectangular hollow waveguides. In both papers, it has been demonstrated that the EIM is simple, but in some cases this method fails to give accurate results. For example, in [13], the accuracy of the EIM is limited to waveguides whose propagating modes are far from the cut-off frequency. The FDFD, FDTD, and FEM have the advantage of directly implementing the differential Maxwell equations [17]. However, the main drawback of these techniques is that the discretization is necessary not only for the plasmonic structures themselves, but also for the space surrounding them [18]. This results in a much bigger number of unknowns leading to huge memory requirements and calculation times. Moreover, the truncation boundary conditions needed for such solvers introduce some sort of errors if the transmission lines under investigation are open, which is usually the case.

The Method of Moments (MoM) offers a solution to this problem since it involves the discretization of the metallic object solely [18], resulting in a tremendous decrease in the number of unknowns. Furthermore, this technique is characterized by its high accuracy and stability [19] due to the fact that an integral formulation is adopted, and consequently most of the output parameters are expressed in an integral form. Besides, the MoM does not require inserting absorbing Perfectly Matched Layers (PML) across the boundaries, since the MoM assumes that the flat layered media are infinitely extended. This reduces the sources of errors compared to the differential-based techniques. The MoM is used in [20], where the surface impedance model is presented to solve plasmonic circuits. This technique is suitable for Long Range Surface Plasmon Polariton (LRSPP) waveguides, which are constructed from nm-thick and μm-wide metal strips embedded in a dielectric medium, because only circumference currents are considered. In [21], the MoM has been applied to calculate the propagation characteristics of a nano-strip graphene transmission line. The nano-strip line is constructed from an infinitesimally thin strip of graphene which has a finite width and is mounted on a grounded substrate. Therefore, in this model only one component of the two transverse currents is considered.

In this work, the aim is to develop a solver that can calculate the propagation characteristics of plasmonic transmission lines of "*any*" topology and located within a stacked planar layered structure. This means that the thickness of these transmission lines generally should

be considered. In such case, for this solver, it is essential to take into account the volumetric current that can flow along the plasmonic transmission lines.

It is worth noting that in this work, we are also concerned with the development of nano-antennas as they have significant applications. The developed solver cannot be used to obtain the radiation characteristics of the nano-antennas directly; however, it can be used to predict the propagation characteristics of special types of antennas like dipole antennas or wire-grid arrays. The mode solver can calculate the propagation constant and attenuation losses of plasmonic waveguides having the same topology as wire antenna. This in turns enables the prediction of the guided wavelength of the dipole antennas as well as their radiation efficiencies. In other words, the developed solver is very useful in identifying the initial dimensions of wire-based nano-antennas. The accurate dimensions can then be optimized using commercial tools like CST Microwave Studio.

In the next section, the various applications of plasmonic transmission lines and nano-antennas will be highlighted.

1.3 Plasmonic Transmission Lines

Waveguides are considered essential components in optoelectronic and photonic devices [21]. The wave guiding in these devices differ from those used at microwave or Radio Frequency (RF) range. In the later, dielectric materials enclosed with metals are usually used as wave guiding structures. The lateral dimensions of these waveguide determine the operating frequencies if they are closed with metal [22]. Waves can also be guided using transmission lines whose dimensions are not restricted with the wavelength of the electromagnetic wave they carry. However, at optical frequencies, metals became poor conductor with high losses. Consequently, they are not used typically for wave transmission. Instead, dielectric waveguides like optical fibres are used since they are characterized by their very low absorption and low losses (in order of 1 dB/km). The wave is guided when there is a big difference between a high dielectric constant medium and that of free-space or a lower dielectric constant cladding area. Nevertheless, the dimensions of optical waveguides should be equal to or greater than the wavelength of light. Consequently, the bulky nature of optical waveguides means that photonic components like interferometers, couplers, etc. will require a relatively large footprint in photonic circuits. With the high demand of miniaturization of the optical devices, SPP phenomenon opened the gate for fabricating devices characterized with their relatively small dimensions compared to photonic waveguides. SPP waveguides are hybrid waveguides consisting of both metallic and dielectric materials. With their ability of wave confinement in sub-wavelength region at the metallic/dielectric interface, they are capable of squeezing light beyond its diffraction limit. Due to the wave localization at the metallic/dielectric interface, any change in the surrounding medium has a strong impact on the waveguide properties. This phenomenon can be invested and applied for sensing applications.

Different SPP waveguide topologies have been presented in the literature [13, 23-26]. Among these structures are metallic nano-strip [23], nano-trench and V-groove

waveguides [24], metal-insulator-metal waveguides [25, 26], dielectric-loaded SPP waveguides [13], and LRSPP [27]. Judging the performance of plasmonic waveguides is dependent on two factors: the mode confinement and the propagation distance of the excited mode [28, 29]. The mode confinement is roughly defined by the ratio of the field penetrating the metal to that penetrating the dielectric [28]. Higher field penetration inside the metal implies better mode confinement. However, it also implies that the wave suffers from more attenuation due to losses encountered inside metals at optical frequencies. Waveguide structures like nano-strip, nano-trenches, and V-grooves are suitable for non-linear optical and bio-sensing applications where mode confinement and power localization are crucial [28]. On the other hand, LRSPP is a very good candidate for applications like optical sensors, attenuators, couplers, filters, and modulators [30-34] as it supports waves of long propagation length. Hybrid waveguides offer a compromise between mode confinement and long propagation length [35].

1.4 Plasmonic Nantennas

Plasmonic antennas (optical antennas/nano-antennas/nantennas) are nano-sized devices which are capable of converting electromagnetic waves into localized electric current/voltage and vice versa, similar to antennas in the microwave frequencies [36]. Compared to RF antennas whose dimensions are in the order of half free-space/guided wavelength, nano-antennas are characterized by their smaller size owing to the fact that the guided wavelength in nano-antennas is much smaller than the free-space wavelength. On the other hand, nantennas are suffering from higher metallic losses. Moreover, due to the SPP phenomenon, only one metal object is sufficient to realize a nantenna. Nano-antennas have several applications. They are capable of converting the solar radiation into electricity and thus can be used for energy harvesting [37]. They can also be used in the enhancement and direction of emissions from single molecules suitable for sensing and spectroscopy applications [38, 39]. Furthermore, they can be used as scatterers to direct the incident light [40]. Plasmonic antennas can also couple electromagnetic waves in the visible and/or infra-red spectrum and confine them into localized energy. In this case, they can replace lenses [41]. Furthermore, nantennas can be used as efficient sensors [42]. In optical communication systems, nantennas are used to convert electromagnetic waves into electric current and vice versa. Due to their small size, their radiation can only extend over a short distance. Therefore, they can be used for inter- /intra-chip applications where data can be transferred between optical circuits and/or chips located at different layers. The design and analysis of optical nano-antennas is different from millimetre and radio frequency antennas due to the dispersive and lossy nature of plasmonic metals constructing them, as discussed earlier. The new features added challenges to design nantennas characterized by high-efficiency. Nano-antennas can be constructed from diverse materials and they can have various topologies. In most cases, nano-antennas are constructed from noble metals (like Gold/Au, Silver/Ag, etc.); however, dielectric materials can also be used. In the literature, several nano-antenna topologies have been introduced including nano-spheres [43], nano-dipoles [44], bow-tie nano-antennas [45], dielectric resonator nantennas [46], crescent [47], and cross-antennas [48]. Some examples of these antennas are shown in Figure 1.3.

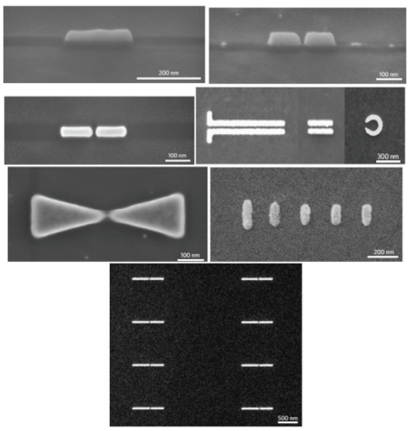

Figure 1.3: Examples of different fabricated nano-antenna topologies including dipole, and bow-tie antennas [49].

In most cases, nano-antennas are used in an array form to increase their directivity if they are used for data transmission or to increase the field localization if they are used for sensing, and field enhancement applications. In the literature, several arrays have been proposed; however, the array elements are usually not connected to each other. For optical communication applications, the nano-antenna elements should be connected together to increase the directivity of the antenna and consequently the communication range. Thus, in this thesis the scope is to develop nano-antenna array whose elements are connected to each other. Since plasmonic materials constructing the nantenna are lossy, increasing the array elements has an adverse effect on the radiation efficiency of the antenna regardless the increase of its directivity.

Among the proposed antennas in this work is a novel design for a circularly polarized wire-grid array. In optical applications, circular polarization, i.e. rotating electromagnetic fields, can be used in lots of applications. Examples of these applications include all-magnetic recording [50, 51]. In this case, a circularly polarized electric field is used to replace the magnetic field. The variation of the magnetic field direction is thus replaced by changing the polarization of the electric field from Left Hand Circular Polarization (LHCP) to Right Hand Circular Polarization. Other applications include micro-gear rotation [52], optical magnetic resonances in semi-conductors [53], optical chirality engineering [54], and characterization of optically active single-walled carbon nano-tubes [55]. Moreover, circularly polarized nantennas are suitable for imaging application as the incident and reflected waves can be easily separated without a rotator. This is because an incident LHCP wave is essentially a RHCP reflected wave, and vice versa. Such important applications lead to a growing need for the design of devices capable of producing circularly polarized light. Circular polarization can be obtained by the superposition of two cross propagating evanescent waves as presented in [56]. Another method for obtaining circularly polarized light is by making a circular hole surrounded by elliptical gratings [57] and L-shaped arrays [58]. Nano-antennas can also be used to obtain circularly polarized optical spots. Although most of the nano-antennas presented in the literature provide linear polarization [59-61], the significant application of circular polarization motivated researchers to design nano-

antennas like cross-dipole nano-rods [62], slant-gap [63] and common-gap plasmonic nano-antennas [64] that can provide circular polarization.

1.5 Scope of the Thesis

The scope of the thesis can be split into two correlated lines. In the first line, the aim is to develop a plasmonic transmission line mode solver that obtains the modal current profile for each propagating mode in the transmission line and identifies its propagation and attenuation constants. The solver should not have any constraints regarding the plasmonic transmission line topology nor the layered medium surrounding it. The second line of this research is related to the design of novel plasmonic antenna topologies using different materials. Achieving high efficiency for nano-antennas is considered a real challenge due to the high losses of metals at the optical frequency range. These miniaturized nantennas are the interface between the radiated waves in free-space and the guided waves propagating along waveguides. The developed plasmonic solver is first used to estimate the initial dimensions of the wire-based antenna and its radiation efficiency. Afterwards, the optimization of the basic structures is performed using commercial tools, which are also used to calculate the antenna's radiation characteristics.

The thesis is arranged as follows: In chapter two, the detailed analysis for the problem under investigation starting from Maxwell's equation is presented. This chapter also includes the derivation of the spectral and spatial domain Green's functions. In chapter three, the MoM technique is discussed in details, where the method of obtaining the propagation characteristics of plasmonic transmission lines and the modal current distribution are presented. In chapter four, the plasmonic mode solver is examined for various transmission lines that have different topology, and/or number of metallic strips. Different layered media also are used to ensure that the developed solver is generic. In chapter five, three wire-grid nano-antenna arrays are presented. A wire-grid array consisting of five elements is first studied when the antenna is placed in homogeneous medium. The antenna has a linear polarization. Unlike the almost isotropic radiation pattern of a single nano-antenna element, the array of nantennas offers pencil narrow beam. Such beam is required for point-to-point optical communication systems. Finally, in this chapter, two versions for a wire-grid antenna array placed within a layered medium are presented. One is considered an extended version of the five-element wire-grid array. It consists of eleven elements instead of five. The other antenna is designed for circular polarization where two nano-antenna arrays are placed orthogonal to each other and their excitation has 90˚ phase difference to achieve the required circularly polarized radiation. In both designs, the nantennas provide a highly directive beam which is also suitable for point-to-point communication. This chapter ends by showing a prototype of a similar wire-grid arrays which are fabricated and measured. A comparison between simulations and experimental results is presented in this chapter. Finally, in chapter six, a summary of the work is concluded and the future extension of the work is outlined.

Chapter 2: Spectral and Spatial Domain Green's Functions

The Green's functions are considered of great importance in electromagnetics where they represent the response of the system due to the presence of a hypothetical unit source. When solving an electromagnetic problem encountering a linear system, one can decompose the source into a number of infinitesimal unitary sources. The response of the system due to each source is first calculated. To obtain the response due to the total source, superposition is applied. In this work, we consider a source which is extended to infinity. So the unitary source can be represented by a filament dipole. Obtaining the Green's functions starts by solving Maxwell's equations and applying the boundary conditions at the interface of each layer/source. These equations are solved in spectral domain as there is a closed form for the spectral domain Green's functions. On the other hand, there is no closed form for the spatial domain Green's functions except in homogeneous medium. The solution of Maxwell's equations and the boundary conditions results in a relation between the spectral domain electric fields and the spectral domain electric current densities that are linked through the Green's functions. In [65], the spectral domain Green's functions are obtained assuming both electric and magnetic current sources. In this work, only electric current sources are considered. The Green's functions can be calculated depending on the type of the layered medium surrounding the source. In this work, four different layer structures are considered: when the electric current source is located in (a) homogeneous medium, (b) at the interface of two half-spaces, (c), at the top layer of a three-layered medium, and (d) at the middle

layer of a three-layered medium. In each case, the expressions of the spectral domain Green's functions are presented. In the spatial domain, the Green's functions can be obtained using the Sommerfeld identity. However, the integral is slowly decaying and requires a long computational time. As a result, the discrete complex image method is adopted in this chapter, which enables to obtain closed form expressions for the spatial domain Green's functions.

2.1 Problem under Investigation

Figure 2.1 shows the topology of the general plasmonic transmission line under investigation. It consists of a number of metal strips embedded within a stack of flat layers. Each strip has an arbitrary cross-sectional shape with finite dimensions along the *xz*-plane, while it extends infinitely along the *y*-axis. Each flat background layer extends infinitely along the *xy*-plane, with a finite thickness along the *z*-axis. The background layers can be either dielectric or metallic. The upper and lower layers are assumed to be infinitely extended in the positive and negative *z*-axis respectively so they are treated as open half spaces.

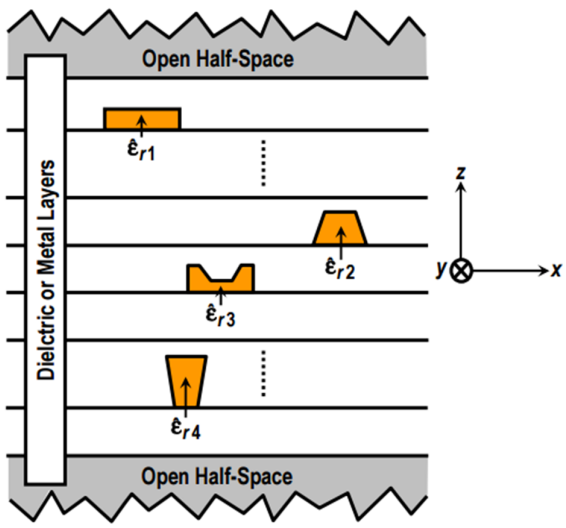

Figure 2.1: Generalized plasmonic transmission line made up of a number of metallic strips with arbitrary cross-section and dimensions, immersed within a stack of flat dielectric or metallic layers.

Figure 2.2 shows the layer structure of the unit source located at the interface of the two layers j and j+1. When both interface layers are identical, this means that the source is located in a certain layer. The dielectric permittivity and permeability of this source are denoted by ε_j, and μ_i respectively, which is generally complex and dispersive. As a general case, the ith layer also has a complex and dispersive dielectric permittivity which is defined as:

$$\varepsilon_i = \varepsilon'(f) - j\varepsilon''(f) \tag{2.1}$$

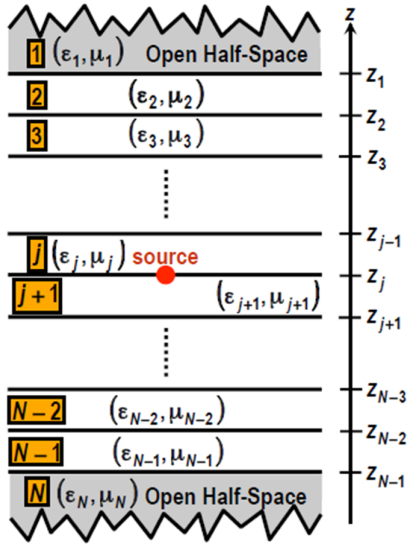

Figure 2.2: Unit current source located at the interface of the layers j, and j+1.

Generally, the source can be a Horizontal Electric Dipole (HED), a Horizontal Magnetic Dipole (HMD), a Vertical Electrical Dipole (VED), a Vertical Magnetic Dipole (VMD), or a combination of them [65]. In this work, no magnetic current sources are considered; only electric current sources are taken into consideration. Consequently, the jth interface between the layers j, and j+1 can be carrying a HED, VED or both of them.

As mentioned in chapter 1, for electromagnetic problems constructed from plasmonic metals, Maxwell's equations are valid. In the MoM, it is essential to work in spectral domain rather than spatial domain when dealing with layered media. The reason is that there is no closed form for the spatial domain Green's functions. On the other hand, the spectral domain Green's functions can be obtained analytically [66]. Assuming the time dependence for the propagating wave in the form of $e^{j\omega t}$, Maxwell's equations at a source-free interface can be expressed in frequency domain as follows:

$$\underline{\nabla} \times \underline{E}_i = -j\omega\mu_i \underline{H}_i \tag{2.2}$$

$$\underline{\nabla} \times \underline{H}_i = j\omega\varepsilon_i \underline{E}_i \tag{2.3}$$

$$\underline{\nabla} \cdot \underline{D}_i = 0 \tag{2.4}$$

$$\underline{\nabla} \cdot \underline{B}_i = 0 \tag{2.5}$$

where $\underline{E}_i$, $\underline{H}_i$, $\underline{D}_i$, and $\underline{B}_i$ are the spatial domain electric field, magnetic field, electric flux density, and magnetic flux density respectively at a certain i^{th} layer.

Solving equations (2.2) and (2.3) leads to the following Helmholtz equations:

$$\underline{\nabla}^2 \underline{E}_i + \omega^2 \mu_i \varepsilon_i \underline{E}_i = 0 \tag{2.6}$$

$$\underline{\nabla}^2 \underline{H}_i + \omega^2 \mu_i \varepsilon_i \underline{H}_i = 0 \tag{2.7}$$

In spectral domain, the Helmholtz equations (2.6) and (2.7) are expressed as:

$$\frac{d^2}{dz^2}\underline{\tilde{E}}_i + \left(-k_x^2 - k_y^2 + \omega^2 \mu_i \varepsilon_i\right)\underline{\tilde{E}}_i = \frac{d^2}{dz^2}\underline{\tilde{E}}_i + k_{zi}^2 \underline{\tilde{E}}_i = 0 \tag{2.8}$$

$$\frac{d^2}{dz^2}\underline{\tilde{H}}_i + \left(-k_x^2 - k_y^2 + \omega^2 \mu_i \varepsilon_i\right)\underline{\tilde{H}}_i = \frac{d^2}{dz^2}\underline{\tilde{H}}_i + k_{zi}^2 \underline{\tilde{H}}_i = 0 \tag{2.9}$$

where k_x and k_y are the spectral counterparts of the spatial variables *x*, and *y*. In spectral domain, the differentiation $\partial/\partial x$, and $\partial/\partial y$ are replaced by $-jk_x$, and $-jk_y$ respectively. The symbol (~) which appears on top of a certain quantity indicates that it is expressed in spectral domain.

The solution of equations (2.8) and (2.9) can be easily found leading to the following equations:

$$\underline{\tilde{E}}_i\left(k_x, k_y, z\right) = \underline{E}_i^+\left(k_x, k_y\right)e^{-jk_{zi}z} + \underline{E}_i^-\left(k_x, k_y\right)e^{jk_{zi}z} \tag{2.10}$$

$$\underline{\tilde{H}}_i\left(k_x, k_y, z\right) = \underline{H}_i^+\left(k_x, k_y\right)e^{-jk_{zi}z} + \underline{H}_i^-\left(k_x, k_y\right)e^{jk_{zi}z} \tag{2.11}$$

Those equations show that each component of the electric and magnetic fields consist of two terms. The first term is propagating along the positive *z*-direction, while the other one is propagating along the negative *z*- direction. So, for each layer, there are twelve unknowns: E_{xi}^+, E_{xi}^-, E_{yi}^+, E_{yi}^-, E_{zi}^+, E_{zi}^-, H_{xi}^+, H_{xi}^-, H_{yi}^+, H_{yi}^-, H_{zi}^+, and H_{zi}^-. For the first layer (layer 1), which includes $z = +\infty$, the term $e^{jk_{z1}z}$ is omitted as no reflection is expected from ∞. Similarly, for the bottom layer (layer *N*), which includes $z = -\infty$, the term $e^{-jk_{zN}z}$ is omitted, as there is no reflection expected from the $-\infty$. Consequently, for a layer structure with *N* layers, there are $12(N-1)$ unknowns. The outer layers each contain six unknowns while the inner layers have a total of $12(N-2)$ unknowns.

Now, back to Maxwell's equations (2.2) – (2.5), in spectral domain, they can be expressed as follows:

$$\left(-jk_x \underline{u}_x - jk_y \underline{u}_y + \frac{d}{dz}\underline{u}_z\right) \times \underline{\tilde{E}}_i = -j\omega\mu_i \underline{\tilde{H}}_i \tag{2.12}$$

$$\left(-jk_x\underline{u}_x - jk_y\underline{u}_y + \frac{d}{dz}\underline{u}_z\right)\times\underline{\tilde{H}}_i = j\omega\varepsilon_i\underline{\tilde{E}}_i \tag{2.13}$$

$$\left(-jk_x\underline{u}_x - jk_y\underline{u}_y + \frac{d}{dz}\underline{u}_z\right)\cdot\underline{\tilde{E}}_i = 0 \tag{2.14}$$

$$\left(-jk_x\underline{u}_x - jk_y\underline{u}_y + \frac{d}{dz}\underline{u}_z\right)\cdot\underline{\tilde{H}}_i = 0 \tag{2.15}$$

Equations (2.12) – (2.15) result in eight scalar equations for each layer. Since each electric and magnetic field component is constructed from two terms, the eight scalar equations contain twelve unknowns. Consequently, the twelve unknowns can be expressed in terms of four independent variables of our choice. For simplicity, the chosen independent unknowns are: $\tilde{E}_z^+$, $\tilde{E}_z^-$, $\tilde{H}_z^+$, and $\tilde{H}_z^-$. The reason for choosing these independent unknowns specifically is that they facilitate the decomposition of the system into TE-z and TM-z systems as will be shown afterwards. Solving these equations together, and after some mathematical manipulations, the spectral domain electric and magnetic fields can be defined as follows:

$$E_{xi}^{\pm} = \left(\mp k_x k_{zi} E_{zi}^{\pm} - \omega\mu_i k_y H_{zi}^{\pm}\right)\Big/ k_\rho^2 \tag{2.16}$$

$$E_{yi}^{\pm} = \left(\mp k_y k_{zi} E_{zi}^{\pm} + \omega\mu_i k_x H_{zi}^{\pm}\right)\Big/ k_\rho^2 \tag{2.17}$$

$$H_{xi}^{\pm} = \left(\omega\varepsilon_i k_y E_{zi}^{\pm} \mp k_x k_{zi} H_{zi}^{\pm}\right)\Big/ k_\rho^2 \tag{2.18}$$

$$H_{yi}^{\pm} = \left(-\omega\varepsilon_i k_x E_{zi}^{\pm} \mp k_y k_{zi} H_{zi}^{\pm}\right)\Big/ k_\rho^2 \tag{2.19}$$

where $k_\rho^2 = k_x^2 + k_y^2$. It is worth noting that for the top-most and bottom-most layers, the coefficients $\left(E_{zi}^-, H_{zi}^-\right)$ and $\left(E_{zi}^+, H_{zi}^+\right)$, respectively, vanish.

2.2 TE and TM Field Decomposition

2.2.1 TE System

For the Transverse Electric (TE) system, the normal component of the electric field is set to zero. Thus, E_{zi}^+, and E_{zi}^- appearing in equations (2.16) – (2.19) vanish. Accordingly, the field components can be expressed in terms of the normal components of the magnetic field: i.e. $\tilde{H}_z^+$, and $\tilde{H}_z^-$ only. The electromagnetic equations for the TE system can thus be expressed as follows:

$$\tilde{E}_{zi}^{TE} = 0, \quad \tilde{H}_{zi}^{TE} = A_i S_i^{TE+}(z) \tag{2.20}$$

$$\tilde{E}_{xi}^{TE} = -\frac{\omega\mu_i k_y}{k_\rho^2} A_i S_i^{TE+}(z) \tag{2.21}$$

$$\tilde{E}_{yi}^{TE} = \frac{\omega\mu_i k_x}{k_\rho^2} A_i S_i^{TE+}(z) \tag{2.22}$$

$$\tilde{H}_{xi}^{TE} = -\frac{k_x k_{zi}}{k_\rho^2} A_i S_i^{TE-}(z) \tag{2.23}$$

$$\tilde{H}_{yi}^{TE} = -\frac{k_y k_{zi}}{k_\rho^2} A_i S_i^{TE-}(z) \tag{2.24}$$

where,

$$A_i = \begin{cases} H_{zi}^{+,TE}, & i \le j \\ H_{zi}^{-,TE}, & i > j \end{cases} \tag{2.25}$$

$$\Gamma_i^{TE} = \begin{cases} H_{zi}^{-,TE} / H_{zi}^{+,TE}, & i \le j \\ H_{zi}^{+,TE} / H_{zi}^{-,TE}, & i > j \end{cases} \tag{2.26}$$

$$S_i^{TE\pm}(z) = \begin{cases} e^{-jk_{zi}z} \pm \Gamma_i^{TE} e^{jk_{zi}z}, & i \le j \\ \Gamma_i^{TE} e^{-jk_{zi}z} \pm e^{jk_{zi}z}, & i > j \end{cases} \tag{2.27}$$

where i represent the layer at which the fields are calculated while j represents the interface carrying the current source. Γ_i^{TE} represents the reflection coefficient of the ith layer. As shown from equations (2.20) – (2.27), all the electromagnetic field components are represented in terms of two unknowns only: A_i, and Γ_i^{TE}. The total unknowns of the problem under investigation are thus reduced into $2(N-1)$ variables instead of $4(N-1)$.

2.2.2 TM System

In a similar way, the electromagnetic fields for the Transverse Magnetic (TM) system are obtained by setting the normal component of the magnetic field to zero i.e. $\tilde{H}_z^+ = \tilde{H}_z^- = 0$. Accordingly, the electromagnetic fields can be expressed as follows:

$$\tilde{H}_{zi}^{TM} = 0, \quad \tilde{E}_{zi}^{TM} = B_i S_i^{TM+}(z) \tag{2.28}$$

$$\tilde{E}_{xi}^{TM} = -\frac{k_x k_{zi}}{k_\rho^2} B_i S_i^{TM-}(z) \tag{2.29}$$

$$\tilde{E}_{yi}^{TM} = -\frac{k_y k_{zi}}{k_\rho^2} B_i S_i^{TM-}(z) \tag{2.30}$$

$$\tilde{H}_{xi}^{TM} = \frac{\omega \varepsilon_i k_y}{k_\rho^2} B_i S_i^{TM+}(z) \tag{2.31}$$

$$\tilde{H}_{yi}^{TM} = -\frac{\omega \varepsilon_i k_x}{k_\rho^2} B_i S_i^{TM+}(z) \tag{2.32}$$

where,

$$B_i = \begin{cases} E_{zi}^{+,TM}, & i \le j \\ E_{zi}^{-,TM}, & i > j \end{cases} \tag{2.33}$$

$$\Gamma_i^{TM} = \begin{cases} E_{zi}^{-,TM} / E_{zi}^{+,TM}, & i \le j \\ E_{zi}^{+,TM} / E_{zi}^{-,TM}, & i > j \end{cases} \tag{2.34}$$

$$S_i^{TM\pm}(z) = \begin{cases} e^{-jk_{zi}z} \pm \Gamma_i^{TM} e^{jk_{zi}z}, & i \le j \\ \Gamma_i^{TM} e^{-jk_{zi}z} \pm e^{jk_{zi}z}, & i > j \end{cases} \tag{2.35}$$

Similarly, all the field components of the TM system can be expressed in the ith layer in terms of two variables: B_i , and Γ_i^{TM} .

2.3 TE and TM Current Decomposition

At the jth interface where a source is located, the tangential electric fields are discontinuous. Assuming the presence of electric current sources only, the tangential electric and magnetic fields are given by [67]:

$$\underline{u}_z \times \left(\underline{E}_{j+1} - \underline{E}_j \right) = \frac{-1}{j\omega\varepsilon_j} \underline{\nabla}_{xy} \times \underline{J}_{zj} \tag{2.36}$$

$$\underline{u}_z \times \left(\underline{H}_{j+1} - \underline{H}_j \right) = -\underline{J}_{(xy)j} \tag{2.37}$$

In spectral domain, equations (2.36), and (2.37) lead to the following equations:

$$\tilde{E}_{x(j+1)} - \tilde{E}_{x(j)} = \frac{-k_x}{\omega\varepsilon_j} \tilde{J}_{zj} \tag{2.38}$$

$$\tilde{E}_{y(j+1)} - \tilde{E}_{y(j)} = \frac{-k_y}{\omega\varepsilon_j} \tilde{J}_{zj} \tag{2.39}$$

$$\tilde{H}_{x(j+1)} - \tilde{H}_{x(j)} = -\tilde{J}_{yj} \tag{2.40}$$

$$\tilde{H}_{y(j+1)} - \tilde{H}_{y(j)} = \tilde{J}_{xj} \tag{2.41}$$

where $\tilde{J}_{xj}$, $\tilde{J}_{yj}$, and $\tilde{J}_{zj}$ are the *x*-, *y*-, and *z*- directed electric current sources which are placed at the jth interface.

2.3.1 Conditions on TE Currents

For the TE system, the discontinuity of the tangential electric and magnetic fields due to the presence of electric current sources can be obtained by substituting equations (2.21) – (2.24) into the boundary conditions equations (2.38) – (2.41) which leads to the following equations:

$$\frac{\omega\mu_{j+1}k_x}{k_\rho^2} A_{j+1} S_{j+1}^{TE+}\left(z_j\right) - \frac{\omega\mu_j k_x}{k_\rho^2} A_j S_j^{TE+}\left(z_j\right) = -\frac{k_y}{\omega\varepsilon_j}\tilde{J}_{zj}^{TE} \tag{2.42}$$

$$-\frac{\omega\mu_{j+1}k_y}{k_\rho^2} A_{j+1} S_{j+1}^{TE+}\left(z_j\right) + \frac{\omega\mu_j k_y}{k_\rho^2} A_j S_j^{TE+}\left(z_j\right) = -\frac{k_x}{\omega\varepsilon_j}\tilde{J}_{zj}^{TE} \tag{2.43}$$

$$-\frac{k_y k_{z(j+1)}}{k_\rho^2} A_{j+1} S_{j+1}^{TE-}\left(z_j\right) + \frac{k_y k_{zj}}{k_\rho^2} A_j S_j^{TE-}\left(z_j\right) = \tilde{J}_{xj}^{TE} \tag{2.44}$$

$$-\frac{k_x k_{z(j+1)}}{k_\rho^2} A_{j+1} S_{j+1}^{TE-}\left(z_j\right) + \frac{k_x k_{zj}}{k_\rho^2} A_j S_j^{TE-}\left(z_j\right) = -\tilde{J}_{yj}^{TE} \tag{2.45}$$

Dividing equation (2.42) by k_x and equation (2.43) by k_y yields to:

$$\tilde{J}_{zj}^{TE} = 0 \tag{2.46}$$

Similarly, dividing equation (2.44) by k_y and equation (2.45) by k_x yields to:

$$\frac{\tilde{J}_{xj}^{TE}}{k_y} = -\frac{\tilde{J}_{yj}^{TE}}{k_x} \tag{2.47}$$

The above equations demonstrate that the four boundary conditions of each layer are reduced into two independent equations. Thus, for the TE system there are $2\left(N-1\right)$ independent equations which are similar to the number of unknowns for this system.

2.3.2 Conditions on TM Currents

Using the same methodology, the discontinuity of the tangential fields due to the presence of electric current sources can be obtained by substituting the tangential fields expressions presented in equations (2.31), and (2.32) into the boundary conditions equations (2.40) and (2.41). This leads to the following equations:

$$-\frac{\omega\varepsilon_{j+1}k_x}{k_\rho^2}B_{j+1}S_{j+1}^{TM+}\left(z_j\right)+\frac{\omega\varepsilon_j k_x}{k_\rho^2}B_j S_j^{TM+}\left(z_j\right)=\tilde{J}_{xj}^{TM} \tag{2.48}$$

$$\frac{\omega\varepsilon_{j+1}k_y}{k_\rho^2}B_{j+1}S_{j+1}^{TM+}\left(z_j\right)-\frac{\omega\varepsilon_j k_y}{k_\rho^2}B_j S_j^{TM+}\left(z_j\right)=-\tilde{J}_{yj}^{TM} \tag{2.49}$$

Dividing equation (2.48) by k_x and equation (2.49) by k_y yields to the following equation:

$$\frac{\tilde{J}_{xj}^{TM}}{k_x}=\frac{\tilde{J}_{yj}^{TM}}{k_y} \tag{2.50}$$

2.3.3 Combined Current Expressions for the TE and TM Systems

With the knowledge of the current components expressions in the previous section, the original current components can be obtained by performing a superposition for the TE and TM systems. Therefore, each current component can be expressed as follows:

$$\tilde{J}_{(x,y,z)j}=\tilde{J}_{(x,y,z)j}^{TE}+\tilde{J}_{(x,y,z)j}^{TM} \tag{2.51}$$

By substituting equations (2.46) and (2.47) into equation (2.51), and after some mathematical manipulations, the electric current components of the TE and TM systems can be expressed as follows:

$$\tilde{J}_{xj}^{TE}=\frac{k_y}{k_\rho^2}\left(k_y\tilde{J}_{xj}-k_x\tilde{J}_{yj}\right) \tag{2.52}$$

$$\tilde{J}_{zj}^{TE}=0 \tag{2.53}$$

$$\tilde{J}_{xj}^{TM}=\frac{k_x}{k_\rho^2}\left(k_x\tilde{J}_{xj}+k_y\tilde{J}_{yj}\right) \tag{2.54}$$

$$\tilde{J}_{zj}^{TM}=\tilde{J}_{zj} \tag{2.55}$$

It is worth noting that the *y*-components of the electric currents are not mentioned as they are expressed in terms of the *x*- component of the currents as defined in equations (2.47), and (2.50).

2.4 Solutions of the TE and TM systems

The spectral domain electric fields at the ith layer resulting from the presence of a current source at the jth interface can be obtained using a recursive algorithm [68–69] which is employed for both the TE and TM systems. This will be shown in the following sections.

2.4.1 Solution of the TE System

At a source-free interface, the tangential field components are continuous. Thus, after re-writing equations (2.42), and (2.44) by setting the currents to zero, one obtains the following equations:

$$\frac{\omega\mu_{i+1}k_x}{k_\rho^2}A_{i+1}S_{i+1}^{TE+}\left(z_i\right)-\frac{\omega\mu_i k_x}{k_\rho^2}A_i S_i^{TE+}\left(z_i\right)=0 \tag{2.56}$$

$$-\frac{k_y k_{z(j+1)}}{k_\rho^2}A_{i+1}S_{i+1}^{TE-}\left(z_i\right)+\frac{k_y k_{zi}}{k_\rho^2}A_i S_i^{TE-}\left(z_j\right)=0 \tag{2.57}$$

After some mathematical manipulations, and solving for $i \le j$, the reflection coefficient at the i+1 layer can be expressed in terms of that at the ith layer as follows:

$$\Gamma_{i+1}^{TE}=\frac{R_{i,i+1}^{TE}+\Gamma_i^{TE}e^{j2k_{zi}z_i}}{1+R_{i,i+1}^{TE}\Gamma_i^{TE}e^{j2k_{zi}z_i}}e^{-j2k_{z(i+1)}z_i} \tag{2.58}$$

$$R_{i,i+1}^{TE}=\frac{\mu_i k_{z(i+1)}-\mu_{i+1}k_{zi}}{\mu_i k_{z(i+1)}+\mu_{i+1}k_{zi}} \tag{2.59}$$

Equation (2.58) demonstrates that the reflection coefficient at a certain layer can be determined in a recursive way in terms of the reflection coefficient of the layer above, if both layers are above the source interface. As the first layer has a known reflection coefficient $\Gamma_1^{TE}=0$, the reflection coefficients of the following layers can be calculated accordingly until the interface layer of the source, where the boundary conditions are different.

Again using equations (2.56), and (2.57), while solving for $i > j$, we obtain:

$$\Gamma_i^{TE}\left(z_i\right)=\frac{R_{i+1,i}^{TE}+\Gamma_{i+1}^{TE}e^{-j2k_{z(i+1)}z_i}}{1+R_{i+1,i}^{TE}\Gamma_{i+1}^{TE}e^{-j2k_{z(i+1)}z_i}}e^{j2k_{zi}z_i} \tag{2.60}$$

In a similar way, the reflection coefficient at the bottom layer vanishes where $\Gamma_N^{TE}=0$. Thus, the layers above the Nth layer can be obtained in an inward recurrence technique using

equation (2.60) until the interface of the current source. As a result, the reflection coefficients of all the above layers can be obtained until the interface of the current source.

Back to the boundary conditions along the source interface, by solving equations (2.42), (2.44) and (2.53), and after some mathematical calculations, the coefficients A_j, and A_{j+1} can be obtained as follows:

$$A_j = k_\rho^2 \frac{a_j^{HED}}{k_y} \tilde{J}_{xj}^{TE} \tag{2.61}$$

$$A_{j+1} = k_\rho^2 \frac{a_{j+1}^{HED}}{k_y} \tilde{J}_{xj}^{TE} \tag{2.62}$$

where,

$$a_j^{HED} = -\frac{\mu_{j+1}}{D^{TE}} S_{j+1}^{TE+}\left(z_j\right) \tag{2.63}$$

$$a_{j+1}^{HED} = -\frac{\mu_j}{D^{TE}} S_j^{TE+}\left(z_j\right) \tag{2.64}$$

$$D^{TE} = \begin{cases} 2\mu_j k_{zj}\left(\Gamma_j^{TE}\Gamma_{j+1}^{TE} - 1\right) & \mu_j = \mu_{j+1}, k_{zj} = k_{z(j+1)} \\ \mu_j k_{z(j+1)} S_{j+1}^{TE-}\left(z_j\right) S_j^{TE+}\left(z_j\right) - \mu_{j+1} k_{zj} S_{j+1}^{TE+}\left(z_j\right) S_j^{TE-}\left(z_j\right) & \text{otherwise} \end{cases} \tag{2.65}$$

At this stage, the expansion coefficients at the interface of the source layers (i.e. layers j and j+1), can be obtained using equations (2.61) and (2.62). To calculate the coefficients for all the remaining layers, equation (2.56) can be re-written as follows:

$$A_i = A_{i+1} \frac{\mu_{i+1} S_{i+1}^{TE+}\left(z_i\right)}{\mu_i S_i^{TE+}\left(z_i\right)} \tag{2.66}$$

$$A_{i+1} = A_i \frac{\mu_i S_i^{TE+}\left(z_i\right)}{\mu_{i+1} S_{i+1}^{TE+}\left(z_i\right)} \tag{2.67}$$

These equations allow us to obtain all the remaining coefficients starting from the interface layers above and below the source and using an outward recursive algorithm. Equation (2.66) is used for the calculating the coefficients at the layers above the jth interface, while equation (2.67) is used for calculating the coefficients at the layers below the (j+1) layer interface.

After applying the inner and outer recurrence procedures, all the electromagnetic field components can be obtained. Figure 2.3 shows the summary of the recurrence technique discussed for the TE system.

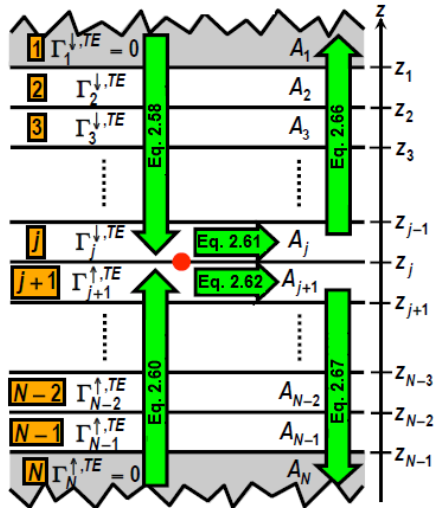

Figure 2.3: Summary for the inward and outward recurrence techniques used to calculate the spectral domain coefficients of the TE system.

2.4.2 Solution of the TM System

The solution of the TM system is very similar to the TE system. At a source-free interface, the tangential field components are continuous. Using equations (2.30), (2.32), and setting the currents into zero, we obtain the following equations:

$$-\frac{k_y k_{z(j+1)}}{k_\rho^2} B_{i+1} S_{i+1}^{TM-}\left(z_i\right) + \frac{k_y k_{zi}}{k_\rho^2} B_i S_i^{TM-}\left(z_i\right) = 0 \tag{2.68}$$

$$-\frac{\omega\varepsilon_{i+1} k_x}{k_\rho^2} B_{i+1} S_{i+1}^{TM+}\left(z_i\right) + \frac{\omega\varepsilon_i k_x}{k_\rho^2} B_i S_i^{TM+}\left(z_j\right) = 0 \tag{2.69}$$

After some mathematical manipulations, the reflection coefficient at the i+1 layer can be expressed in terms of that at the ith layer as follows:

$$\Gamma_{i+1}^{TM}\left(z_i\right) = \frac{R_{i+1,i}^{TM} + \Gamma_i^{TM} e^{j2k_{zi}z_i}}{1 + R_{i+1,i}^{TM}\Gamma_i^{TM} e^{j2k_{zi}z_i}} e^{-j2k_{z(i+1)}z_i} \tag{2.70}$$

$$R_{i,i+1}^{TM} = \frac{\varepsilon_{i+1}k_{zi} - \varepsilon_i k_{z(i+1)}}{\varepsilon_{i+1}k_{zi} + \varepsilon_i k_{z(i+1)}} \tag{2.71}$$

$$\Gamma_i^{TM}\left(z_i\right) = \frac{R_{i,i+1}^{TM} + \Gamma_{i+1}^{TM} e^{-j2k_{z(i+1)}z_i}}{1 + R_{i,i+1}^{TM}\Gamma_{i+1}^{TM} e^{-j2k_{z(i+1)}z_i}} e^{j2k_{zi}z_i} \tag{2.72}$$

Similar to the TE system, the reflection coefficient for the TM system at a certain layer can be determined in a recursive way in terms of the reflection coefficient of its above (below) layer starting from the first (bottom) layer where $\Gamma_1^{TM}=0\left(\Gamma_N^{TM}=0\right)$, until the interface layer of the source.

The boundary conditions along the source interface can be obtained for the TM system by solving equations (2.30), (2.32), (2.39), and (2.41). After some mathematical calculations, the coefficients B_j, and B_{j+1} can be obtained as follows:

$$B_j = k_\rho^2\left(\frac{b_j^{HED}}{k_x}\tilde{J}_{xj}^{TM} + b_j^{VED}\tilde{J}_{zj}^{TM}\right) \tag{2.73}$$

$$B_{j+1} = k_\rho^2\left(\frac{b_{j+1}^{HED}}{k_x}\tilde{J}_{xj}^{TM} + b_{j+1}^{VED}\tilde{J}_{zj}^{TM}\right) \tag{2.74}$$

where,

$$b_j^{HED} = \frac{k_{z(j+1)}}{\omega D^{TM}} S_{j+1}^{TM-}\left(z_j\right) \tag{2.75}$$

$$b_{j+1}^{HED} = \frac{k_{zj}}{\omega D^{TM}} S_j^{TM-}\left(z_j\right) \tag{2.76}$$

$$b_j^{VED} = \frac{\varepsilon_{j+1}}{\omega\varepsilon_j D^{TM}} S_{j+1}^{TM+}\left(z_j\right) \tag{2.77}$$

$$b_{j+1}^{VED} = \frac{1}{\omega D^{TM}} S_j^{TM+}\left(z_j\right) \tag{2.78}$$

$$D^{TM} = \begin{cases} 2\varepsilon_j k_{zj}\left(\Gamma_j^{TM}\Gamma_{j+1}^{TM}-1\right) & \varepsilon_j=\varepsilon_{j+1}, k_{zj}=k_{z(j+1)} \\ \varepsilon_j k_{z(j+1)} S_{j+1}^{TM-}\left(z_j\right) S_j^{TM+}\left(z_j\right) - \varepsilon_{j+1} k_{zj} S_{j+1}^{TM+}\left(z_j\right) S_j^{TM-}\left(z_j\right) & \text{otherwise} \end{cases} \tag{2.79}$$

These equations present the expansion coefficients at the interface of the source layers i.e. layers j, and j+1. For the remaining layers, the expansion coefficients can be obtained by re-writing equation (2.69). Hence, we obtain the following equations:

$$B_i = B_{i+1}\frac{\varepsilon_{i+1} S_{i+1}^{TM+}\left(z_i\right)}{\varepsilon_i S_i^{TM+}\left(z_i\right)} \tag{2.80}$$

$$B_{i+1} = B_i\frac{\varepsilon_i S_i^{TM+}\left(z_i\right)}{\varepsilon_{i+1} S_{i+1}^{TM+}\left(z_i\right)} \tag{2.81}$$

At this stage, all the coefficients can be obtained starting from the interface layers above and below the source and using an outward recursive algorithm. Equation (2.80) is used for the calculating the coefficients at the layers above the jth interface, while equation (2.81) is used for calculating the coefficients at the layers below the (j+1) layer interface.

Figure 2.4 shows the summary for the recurrence technique discussed for the TM system. Afterwards, all the electromagnetic fields can be obtained.

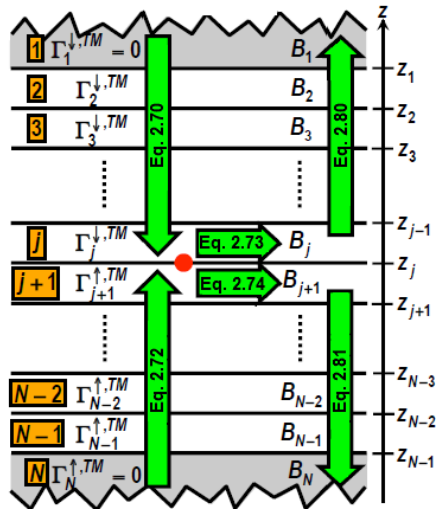

Figure 2.4: Summary for the inward and outward recurrence techniques used to calculate the spectral domain coefficients of the TM system.

2.5 Recombination of the TE and TM Systems

The complete set of the electromagnetic fields can be obtained from equations (2.20) – (2.24) and (2.28) – (2.32) for the TE and TM systems respectively. Combining the solutions of both systems using superposition, the spectral domain electric field can be expressed in matrix form as follows [70]:

$$\begin{bmatrix} \tilde{E}_{xi} \\ \tilde{E}_{yi} \\ \tilde{E}_{zi} \end{bmatrix} = \begin{bmatrix} \tilde{G}_{ij}^{E_\ell,J_\ell} + (-jk_x)(-jk_x)\tilde{G}_{ij}^{E_\ell,J'_\ell} & (-jk_x)(-jk_y)\tilde{G}_{ij}^{E_\ell,J'_\ell} & (-jk_x)\tilde{G}_{ij}^{\prime E_\ell,J_z} \\ (-jk_y)(-jk_x)\tilde{G}_{ij}^{E_\ell,J'_\ell} & \tilde{G}_{ij}^{E_\ell,J_\ell} + (-jk_y)(-jk_y)\tilde{G}_{ij}^{E_\ell,J'_\ell} & (-jk_y)\tilde{G}_{ij}^{\prime E_\ell,J_z} \\ (-jk_x)\tilde{G}_{ij}^{\prime E_z,J'_\ell} & (-jk_y)\tilde{G}_{ij}^{\prime E_z,J'_\ell} & \tilde{G}_{ij}^{\prime E_z,J_z} \end{bmatrix} \begin{bmatrix} \tilde{J}_{xj} \\ \tilde{J}_{yj} \\ \tilde{J}_{zj} \end{bmatrix} \qquad (2.82)$$

where $\tilde{G}_{ij}^{E_\ell,J_\ell}$, $\tilde{G}_{ij}^{E_\ell,J'_\ell}$, $\tilde{G}_{ij}^{\prime E_\ell,J_z}$, $\tilde{G}_{ij}^{\prime E_z,J'_\ell}$, $\tilde{G}_{ij}^{\prime E_z,J_z}$ are appropriate spectral domain Green's functions that link the current of the jth strip to the electric field at the ith strip [71]. The superscript of any Green's function consists of two parts: the first part is orientation of the electric field to be calculated, being either lateral E_ℓ, or z-directed E_z. The second part is the type and orientation of the source, which is J_ℓ, J'_ℓ, J_z, or J'_z indicating lateral current, derivative of lateral current, z-directed current, or derivative of z-directed current,

respectively. The expressions of the Green's functions are given by:

$$\tilde{G}_{ij}^{E_\ell,J_\ell} = -\omega\mu_i a_i^{HED} S_i^{TE+}(z) \tag{2.83}$$

$$\tilde{G}_{ij}^{E_\ell,J'_\ell} = -\frac{1}{k_\rho^2}\left[\omega\mu_i a_i^{HED} S_i^{TE+}(z) - k_{zi} b_i^{HED} S_i^{TM-}(z)\right] \tag{2.84}$$

$$\tilde{G}_{ij}'^{E_\ell,J_z} = -jk_{zi} b_i^{VED} S_i^{TM-}(z) \tag{2.85}$$

$$\tilde{G}_{ij}'^{E_z,J'_\ell} = jb_i^{HED} S_i^{TM+}(z) \tag{2.86}$$

$$\tilde{G}_{ij}'^{E_z,J_z} = k_\rho^2 b_i^{VED} S_i^{TM+}(z) \tag{2.87}$$

In other form, equation (2.82) can be expressed as:

$$\begin{bmatrix} \tilde{E}_{xi} \\ \tilde{E}_{yi} \\ \tilde{E}_{zi} \end{bmatrix} = \begin{bmatrix} \tilde{G}_{ij}^{E_\ell,J_\ell} + (-jk_x)(-jk_x)\tilde{G}_{ij}^{E_\ell,J'_\ell} & (-jk_x)(-jk_y)\tilde{G}_{ij}^{E_\ell,J'_\ell} & (-jk_x)\dfrac{\partial \tilde{G}_{ij}^{E_\ell,J'_z}}{\partial z} \\ (-jk_y)(-jk_x)\tilde{G}_{ij}^{E_\ell,J'_\ell} & \tilde{G}_{ij}^{E_\ell,J_\ell} + (-jk_y)(-jk_y)\tilde{G}_{ij}^{E_\ell,J'_\ell} & (-jk_y)\dfrac{\partial \tilde{G}_{ij}^{E_\ell,J'_z}}{\partial z} \\ \dfrac{\partial}{\partial z}(-jk_x)\tilde{G}_{ij}^{E_z,J'_\ell} & \dfrac{\partial}{\partial z}(-jk_y)\tilde{G}_{ij}^{E_z,J'_\ell} & \tilde{G}_{ij}^{E_z,J_z} + \dfrac{\partial^2 \tilde{G}_{ij}^{E_z,J'_z}}{\partial z^2} \end{bmatrix} \begin{bmatrix} \tilde{J}_{xj} \\ \tilde{J}_{yj} \\ \tilde{J}_{zj} \end{bmatrix} \tag{2.88}$$

where,

$$\tilde{G}_{ij}'^{E_\ell,J'_z}\Big|_{(2.82)} = \frac{\partial}{\partial z}\tilde{G}_{ij}^{E_\ell,J'_z}\Big|_{(2.88)} \tag{2.89}$$

$$\tilde{G}_{ij}'^{E_z,J'_\ell}\Big|_{(2.82)} = \frac{\partial}{\partial z}\tilde{G}_{ij}^{E_z,J'_\ell}\Big|_{(2.88)} \tag{2.90}$$

$$\tilde{G}_{ij}'^{E_z,J_z}\Big|_{(2.82)} = \tilde{G}_{ij}^{E_z,J_z} + \frac{\partial^2 \tilde{G}_{ij}^{E_z,J'_z}}{\partial z^2}\Big|_{(2.88)} \tag{2.91}$$

Comparing equations (2.82) and (2.88), it is obvious that the elements of the third row and third column of the impedance matrix are expressed differently. In equation (2.88), the differentiation with respect to "z" of the corresponding Green's functions is not performed, so the operator $\partial/\partial z$ is left. On the other hand, in equation (2.82), the differentiation with respect to "z" is carried out on the corresponding Green's functions.

The Green's functions expressions vary according to the layer structure surrounding the electric current source. In the following sections, we will investigate different layer structure cases including: homogeneous medium, two half-spaces, and three-layered medium when the source is at the top layer and the middle layers respectively.

2.6 Closed-Form Spectral Domain Green's Functions of Frequently used Layered Media

2.6.1 Source Located in Homogeneous Medium

In homogeneous medium, the Green's functions are known analytically [72] and they are given by:

$$\tilde{G}_{ij}^{E_\ell,J_\ell} = \tilde{G}_{ij}^{E_z,J_z} = \frac{-\omega\mu_i}{2}\frac{e^{-jk_{zi}|z-z_1|}}{k_{zi}} \tag{2.92}$$

$$\tilde{G}_{ij}^{E_\ell,J'_\ell} = \tilde{G}_{ij}^{E_\ell,J'_z} = \tilde{G}_{ij}^{E_z,J'_\ell} = \tilde{G}_{ij}^{E_z,J'_z} = \frac{-1}{2\omega\varepsilon_i}\frac{e^{-jk_{zi}|z-z_1|}}{k_{zi}} \tag{2.93}$$

It is clear that the Green's functions are all in the form of a constant term multiplied by an exponential term divided by k_{zi}. As a special case, when the source is located in free-space, the Green's functions can be expressed as:

$$\tilde{G}_{ij}^{E_\ell,J_\ell} = \tilde{G}_{ij}^{E_z,J_z} = \frac{-\omega\mu_0}{2}\frac{e^{-jk_{z_0}|z-z_1|}}{k_{z_0}} \tag{2.94}$$

$$\tilde{G}_{ij}^{E_\ell,J'_\ell} = \tilde{G}_{ij}^{E_\ell,J'_z} = \tilde{G}_{ij}^{E_z,J'_\ell} = \tilde{G}_{ij}^{E_z,J'_z} = \frac{-1}{2\omega\varepsilon_0}\frac{e^{-jk_{z_0}|z-z_1|}}{k_{z_0}} \tag{2.95}$$

2.6.2 Source Surrounded by Top and Bottom Layered Media

The second case considered is for a source located at the top layer of a system of layered structure. In this case, the Green's functions are calculated analytically. In this case, the expressions of the Green's functions are given by:

$$\begin{aligned}\tilde{G}_{ij}^{E_\ell,J_\ell} &= \frac{-\omega\mu_1}{2}\left[\Gamma_2^{TE}\frac{e^{-jk_{z1}(z+z_1)}}{k_{z1}} + \frac{e^{-jk_{z1}|z-z_1|}}{k_{z1}}\right] \\ &= \left(g_{ij}^{E_\ell,J_\ell}\frac{e^{-jk_{z1}(z+z_1)}}{k_{z1}}\right) + \left(\frac{-\omega\mu_1}{2}\frac{e^{-jk_{z1}|z-z_1|}}{k_{z1}}\right)\end{aligned} \tag{2.96}$$

$$\begin{aligned}\tilde{G}_{ij}^{E_\ell,J'_\ell} &= \frac{\tilde{G}_{ij}^{E_\ell,J_\ell}}{k_\rho^2} - \frac{k_{z1}^2}{2\omega\varepsilon_1 k_\rho^2}\left[\Gamma_2^{TM}\frac{e^{-jk_{z1}(z+z_1)}}{k_{z1}} - \frac{e^{-jk_{z1}|z-z_1|}}{k_{z1}}\right] \\ &= \frac{-\omega\mu_1}{2k_\rho^2}\left[\Gamma_2^{TE}\frac{e^{-jk_{z1}(z+z_1)}}{k_{z1}} + \frac{e^{-jk_{z1}|z-z_1|}}{k_{z1}}\right] - \frac{k_{z1}^2}{2\omega\varepsilon_1 k_\rho^2}\left[\Gamma_2^{TM}\frac{e^{-jk_{z1}(z+z_1)}}{k_{z1}} - \frac{e^{-jk_{z1}|z-z_1|}}{k_{z1}}\right] \\ &= \left(g_{ij}^{E_\ell,J'_\ell}\frac{e^{-jk_{z1}(z+z_1)}}{k_{z1}}\right) + \left(\frac{-1}{2\omega\varepsilon_1}\right)\frac{e^{-jk_{z1}|z-z_1|}}{k_{z1}}\end{aligned} \tag{2.97}$$

$$\tilde{G}_{ij}^{E_\ell,J'_z} = \tilde{G}_{ij}^{E_z,J'_z} = \frac{-1}{2\omega\varepsilon_1}\left[\Gamma_2^{TM}\frac{e^{-jk_{z1}(z+z_1)}}{k_{z1}} + \frac{e^{-jk_{z1}|z-z_1|}}{k_{z1}}\right]$$
$$= \left(g_{ij}^{E_\ell,J'_z}\frac{e^{-jk_{z1}(z+z_1)}}{k_{z1}}\right) + \left(\frac{-1}{2\omega\varepsilon_1}\frac{e^{-jk_{z1}|z-z_1|}}{k_{z1}}\right) \tag{2.98}$$
$$= \left(g_{ij}^{E_z,J'_z}\frac{e^{-jk_{z1}(z+z_1)}}{k_{z1}}\right) + \left(\frac{-1}{2\omega\varepsilon_1}\frac{e^{-jk_{z1}|z-z_1|}}{k_{z1}}\right)$$

$$\tilde{G}_{ij}^{E_z,J'_\ell} = \frac{1}{2\omega\varepsilon_1}\left[\Gamma_2^{TM}\frac{e^{-jk_{z1}(z+z_1)}}{k_{z1}} - \frac{e^{-jk_{z1}|z-z_1|}}{k_{z1}}\right]$$
$$= \left(g_{ij}^{E_z,J'_\ell}\frac{e^{-jk_{z1}(z+z_1)}}{k_{z1}}\right) + \left(\frac{-1}{2\omega\varepsilon_1}\frac{e^{-jk_{z1}|z-z_1|}}{k_{z1}}\right) \tag{2.99}$$

$$\tilde{G}_{ij}^{E_z,J_z} = \frac{-\omega\mu_1}{2}\left[\Gamma_2^{TM}\frac{e^{-jk_{z1}(z+z_1)}}{k_{z1}} + \frac{e^{-jk_{z1}|z-z_1|}}{k_{z1}}\right]$$
$$= \left(g_{ij}^{E_z,J_z}\frac{e^{-jk_{z1}(z+z_1)}}{k_{z1}}\right) + \left(\frac{-\omega\mu_1}{2}\frac{e^{-jk_{z1}|z-z_1|}}{k_{z1}}\right) \tag{2.100}$$

where ε_1 is the dielectric constant of the upper half space, k_{z1} is propagation constant along the direction of stratification: $k_{z1}^2 = k_1^2 - k_\rho^2$, where $k_\rho^2 = k_x^2 + k_y^2$. Γ_2^{TE}, and Γ_2^{TM} are the reflection coefficients in the second layer of the TE and TM systems respectively. It is assumed the source and observer are located at z_1 and z respectively. It is clear that in this case, each Green's function consists of two exponential terms. The terms $g_{ij}^{E_\ell,J_\ell}$, $g_{ij}^{E_\ell,J'_\ell}$, $g_{ij}^{E_\ell,J'_z}$, $g_{ij}^{E_z,J'_z}$, $g_{ij}^{E_z,J'_\ell}$, $g_{ij}^{E_z,J_z}$ defined in equations (2.96) – (2.100) are the first terms of the basic spectral domain Green functions excluding the $e^{-jk_{z1}(z+z_1)}/k_{z1}$.

2.6.2.1 Source in a Half-Space Backed by another Half-Space

In this section, we investigate the expressions of the Green's functions when the source is located within one of two half-spaces, as shown in Figure 2.5. Specifically, a source that is located in free-space and backed by Silicon Dioxide (SiO_2) is considered in this section. Using the equations (2.58) – (2.60) and (2.70) – (2.72) the reflection coefficients Γ_2^{TE} , and Γ_2^{TM} can be expressed as:

$$\Gamma_2^{TE} = R_{2,1}^{TE}\, e^{j2k_{z_1}z_2} \tag{2.101}$$

$$R_{2,1}^{TE} = \frac{\mu_2 k_{z_1} - \mu_1 k_2}{\mu_2 k_{z_1} + \mu_1 k_2} \tag{2.102}$$

$$\Gamma_2^{TM} = R_{1,2}^{TM} e^{j2k_{z_1} z_2} \tag{2.103}$$

$$R_{1,2}^{TM} = \frac{\varepsilon_2 k_{z_1} - \varepsilon_1 k_{z_2}}{\varepsilon_2 k_{z_1} + \varepsilon_1 k_{z_2}} \tag{2.104}$$

where z_2 is the z-location of the interface between the two half-spaces.

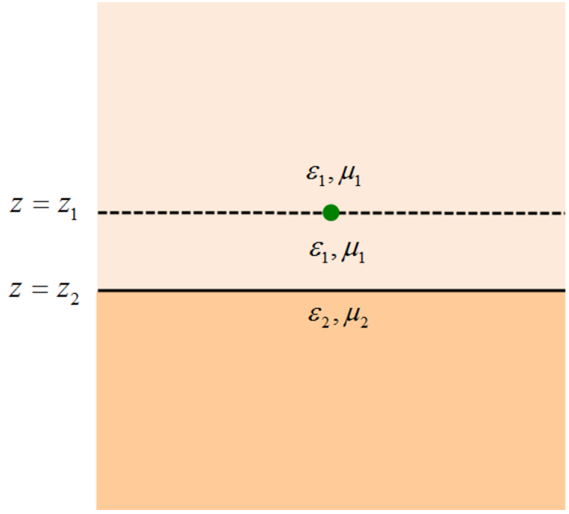

Figure 2.5: Current source located at the interface of two half-spaces.

Substituting in equations (2.96) – (2.100), the coefficients of the first exponential term are plotted in Figures (2.6) – (2.10). These coefficients are calculated at frequency = 193.55 THz (λ = 1.55 μm). These coefficients are independent of the location of the current source. The second components of the Green's functions are exactly like the expressions of the Green's functions in free-space. It is clear from figures (2.6) – (2.10) that the basic Green's functions are strongly varying at the low-spectral values, while at high spectral values the functions tend to saturate.

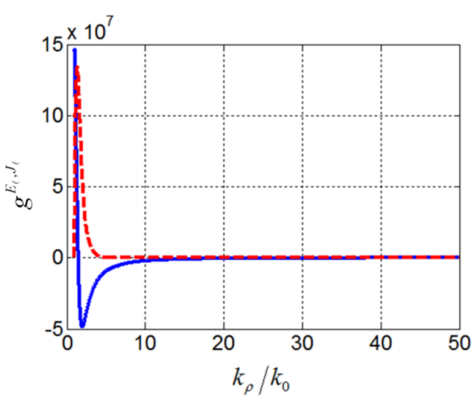

Figure 2.6: The basic Green's function g^{E_ℓ, J_ℓ} for a source located at the interface of two half-spaces (free-space and SiO_2): blue (real part), and red dashed (imaginary part).

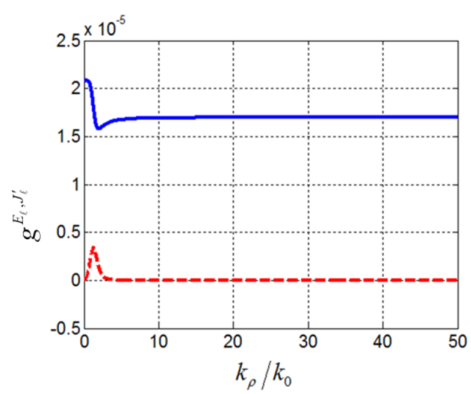

Figure 2.7: The basic Green's function $g^{E_\ell, J_\ell'}$ for a source located at the interface of two half-spaces (free-space and SiO_2): blue (real part), and red dashed (imaginary part).

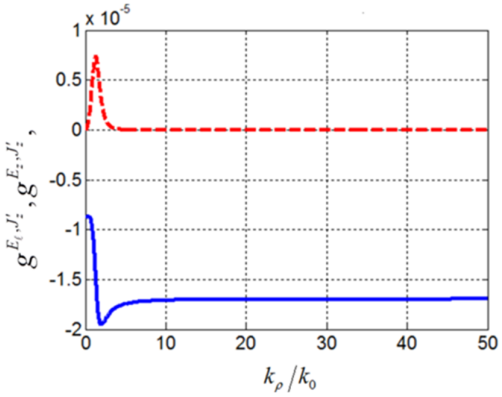

Figure 2.8: The basic Green's functions: g^{E_ℓ,J'_z}, g^{E_z,J'_z} for a source located at the interface of two half-spaces (free-space and SiO_2): blue (real part), and red dashed (imaginary part).

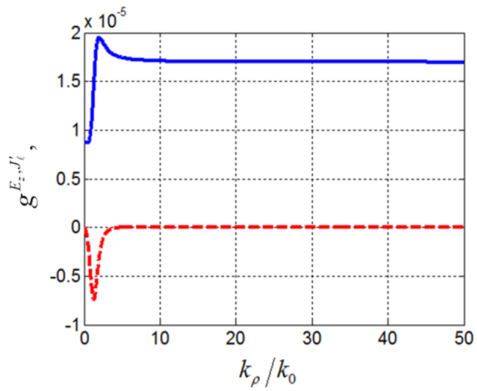

Figure 2.9: The basic Green's functions: g^{E_z,J'_ℓ} for a source located at the interface of two half-spaces (free-space and SiO_2): blue (real part), and red dashed (imaginary part).

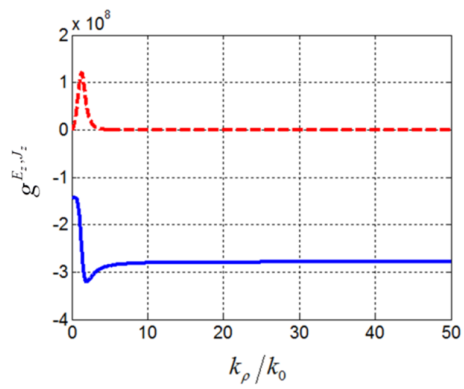

Figure 2.10: The basic Green's functions: g^{E_z,J_z} for a source located at the interface of two half-spaces (free-space and SiO_2): blue (real part), and red dashed (imaginary part).

2.6.2.2 Source Carrying Half-Space/Finite Layer/Half-Space

The second case considered is for a three-layered medium, shown in Figure 2.11. The expressions of the Green's functions are exactly as defined in Equations (2.96) – (2.100); however, the reflection coefficients are not similar to (2.101) – (2.104) due to the different layer structure. The new expressions for the reflection coefficients in this case are defined as follows:

$$\Gamma_2^{TE} = \frac{R_{2,1}^{TE} + \Gamma_3^{TE} e^{-j2k_{z_2}z_2}}{1 + R_{2,1}^{TE}\Gamma_3^{TE} e^{-j2k_{z_2}z_2}} e^{j2k_{z_1}z_2} \tag{2.105}$$

$$\Gamma_2^{TM} = \frac{R_{1,2}^{TM} + \Gamma_3^{TM} e^{-j2k_{z_2} z_2}}{1 + R_{1,2}^{TM} \Gamma_3^{TM} e^{-j2k_{z_2} z_2}} e^{j2k_{z_1} z_2} \tag{2.106}$$

where,

$$\Gamma_3^{TE} = R_{3,2}^{TE} \, e^{j2k_{z_2} z_3} \tag{2.107}$$

$$R_{3,2}^{TE} = \frac{\mu_3 k_{z_2} - \mu_2 k_{z_3}}{\mu_3 k_{z_2} + \mu_2 k_{z_3}} \tag{2.108}$$

$$\Gamma_3^{TM} = R_{2,3}^{TM} \, e^{j2k_{z_2} z_3} \tag{2.109}$$

$$R_{2,3}^{TM} = \frac{\varepsilon_3 k_{z_2} - \varepsilon_2 k_{z_3}}{\varepsilon_3 k_{z_2} + \varepsilon_2 k_{z_3}} \tag{2.110}$$

where z_2, and z_3 are the z-locations of the layer1/layer2 and layer2/layer3 interfaces respectively.

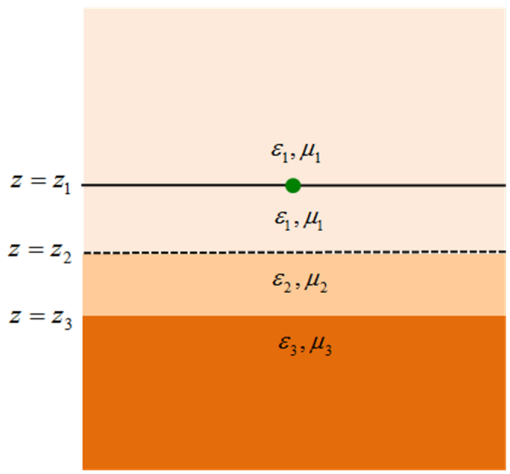

Figure 2.11: Current source located at the top layer of a three-layered medium structure.

2.6.3 Half-Space/Source Carrying Layer/Half-Space

The last case considered is for a three-layered medium with an electric current source located at the middle layer, as shown in Figure 2.12. As shown, the source is located within a finite thickness layer. The adjacent upper and lower layers are assumed to be open half-spaces.

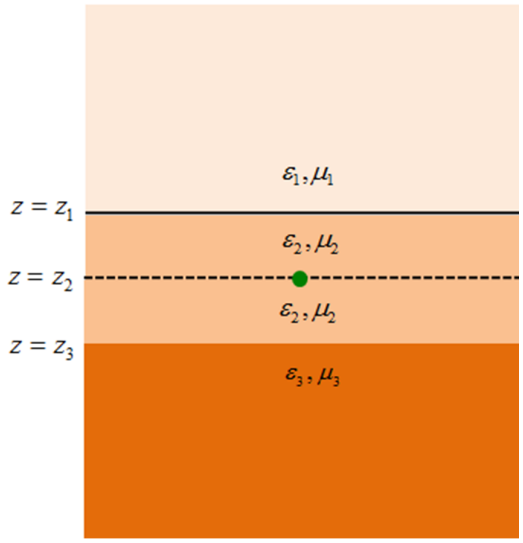

Figure 2.12: Current source located at the middle layer of a three-layered medium structure.

In this case, the Green's functions consist of four terms and are given by the following equations:

$$\tilde{G}_{ij}^{E_\ell,J_\ell} = \frac{\omega\mu_2}{2\left(\Gamma_2^{TE}\Gamma_3^{TE}-1\right)}\left[\Gamma_3^{TE}\frac{e^{-jk_{z_2}(z+z_2)}}{k_{z_2}}+\Gamma_3^{TE}\Gamma_2^{TE}\frac{e^{jk_{z_2}|z-z_2|}}{k_{z_2}}+\Gamma_2^{TE}\frac{e^{jk_{z_2}(z+z_2)}}{k_{z_2}}+\frac{e^{-jk_{z_2}|z-z_2|}}{k_{z_2}}\right] \tag{2.111}$$
$$=\left(g_1^{E_\ell,J_\ell}\frac{e^{-jk_{z_2}(z+z_2)}}{k_{z_2}}\right)+\left(g_2^{E_\ell,J_\ell}\frac{e^{jk_{z_2}|z-z_2|}}{k_{z_2}}\right)+\left(g_3^{E_\ell,J_\ell}\frac{e^{jk_{z_2}(z+z_2)}}{k_{z_2}}\right)+\left(g_4^{E_\ell,J_\ell}\frac{e^{-jk_{z_2}|z-z_2|}}{k_{z_2}}\right)$$

$$\tilde{G}_{ij}^{E_\ell,J'_\ell} = \frac{\tilde{G}_{ij}^{E_\ell,J_\ell}}{k_\rho^2}+\frac{k_{z_2}^2}{2\omega\varepsilon_2 k_\rho^2 B}\left(\Gamma_3^{TM}\frac{e^{-jk_{z_2}(z+z_2)}}{k_{z_2}}-\Gamma_3^{TM}\Gamma_2^{TM}\frac{e^{jk_{z_2}|z-z_2|}}{k_{z_2}}+\Gamma_2^{TM}\frac{e^{jk_{z_2}(z+z_2)}}{k_{z_2}}-\frac{e^{-jk_{z_2}|z-z_2|}}{k_{z_2}}\right) \tag{2.112}$$
$$=\left(g_1^{E_\ell,J'_\ell}\frac{e^{-jk_{z_2}(z+z_2)}}{k_{z_2}}\right)+\left(g_2^{E_\ell,J'_\ell}\frac{e^{jk_{z_2}|z-z_2|}}{k_{z_2}}\right)+\left(g_3^{E_\ell,J'_\ell}\frac{e^{jk_{z_2}(z+z_2)}}{k_{z_2}}\right)+\left(g_4^{E_\ell,J'_\ell}\frac{e^{-jk_{z_2}|z-z_2|}}{k_{z_2}}\right)$$

$$\tilde{G}_{ij}^{E_\ell,J'_z} = \tilde{G}_{ij}'^{E_z,J_z'} = \frac{1}{2\omega\varepsilon_2 B}\left[\frac{\Gamma_3^{TM}e^{-jk_{z_2}(z+z_2)}}{k_{z_2}}+\frac{\Gamma_3^{TM}\Gamma_2^{TM}e^{jk_{z_2}|z-z_2|}}{k_{z_2}}+\frac{\Gamma_2^{TM}e^{jk_{z_2}(z+z_2)}}{k_{z_2}}+\frac{e^{-jk_{z_2}|z-z_2|}}{k_{z_2}}\right] \tag{2.113}$$
$$=\left(g_1^{E_\ell,J'_z}\frac{e^{-jk_{z_2}(z+z_2)}}{k_{z_2}}\right)+\left(g_2^{E_\ell,J'_z}\frac{e^{jk_{z_2}|z-z_2|}}{k_{z_2}}\right)+\left(g_3^{E_\ell,J'_z}\frac{e^{jk_{z_2}(z+z_2)}}{k_{z_2}}\right)+\left(g_4^{E_\ell,J'_z}\frac{e^{-jk_{z_2}|z-z_2|}}{k_{z_2}}\right)$$

$$\tilde{G}_{ij}'^{E_z,J'_\ell} = \frac{1}{2\omega\varepsilon_2 B}\left[\frac{-\Gamma_3^{TM}e^{-jk_{z_2}(z+z_2)}}{k_{z_2}}+\Gamma_3^{TM}\Gamma_2^{TM}\frac{e^{jk_{z_2}|z-z_2|}}{k_{z_2}}-\frac{\Gamma_2^{TM}e^{jk_{z_2}(z+z_2)}}{k_{z_2}}+\frac{e^{-jk_{z_2}|z-z_2|}}{k_{z_2}}\right] \tag{2.114}$$
$$=\left(g_1^{E_z,J'_\ell}\frac{e^{-jk_{z_2}(z+z_2)}}{k_{z_2}}\right)+\left(g_2^{E_z,J'_\ell}\frac{e^{jk_{z_2}|z-z_2|}}{k_{z_2}}\right)+\left(g_3^{E_z,J'_\ell}\frac{e^{jk_{z_2}(z+z_2)}}{k_{z_2}}\right)+\left(g_4^{E_z,J'_\ell}\frac{e^{-jk_{z_2}|z-z_2|}}{k_{z_2}}\right)$$

$$\tilde{G}_{ij}'^{E_z,J_z} = \frac{\omega\mu_2}{2B}\left[\Gamma_3^{TM}\frac{e^{-jk_{z_2}(z+z_2)}}{k_{z_2}} + \Gamma_3^{TM}\Gamma_2^{TM}\frac{e^{jk_{z_2}|z-z_2|}}{k_{z_2}} + \Gamma_2^{TM}\frac{e^{jk_{z_2}(z+z_2)}}{k_{z_2}} + \frac{e^{-jk_{z_2}|z-z_2|}}{k_{z_2}}\right] \tag{2.115}$$

$$= \left(g_1^{E_z,J_z}\frac{e^{-jk_{z_2}(z+z_2)}}{k_{z_2}}\right) + \left(g_2^{E_z,J_z}\frac{e^{jk_{z_2}|z-z_2|}}{k_{z_2}}\right) + \left(g_3^{E_z,J_z}\frac{e^{jk_{z_2}(z+z_2)}}{k_{z_2}}\right) + \left(g_4^{E_z,J_z}\frac{e^{-jk_{z_2}|z-z_2|}}{k_{z_2}}\right)$$

where,

$$A = \left(\Gamma_2^{TE}\Gamma_3^{TE} - 1\right) \tag{2.116}$$

$$B = \left(\Gamma_2^{TM}\Gamma_3^{TM} - 1\right) \tag{2.117}$$

$$\Gamma_2^{TE} = R_{1,2}^{TE}\, e^{-j2k_{z_2}z_1} \tag{2.118}$$

$$R_{1,2}^{TE} = \frac{\mu_1 k_{z_2} - \mu_2 k_{z_1}}{\mu_1 k_{z_2} + \mu_2 k_{z_1}} \tag{2.119}$$

$$\Gamma_2^{TM} = R_{2,1}^{TM}\, e^{-j2k_{z_2}z_1} \tag{2.120}$$

$$R_{2,1}^{TM} = \frac{\varepsilon_1 k_{z_2} - \varepsilon_2 k_{z_1}}{\varepsilon_1 k_{z_2} + \varepsilon_2 k_{z_1}} \tag{2.121}$$

$$\Gamma_3^{TE} = R_{3,2}^{TE}\, e^{j2k_{z_2}z_3} \tag{2.122}$$

$$R_{3,2}^{TE} = \frac{\mu_3 k_{z_2} - \mu_2 k_{z_3}}{\mu_3 k_{z_2} + \mu_2 k_{z_3}} \tag{2.123}$$

$$\Gamma_3^{TM} = R_{2,3}^{TM}\, e^{j2k_{z_2}z_3} \tag{2.124}$$

$$R_{2,3}^{TM} = \frac{\varepsilon_3 k_{z_2} - \varepsilon_2 k_{z_3}}{\varepsilon_3 k_{z_2} + \varepsilon_2 k_{z_3}} \tag{2.125}$$

For a current source located inside SiO_2 layer while the upper and lower half spaces are free-space and Indium-Tin Oxide (ITO) , $\varepsilon_r = 4$, respectively, the coefficients of the spectral domain Green's functions are plotted in Figures (2.13) – (2.17), as calculated at frequency = 193.55 THz (λ = 1.55 μm).

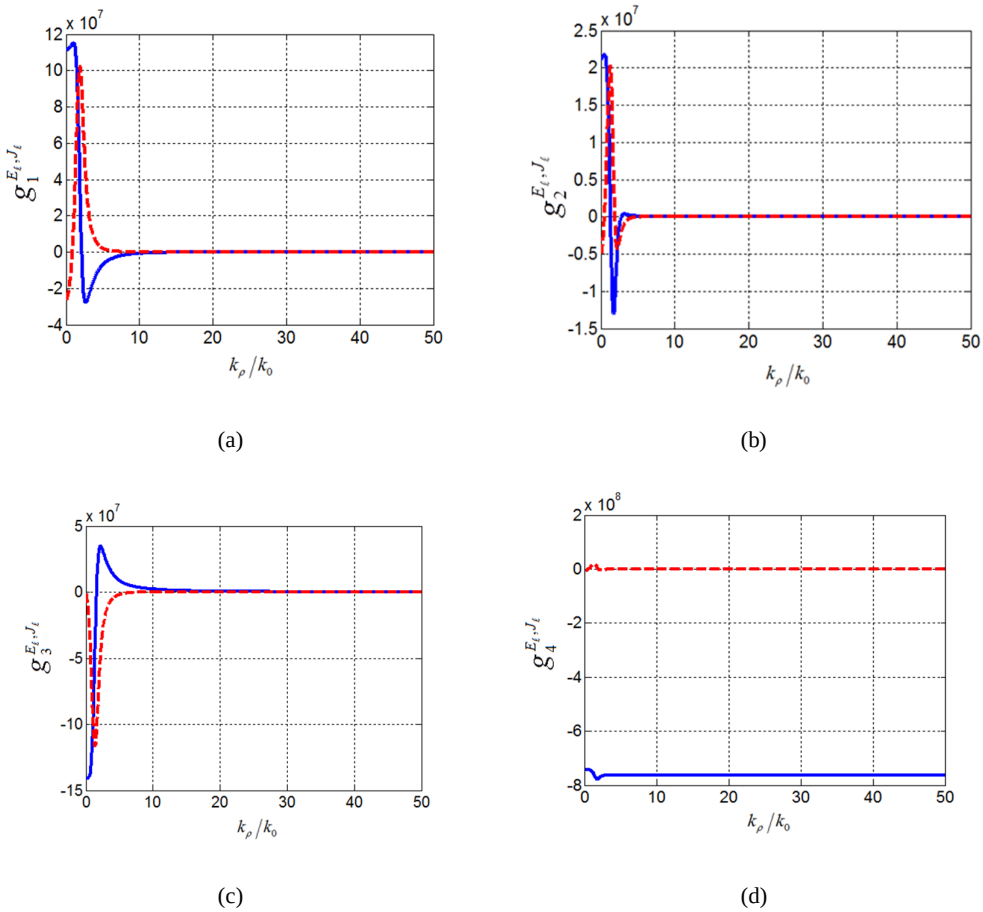

Figure 2.13: The basic Green's functions for a source located in the middle layer of three-layered structure (free-space/SiO_2/ITO) (a) $g_1^{E_\ell,J_\ell}$, (b) $g_2^{E_\ell,J_\ell}$, (c) $g_3^{E_\ell,J_\ell}$, and (d) $g_4^{E_\ell,J_\ell}$: blue (real part), and red dashed (imaginary part).

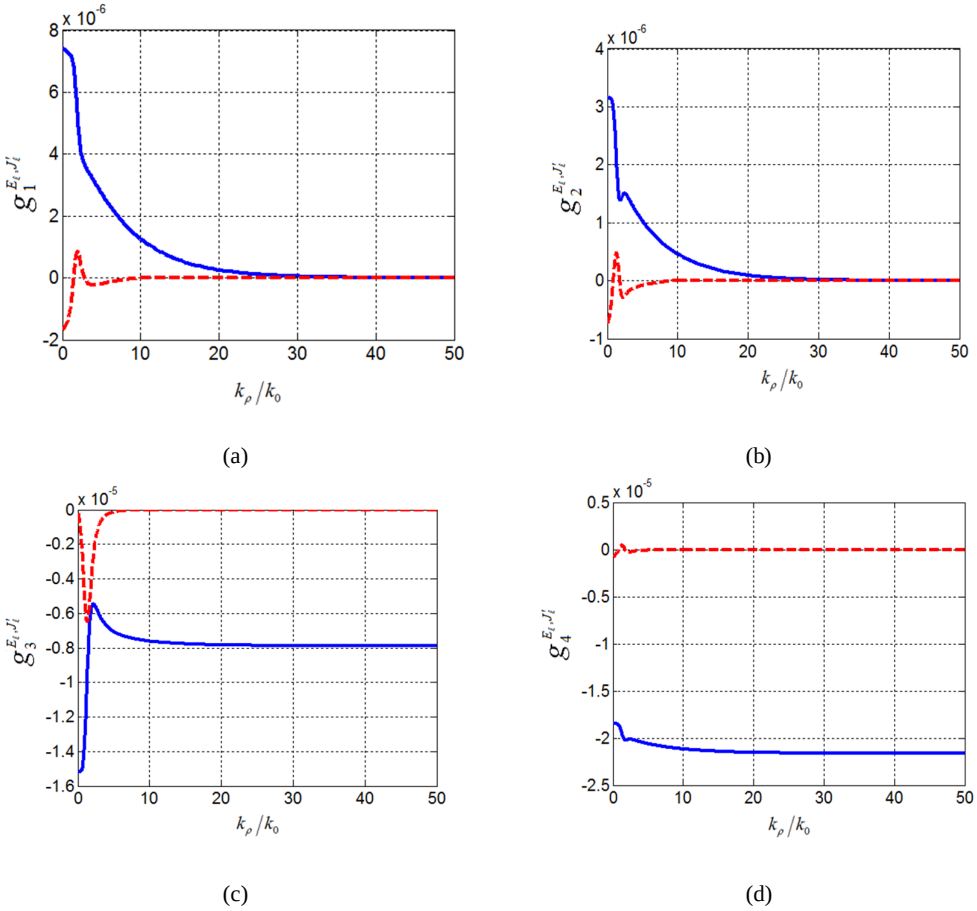

Figure 2.14: The basic Green's functions for a source located in the middle layer of three-layered structure (free-space/SiO_2/ITO) (a) $g_1^{E_\ell,J_\ell^i}$, (b) $g_2^{E_\ell,J_\ell^i}$, (c) $g_3^{E_\ell,J_\ell^i}$, and (d) $g_4^{E_\ell,J_\ell^i}$: blue (real part), and red dashed (imaginary part).

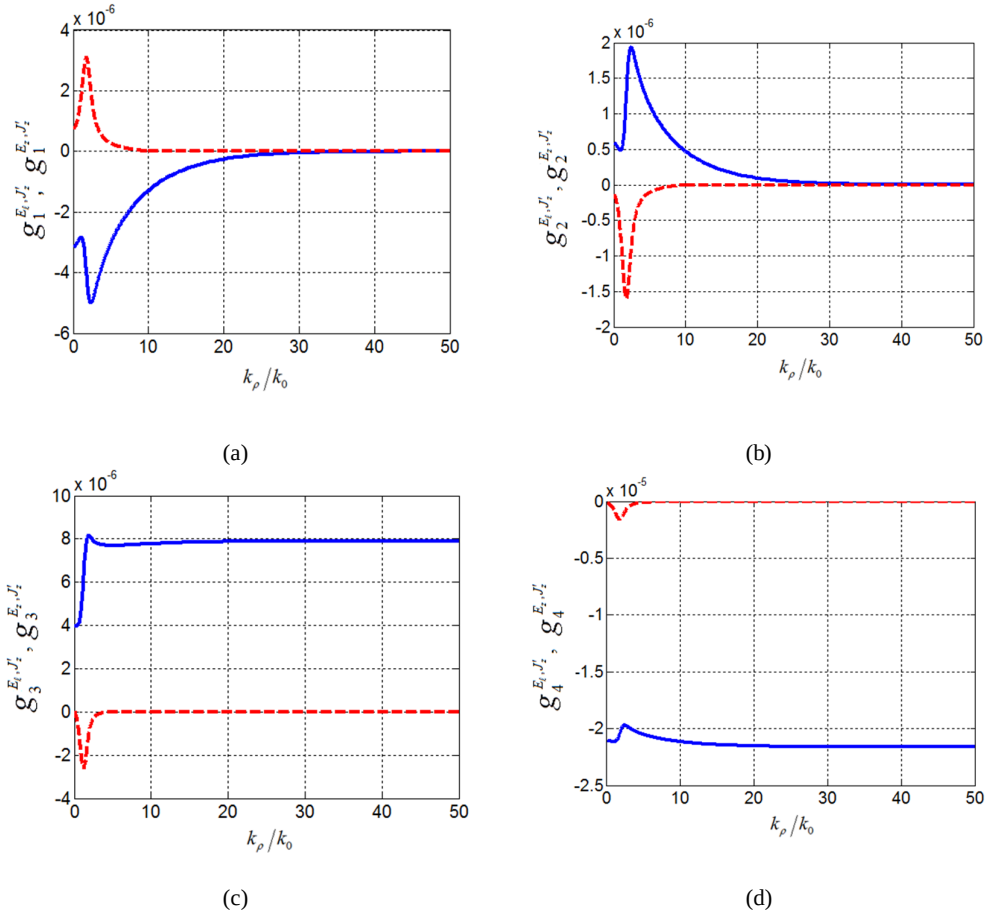

Figure 2.15: The basic Green's functions for a source located in the middle layer of three-layered structure (free-space/SiO_2/ITO) (a) $g_1^{E_\ell,J_z'}\left(g_1^{E_z,J_z'}\right)$, (b) $g_2^{E_\ell,J_z'}\left(g_2^{E_z,J_z'}\right)$, (c) $g_3^{E_\ell,J_z'}\left(g_3^{E_z,J_z'}\right)$, and (d) $g_4^{E_\ell,J_z'}\left(g_4^{E_z,J_z'}\right)$: blue (real part), and red dashed (imaginary part).

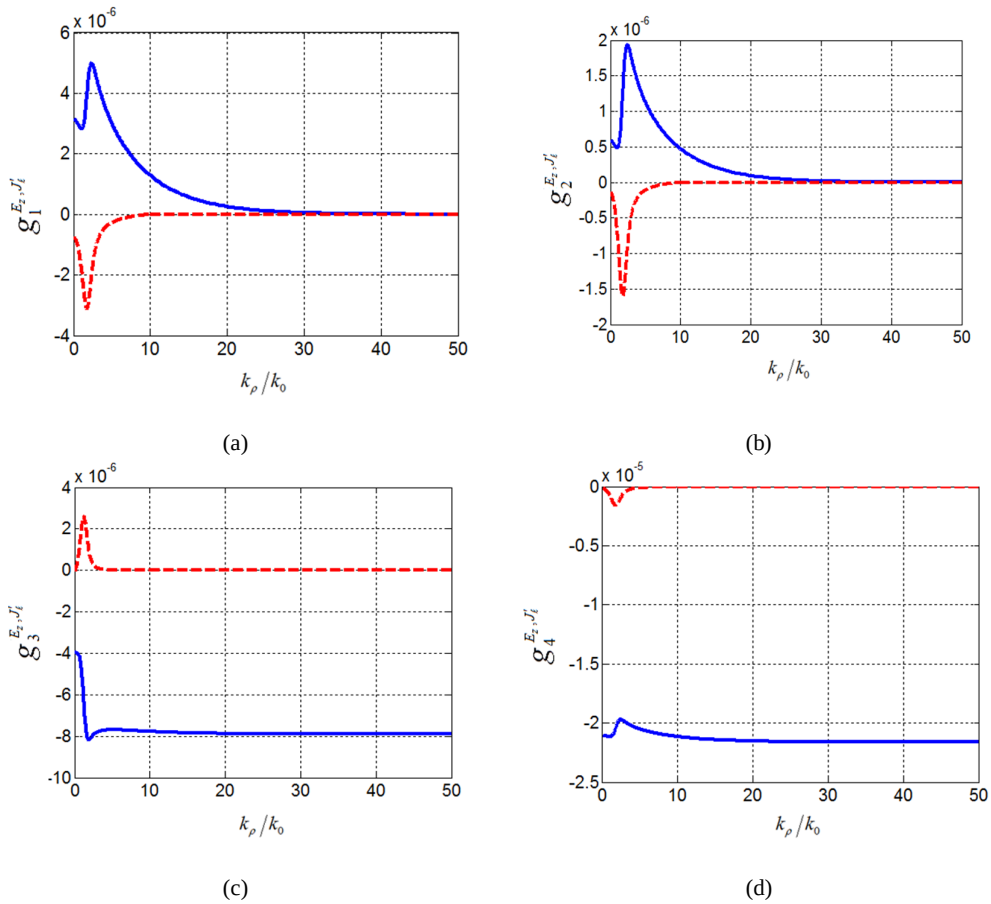

Figure 2.16: The basic Green's functions: for a source located in the middle layer of three-layered structure (free-space/SiO_2/ITO) (a) $g_1^{E_z,J_\ell^t}$, (b) $g_2^{E_z,J_\ell^t}$, (c) $g_3^{E_z,J_\ell^t}$, and (d) $g_4^{E_z,J_\ell^t}$: blue (real part), and red dashed (imaginary part).

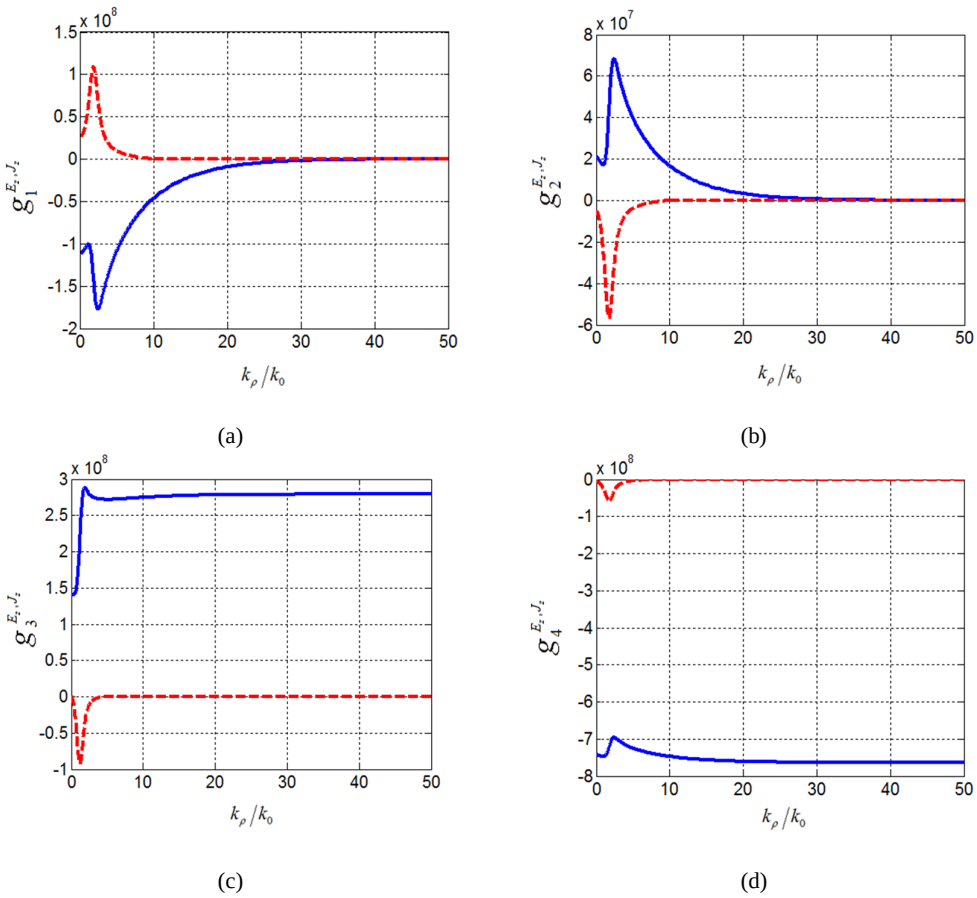

Figure 2.17: The basic Green's functions: for a source located in the middle layer of three-layered structure (free-space/SiO_2/ITO) (a) $g_1^{E_z,J_z}$, (b) $g_2^{E_z,J_z}$, (c) $g_3^{E_z,J_z}$, and (d) $g_4^{E_z,J_z}$: blue (real part), and red dashed (imaginary part).

2.7 Spatial Domain Green's Functions

In spatial domain, the electric fields are obtained from their spectral domain counterparts using Fourier transform. In matrix form, the spatial domain electric fields are expressed as:

$$\begin{bmatrix} E_{xi} \\ E_{yi} \\ E_{zi} \end{bmatrix} = \begin{bmatrix} G_{ij}^{E_\ell,J_\ell} + \frac{\partial^2}{\partial x^2} G_{ij}^{E_\ell,J'_\ell} & \frac{\partial^2}{\partial x \partial y} G_{ij}^{E_\ell,J'_\ell} & \frac{\partial^2}{\partial x \partial z} G_{ij}^{E_\ell,J'_z} \\ \frac{\partial^2}{\partial y \partial x} G_{ij}^{E_\ell,J'_\ell} & G_{ij}^{E_\ell,J_\ell} + \frac{\partial^2}{\partial y^2} G_{ij}^{E_\ell,J'_\ell} & \frac{\partial^2}{\partial y \partial z} G_{ij}^{E_\ell,J'_z} \\ \frac{\partial^2}{\partial z \partial x} G_{ij}'^{E_z,J'_\ell} & \frac{\partial^2}{\partial z \partial y} G_{ij}^{E_z,J'_\ell} & G_{ij}^{E_z,J_z} + \frac{\partial^2}{\partial z^2} G_{ij}^{E_z,J'_z} \end{bmatrix} \begin{bmatrix} J_{xj} \\ J_{yj} \\ J_{zj} \end{bmatrix} \tag{2.126}$$

where $G_{ij}^{E_\ell,J_\ell}$, $G_{ij}^{E_\ell,J'_\ell}$, $G_{ij}^{E_\ell,J'_z}$, $G_{ij}^{E_z,J'_\ell}$, $G_{ij}^{E_z,J_z}$ and $G_{ij}^{E_z,J'_z}$ are the spatial domain counterparts of the spectral domain Green functions $\tilde{G}_{ij}^{E_\ell,J_\ell}$, $\tilde{G}_{ij}^{E_\ell,J'_\ell}$, $\tilde{G}_{ij}^{E_\ell,J'_z}$, $\tilde{G}_{ij}^{E_z,J'_\ell}$, $\tilde{G}_{ij}^{E_z,J_z}$ and $\tilde{G}_{ij}^{E_z,J'_z}$ respectively. Similar to the spectral domain Green's functions, each spatial domain Green's function can be described by two superscripts.

In the previous section, the spectral domain Green's functions are derived analytically for several layer structures. The spatial domain Green's functions for filament sources can be obtained from their spectral domain counterparts using the following Sommerfeld identity [73–74]:

$$G_{ij}(x,z) = \frac{1}{2\pi} \int_{-\infty}^{\infty} \tilde{G}_{ij}(k_x,z) e^{jk_x(x-x')} dk_x = \frac{1}{\pi} \int_0^{\infty} \tilde{G}_{ij}(k_x,z) \cos\left(k_x(x-x')\right) dk_x \tag{2.127}$$

Nevertheless, calculating the integration in equation (2.127) is numerically inefficient and time consuming. This is due to the slowly decaying and highly oscillatory nature of the integrand [75]. However, if the spectral Green's function is expanded in the form of exponentials divided by k_{z1}, the Sommerfeld integration can be evaluated analytically using the following equation [76]:

$$\int_0^{\infty} \frac{e^{-jk_{zi}(z \pm z_1)}}{k_{zi}} \cos\left(k_x(x-x')\right) dk_x = jK_0\left(\gamma\sqrt{(x-x')^2 + (z \pm z')^2}\right) \qquad \begin{array}{l} \mathrm{Re}\left|z \pm z'\right| > 0, \\ \mathrm{Re}\,\gamma > 0, \left|x - x'\right| > 0 \end{array} \tag{2.128}$$

where $\gamma = \sqrt{k_y^2 - k_i^2}$, K_0 is the modified Bessel function of the second kind and zero order. The Discrete Complex Image Method (DCIM) [77–79] can perform this task. It begins by approximating the function (the spectral domain Green's functions in our case) into a series of complex exponentials. In this work, the Generalized Pencil of Function (GPOF) [80] method is adopted for this approximation. Compared to Prony's [81] method, GPOF is more stable, more efficient, and less sensitive to numerical noise [82]. Afterwards, the inverse Fourier transform of the obtained series of exponentials can be calculated analytically. It is worth mentioning that the GPOF method requires uniform sampling of the function to be approximated. Doing this, any function $f(t)$ can be expressed as:

$$f(t) = \sum_{n=1}^{N} w_n e^{\alpha_n t} \tag{2.129}$$

where N is the number of terms required to approximate the function $f(t)$ and it is determined by the GPOF method, t is a variable which is sampled uniformly from 0 to t_m. w_n and α_n represent the coefficient and exponent terms of the nth term. Due to the fast variations of the spectral domain Green's functions at low spectral values, an accurate approximation of these functions requires large number of samples. On the contrary, at high spectral values, the spectral domain Green's functions vary slowly. Consequently, it is more efficient to perform the DCIM along two levels [83]. The first level corresponds to the high spectrum part of the function where a low sampling rate is enough for an accurate approximation. In the second level, the sampling rate must be high enough in order to capture the fast-varying behaviour of the Green's functions in the low spectrum part. Since the Sommerfeld integration along k_x starts from zero to infinity, according to equation (2.128), the sampling should cover this range. In terms of k_ρ, sampling should start from $k_\rho = k_y$ until $k_\rho = \infty$. Figure 2.18 shows the sampling paths along the k_ρ-plane for the first level (C_1) and second level (C_2) of the DCIM. The function is first discretized along the high spectral values (i.e. along C_1) starting from $k_\rho = \beta_2$ until $k_\rho = \beta_1$. The optimum choice of β_2 is to be slightly higher than the maximum propagation constant along the layered medium. The end point of the first path is taken at $\beta_1 \geq 50k_0$, depending on the dielectric permittivity of the layered structure. It is worth noting that along this level, the Green's functions are sampled along the real axis of k_x due to the absence of poles and branch cuts along the high spectrum. The second path starts at $\beta_3 = k_y$, which corresponds to $k_x = 0$, and it ends at the starting point of the first path (i.e. at β_2). It is worth noting that sampling along the real axis is not possible along this level due to the presence of poles and branch cuts resulting in singularities. Thus, path C_2 is performed along the complex plane of k_ρ, as shown in Figure 2.18. In terms of k_{zi}, the first path starts at $-j\gamma_2$, and ends at $-j\gamma_1$ whereas the second path starts at $-j\gamma_3$ and ends at $-j\gamma_2$, as shown in Figure 2.19 where:

$$k_{zi}^2 = k_i^2 - k_\rho^2 = k_i^2 - k_y^2 - k_x^2 \tag{2.130}$$

$$\gamma_1 = \sqrt{\beta_1^2 - k_i^2} \tag{2.131}$$

$$\gamma_2 = \sqrt{\beta_2^2 - k_i^2} \tag{2.132}$$

$$\gamma_3 = \sqrt{k_y^2 - k_i^2} \tag{2.133}$$

Therefore, the equations relating k_{zi} with t along the two paths C_1 and C_2 are given by:

$$k_{zi} = \begin{cases} -j\left[\gamma_2 + (\gamma_1 - \gamma_2)t\right] & \text{along } C_1 \\ -j\left[\gamma_3 + (\gamma_2 - \gamma_3)t\right] & \text{along } C_2 \end{cases} \tag{2.134}$$

$$t = \begin{cases} \dfrac{\gamma_2}{\gamma_2 - \gamma_1} - \dfrac{jk_{zi}}{\gamma_2 - \gamma_1} & \text{along } C_1 \\ \dfrac{\gamma_3}{\gamma_3 - \gamma_2} - \dfrac{jk_{zi}}{\gamma_3 - \gamma_2} & \text{along } C_2 \end{cases} \tag{2.135}$$

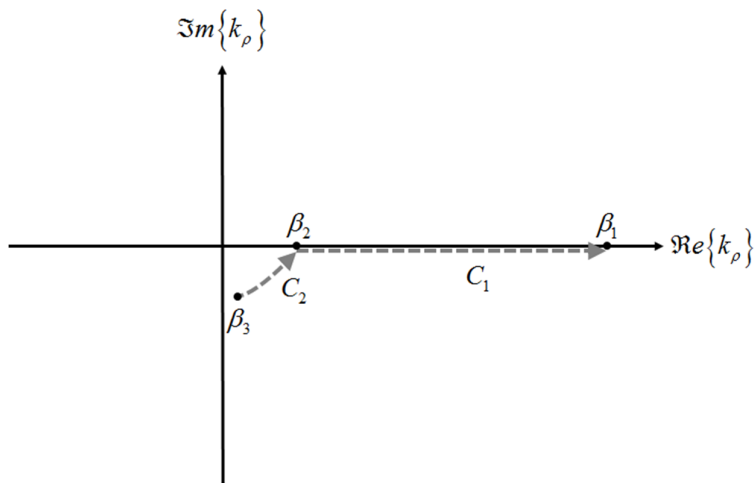

Figure 2.18: Sampling path across the k_ρ - plane using the two-level DCIM.

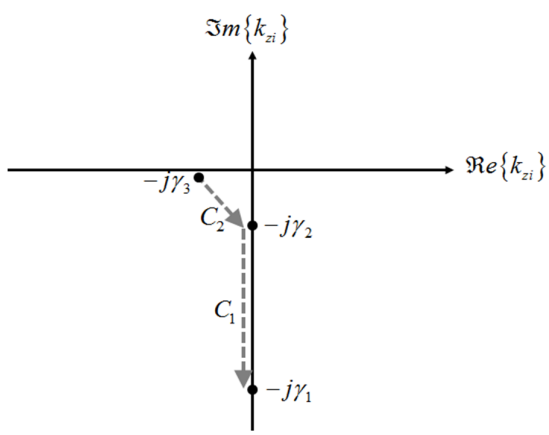

Figure 2.19: Sampling path across the k_{zi} - plane using the two-level DCIM

After sampling the function $f(t)$ with uniform steps along t, the GPOF method is applied where it calculates the coefficients and exponents of the exponentials defined in Equation (2.129). In terms of k_{zi}, the function along path C_1, can be represented as follows:

$$f_1(t)=\sum_{n=1}^{N_1} w_{1n} e^{\alpha_{1n} t} = \sum_{n=1}^{N_1} w_{1n} e^{\alpha_{1n}\frac{\gamma_2}{\gamma_2-\gamma_1}} e^{-\alpha_{1n}\frac{jk_{zi}}{\gamma_2-\gamma_1}} = f_1\left(k_{zi}\right) \tag{2.136}$$

Now, the low spectral values are not considered along path C_1 and the approximation of the function along this path does not provide an accurate approximation for the low spectrum. Thus, the differences between the exact function $f(t)$ and $f_1(t)$ must be sampled along C_2 with uniform steps of t. Doing so, the following equation is obtained after applying the GPOF technique:

$$f_2(t)=f(t)-f_1(t)=\sum_{n=1}^{N_2} w_{2n} e^{\alpha_{2n} t} = \sum_{n=1}^{N_2} w_{2n} e^{\alpha_{2n}\frac{\gamma_3}{\gamma_3-\gamma_2}} e^{-\alpha_{2n}\frac{jk_{zi}}{\gamma_3-\gamma_2}} = f_2\left(k_{zi}\right) \tag{2.137}$$

Consequently, each of the spectral domain Green's functions along the entire spectrum can be finally expressed as:

$$f(k_{zi})=f_1(k_{zi})+f_2(k_{zi})=\sum_{n=1}^{N_1} w_{1n} e^{\alpha_{1n}\frac{\gamma_2}{\gamma_2-\gamma_1}} e^{-\alpha_{1n}\frac{jk_{zi}}{\gamma_2-\gamma_1}} + \sum_{n=1}^{N_2} w_{2n} e^{\alpha_{2n}\frac{\gamma_3}{\gamma_3-\gamma_2}} e^{-\alpha_{2n}\frac{jk_{zi}}{\gamma_3-\gamma_2}} \tag{2.138}$$

It is important to note that the DCIM process is going to be performed on the spectral domain Green's functions without including the terms $e^{\pm jk_{zi}(z+z_1)}/k_{zi}$ and $e^{\pm jk_{zi}|z-z_1|}/k_{zi}$. In other words, the coefficients of the exponentials will only be subjected to the DCIM. The reason for that is to keep the DCIM outcome independent on the spatial distances between the test and source locations. Now, after the two-level DCIM is applied on the spectral Green's functions as specified, and the omitted terms are put back, any spectral Green's function can take either one of the following forms:

$$\tilde{G}\left(k_{zi},z\right)=\begin{cases} \sum_{n=1}^{N_1} w_{1n} e^{\alpha_{1n}\frac{\gamma_2}{\gamma_2-\gamma_1}} \dfrac{e^{-jk_{zi}\left(z+z_1+\frac{\alpha_{1n}}{\gamma_2-\gamma_1}\right)}}{k_{zi}} + \sum_{n=1}^{N_2} w_{2n} e^{\alpha_{2n}\frac{\gamma_3}{\gamma_3-\gamma_2}} \dfrac{e^{-jk_{zi}\left(z+z_1+\frac{\alpha_{2n}}{\gamma_3-\gamma_2}\right)}}{k_{zi}} \\ \sum_{n=1}^{N_1} w_{1n} e^{\alpha_{1n}\frac{\gamma_2}{\gamma_2-\gamma_1}} \dfrac{e^{-jk_{zi}\left(|z-z_1|+\frac{\alpha_{1n}}{\gamma_2-\gamma_1}\right)}}{k_{zi}} + \sum_{n=1}^{N_2} w_{2n} e^{\alpha_{2n}\frac{\gamma_3}{\gamma_3-\gamma_2}} \dfrac{e^{-jk_{zi}\left(|z-z_1|+\frac{\alpha_{2n}}{\gamma_3-\gamma_2}\right)}}{k_{zi}} \\ \sum_{n=1}^{N_1} w_{1n} e^{\alpha_{1n}\frac{\gamma_2}{\gamma_2-\gamma_1}} \dfrac{e^{jk_{zi}\left(-(z+z_1)+\frac{\alpha_{1n}}{\gamma_2-\gamma_1}\right)}}{k_{zi}} + \sum_{n=1}^{N_2} w_{2n} e^{\alpha_{2n}\frac{\gamma_3}{\gamma_3-\gamma_2}} \dfrac{e^{-jk_{zi}\left(-(z+z_1)+\frac{\alpha_{2n}}{\gamma_3-\gamma_2}\right)}}{k_{zi}} \\ \sum_{n=1}^{N_1} w_{1n} e^{\alpha_{1n}\frac{\gamma_2}{\gamma_2-\gamma_1}} \dfrac{e^{jk_{zi}\left(-|z-z_1|+\frac{\alpha_{1n}}{\gamma_2-\gamma_1}\right)}}{k_{zi}} + \sum_{n=1}^{N_2} w_{2n} e^{\alpha_{2n}\frac{\gamma_3}{\gamma_3-\gamma_2}} \dfrac{e^{-jk_{zi}\left(-|z-z_1|+\frac{\alpha_{2n}}{\gamma_3-\gamma_2}\right)}}{k_{zi}} \end{cases} \tag{2.139}$$

Applying Sommerfeld's identity in equation (2.127) on the spectral Green's function in equation (2.139) and using the identity of equation (2.140), the spatial domain Green's function can be expressed as follows:

$$
G(x,z)=\begin{cases}
\sum_{n=1}^{N_1} w_{1n} e^{\alpha_{1n}\frac{\gamma_2}{\gamma_2-\gamma_1}} K_0\left(\gamma\sqrt{(x-x')^2+\left(z+z'+\frac{\alpha_{1n}}{\gamma_2-\gamma_1}\right)^2}\right) \\
+\sum_{n=1}^{N_2} w_{2n} e^{\alpha_{2n}\frac{\gamma_3}{\gamma_3-\gamma_2}} K_0\left(\gamma\sqrt{(x-x')^2+\left(z+z'+\frac{\alpha_{2n}}{\gamma_3-\gamma_2}\right)^2}\right) \\
\\
\sum_{n=1}^{N_1} w_{1n} e^{\alpha_{1n}\frac{\gamma_2}{\gamma_2-\gamma_1}} K_0\left(\gamma\sqrt{(x-x')^2+\left(|z-z'|+\frac{\alpha_{1n}}{\gamma_2-\gamma_1}\right)^2}\right) \\
+\sum_{n=1}^{N_2} w_{2n} e^{\alpha_{2n}\frac{\gamma_3}{\gamma_3-\gamma_2}} K_0\left(\gamma\sqrt{(x-x')^2+\left(|z-z'|+\frac{\alpha_{2n}}{\gamma_3-\gamma_2}\right)^2}\right) \\
\\
\sum_{n=1}^{N_1} w_{1n} e^{\alpha_{1n}\frac{\gamma_2}{\gamma_2-\gamma_1}} K_0\left(\gamma\sqrt{(x-x')^2+\left(-(z+z')+\frac{\alpha_{1n}}{\gamma_2-\gamma_1}\right)^2}\right) \\
+\sum_{n=1}^{N_2} w_{2n} e^{\alpha_{2n}\frac{\gamma_3}{\gamma_3-\gamma_2}} K_0\left(\gamma\sqrt{(x-x')^2+\left(-(z+z')+\frac{\alpha_{2n}}{\gamma_3-\gamma_2}\right)^2}\right) \\
\\
\sum_{n=1}^{N_1} w_{1n} e^{\alpha_{1n}\frac{\gamma_2}{\gamma_2-\gamma_1}} K_0\left(\gamma\sqrt{(x-x')^2+\left(-|z-z'|+\frac{\alpha_{1n}}{\gamma_2-\gamma_1}\right)^2}\right) \\
+\sum_{n=1}^{N_2} w_{2n} e^{\alpha_{2n}\frac{\gamma_3}{\gamma_3-\gamma_2}} K_0\left(\gamma\sqrt{(x-x')^2+\left(-|z-z'|+\frac{\alpha_{2n}}{\gamma_3-\gamma_2}\right)^2}\right)
\end{cases} \tag{2.140}
$$

In Figure 2.20, the exact and approximated coefficients for the spectral domain Green's functions $\tilde{G}^{E_\ell,J_\ell}$ are compared. The problem studied is for a source located at the interface of two half-spaces (free-space/SiO_2). The parameters used for this problem are: $\beta_1 = 50\,k_0$, $\beta_2 = 5\,k_0$, and $\beta_3 = k_y = 8.23\times10^6 - 3.14\times10^5\,j$. The sampling parameters for k_{z1} along the first and second path are fixed to be $N_{p1} = N_{p2} = 100$. After applying the DCIM method to the basic spectral domain Green's function g^{E_ℓ,J_ℓ} , the following parameters are obtained:

n	w_{1n}	α_{1n}	w_{2n}	α_{2n}
1	–1.7650e+006	–42.9898	–2.1460e+006 –7.2744e+005 j	–18.4536 – 1.4954 j
2	–4.4801e+006	–18.1319	–1.1553e+006 +1.4590e+006 j	–5.4142 + 3.3026 j
3	–2.6341e+006	–6.8639	–2.7853e+007 –6.9556e+006 j	–7.8802 – 0.4295 j
4	–4.9940e+005	–1.7754	3.6964e+005 –1.1387e+006 j	–5.4093 – 4.2803 j

A comparison between the real and imaginary parts of the exact Green's function, $\tilde{G}^{E_\ell,J_\ell}$, and its approximated function using the DCIM method is shown in Figure 2.20. As shown the approximated function is coinciding with the exact function, indicating very high accuracy of fitting using exponential functions.

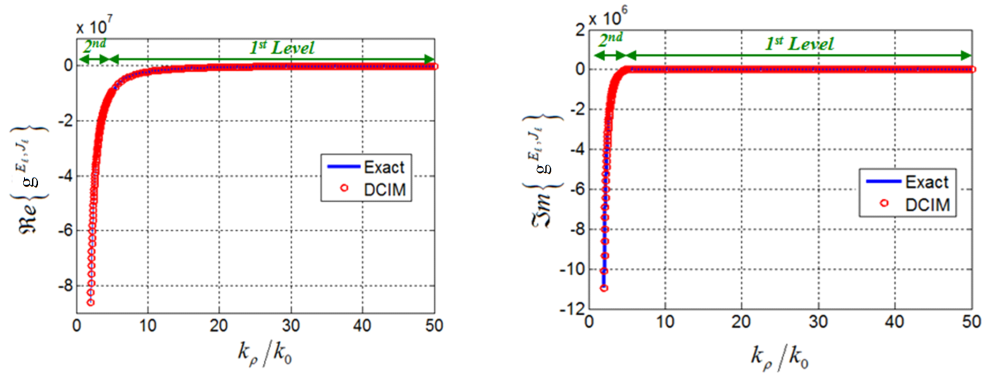

(a) (b)

Figure 2.20: Exact and DCIM approximation for the basic Green's function g^{E_ℓ,J_ℓ}: (a) real part, and (b) imaginary part.

After applying the DCIM technique for all the Green's functions, equation (2.140) is used to obtain the spatial domain Green's functions. These functions are dependent on three factors: the lateral distance between the test and source points: $(x-x')$, the vertical locations of the test and source points: $(z \pm z')$, and the propagation constant: k_y. Figures (2.21) – (2.25) show the various spectral domain Green's functions at 193.55 THz, propagation constant $k_y = 8.23\times10^6 - j\,3.14\times10^5$, and assuming the source point is located at $z'=0$. As shown from the figures, as the lateral or vertical distance between the sources and test points increases, the values of the Green's functions decreases. This means that when the test point is far from the source, it is less affected by the current flowing at the source point, which is expected.

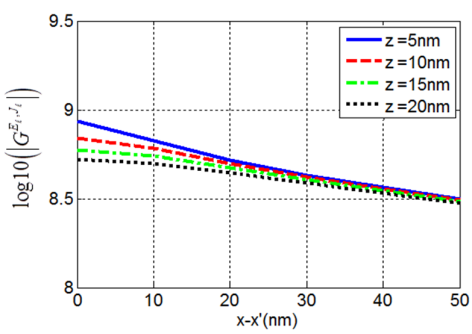

Figure 2.21: Spatial domain Green's function G^{E_ℓ,J_ℓ} versus the lateral distance between the source and test points $(x-x')$ at 193.55 THz, k_y = $8.23\times10^6 - j\,3.14\times10^5$ and $z'=0$.

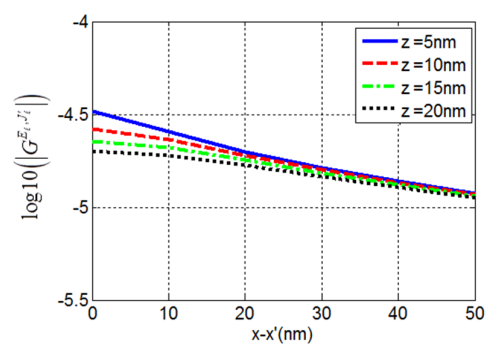

Figure 2.22: Spatial domain Green's function G^{E_ℓ,J'_ℓ} versus the lateral distance between the source and test points $(x-x')$ at 193.55 THz, k_y = $8.23\times10^6 - j\,3.14\times10^5$ and $z'=0$.

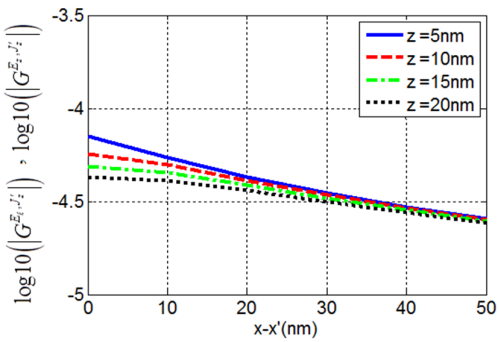

Figure 2.23: Spatial domain Green's functions $G^{E_\ell,J'_z}, G^{E_z,J'_z}$ versus the lateral distance between the source and test points $(x-x')$ at 193.55 THz, k_y = $8.23\times10^6 - j\,3.14\times10^5$ and $z' = 0$.

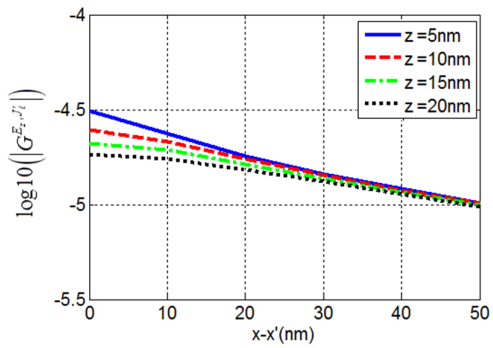

Figure 2.24: Spatial domain Green's function G^{E_z,J'_ℓ} versus the lateral distance between the source and test points $(x-x')$ at 193.55 THz, k_y = $8.23\times10^6 - j\,3.14\times10^5$ and $z' = 0$.

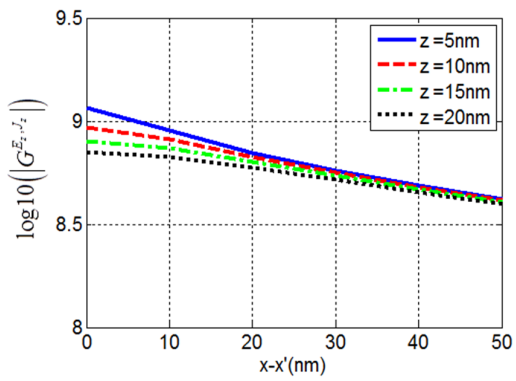

Figure 2.25: Spatial domain Green's function G^{E_z,J_z} versus the lateral distance between the source and test points $(x-x')$ at 193.55 THz, $k_y = 8.23\times10^6 - j\,3.14\times10^5$ and $z' = 0$.

2.8 Conclusions

This chapter presents the derivation of the spectral and spatial domain Green's functions. Starting from Maxwell's equations and applying the boundary conditions at each source/layer interface, the electric and magnetic fields expressions are obtained. The problem is first decomposed into two systems (TE and TM systems) for simplicity. After solving each system separately, a superposition for both solutions is performed in order to find the solution of the whole problem. In this work, we are concerned with electric current sources only. We are also interested in obtaining the electric field expressions without the magnetic fields. It has been shown in this chapter that the electric fields are related to the electric current densities through a Green's functions tensor, i.e. dyadic Green's functions. The expressions of these functions are dependent on the layer structure. Three main cases are considered in this work. First, we start by the source located in free-space where both the spectral and spatial domain Green's functions are known analytically. The second case

is regarding a source immersed within a layered medium. One example is a source located in half-space backed by a half-space. Another example is for a source located in a half-space on top of a finite thickness substrate backed with an infinite medium. The last example is for a source located inside a layer with finite thickness surrounded by two half-spaces. The chapter presents examples for the spectral domain Green's function as well as their spatial domain counterparts which are obtained using two-level DCIM technique.

Chapter 3: Formulation of the Method of Moments

This chapter presents the detailed formulation for the MoM technique which is used to calculate the propagation characteristics of plasmonic transmission lines. The formulation starts with the integral form of the spatial domain electric fields. In the previous chapter, the spatial domain Green's functions are derived from their spectral domain counterparts. These spatial domain Green's functions link the spatial domain electric fields with the spatial domain electric current densities. The MoM technique starts by meshing the plasmonic strips into smaller segments and assuming that each segment carries a unit current source with known basis function and unknown coefficient. The next step is to satisfy the boundary conditions along the plasmonic strips and apply a testing technique. After some analytical manipulations, the electric fields are expressed in matrix form where the only unknown(s) is (are) the propagation constant(s) of the propagating mode(s). The number of the propagating modes is dependent on the number of metallic strips constructing the transmission line as well as their dimensions. The value(s) of the propagation constant(s) can be obtained using an iterative numerical method which satisfies the matrix equation. After the propagation constant(s) is (are) calculated, the modal current(s) for all propagating mode(s) can be obtained accordingly.

3.1 Electric Field in terms of Electric Current

In chapter 2, the Green's functions in spatial domain are calculated using the DCIM method. These Green's functions provide a relation between the spatial domain electric fields and the spatial domain electric current densities. In integral form, equation (2.126) is expressed as:

$$\begin{aligned} E_{xi}(x,z) = & \int_{z'_j} dz' \int_{x'_j} dx' G_{ij}^{E_\ell,J_\ell}(x,z,x',z') J_{xj}(x',z') + \int_{z'_j} dz' \int_{x'_j} dx' \frac{\partial^2}{\partial x^2} G_{ij}^{E_\ell,J'_\ell}(x,z,x',z') J_{xj}(x',z') \\ & - jk_y \int_{z'_j} dz' \int_{x'_j} dx' \frac{\partial}{\partial x} G_{ij}^{E_\ell,J'_\ell}(x,z,x',z') J_{yj}(x',z') \\ & + \int_{z'_j} dz' \int_{x'_j} dx' \frac{\partial}{\partial x}\frac{\partial}{\partial z} G_{ij}^{E_\ell,J'_z}(x,z,x',z') J_{zj}(x',z') \end{aligned} \tag{3.1}$$

$$\begin{aligned} E_{yi}(x,z) = & -jk_y \int_{z'_j} dz' \int_{x'_j} dx' \frac{\partial}{\partial x} G_{ij}^{E_\ell,J'_\ell}(x,z,x',z') J_{xj}(x',z') \\ & + \int_{z'_j} dz' \int_{x'_j} dx' G_{ij}^{E_\ell,J_\ell}(x,z,x',z') J_{yj}(x',z') - k_y^2 \int_{z'_j} dz' \int_{x'_j} dx' G_{ij}^{E_\ell,J'_\ell}(x,z,x',z') J_{yj}(x',z') \\ & - jk_y \int_{z'_j} dz' \int_{x'_j} dx' \frac{\partial}{\partial z} G_{ij}^{E_\ell,J'_z}(x,z,x',z') J_{zj}(x',z') \end{aligned} \tag{3.2}$$

$$\begin{aligned} E_{zi}(x,z) = & \int_{z'_j} dz' \int_{x'_j} dx' \frac{\partial}{\partial z}\frac{\partial}{\partial x} G_{ij}^{E_z,J'_\ell}(x,z,x',z') J_{xj}(x',z') \\ & - jk_y \int_{z'_j} dz' \int_{x'_j} dx' \frac{\partial}{\partial z} G_{ij}^{E_z,J'_\ell}(x,z,x',z') J_{yj}(x',z') \\ & + \int_{z'_j} dz' \int_{x'_j} dx' \, G_{ij}^{E_z,J_z}(x,z,x',z') J_{zj}(x',z') + \int_{z'_j} dz' \int_{x'_j} dx' \, \frac{\partial^2}{\partial z^2} G_{ij}^{E_z,J'_z}(x,z,x',z') J_{zj}(x',z') \end{aligned} \tag{3.3}$$

where E_x, E_y and E_z are the *x*-, *y*-, and *z*- components of the spatial domain electric field, (x'_j, z'_j) is the domain of the current distribution in the *xz*-plane along the cross-section of the jth strip.

3.2 Electric Current Expansion

In the MoM technique, the metal strips comprising the plasmonic transmission line are discretized. In this work, rectangular segments with dimensions Δ_x along the *x*-axis, and Δ_z along the *z*-axis are used for discretization. The current along the metallic strip is modelled as a summation of pre-assumed basis functions weighted by unknown coefficients. The choice of the basis function is very essential in providing an accurate solution for the problem. The chosen representations for the electric current densities are given by:

$$J_x(x,z) = \sum_{n=1}^{N_x} A_n \; T(x-a_n) \; R(z-b_n) \tag{3.4}$$

$$J_y(x,z) = \sum_{n=1}^{N_y} B_n \; R\left(x - c_n\right) \; R(z - d_n) \tag{3.5}$$

$$J_z(x,z) = \sum_{n=1}^{N_z} C_n \; R\left(x - e_n\right) \; T(z - f_n) \tag{3.6}$$

where N_x, N_y, and N_z are the number of basis functions required to approximate the *x*-directed, *y*-directed, and *z*-directed current densities respectively. A_n, B_n, and C_n are the expansion coefficients (weights). $T(u)$, and $R(u)$ are triangular and rectangular functions, respectively, forming the current basis functions. $(a_n, b_n), (c_n, d_n)$, and (e_n, f_n) are the (x,z) centres of the *x*-directed, *y*-directed, and *z*-directed current basis functions, respectively, as shown in Figure 3.1.

It can be noticed from equations (3.4) – (3.6) that the longitudinal current J_y is represented by a rectangular prism basis function, while the transversal currents J_x and J_z are represented by triangular prism basis functions. The triangular functions defined in equations (3.4) and (3.6) can be an even triangular function, $ET(u)$, a right-sided triangular function, $RT(u)$, or a left-sided triangular function, $LT(u)$, as shown in Figure 3.2. The definitions of the triangular and rectangular functions are given by:

$$ET(u) = \begin{cases} \left(u + \Delta_u\right)/\Delta_u^2, & -\Delta_u < u < 0 \\ \left(\Delta_u - u\right)/\Delta_u^2, & 0 < u < \Delta_u \\ 0, & \text{otherwise} \end{cases} \tag{3.7}$$

$$RT(u) = \begin{cases} \left(\Delta_u - u\right)/\Delta_u^2, & 0 < u < \Delta_u \\ 0, & \text{otherwise} \end{cases} \tag{3.8}$$

$$LT(u) = \begin{cases} \left(u + \Delta_u\right)/\Delta_u^2, & -\Delta_u < u < 0 \\ 0, & \text{otherwise} \end{cases} \tag{3.9}$$

$$R(u) = \begin{cases} 1/\Delta_u, & -\left(\Delta_u/2\right) < u < \left(\Delta_u/2\right) \\ 0, & \text{otherwise} \end{cases} \tag{3.10}$$

It is worth noting that using $ET(u)$ function together with $R(u)$ function gives rise to a full "roof-top" basis function, while using either $RT(u)$ or $LT(u)$ together with $R(u)$ results in a "half roof-top" basis function. It is essential to highlight that the half roof-top basis functions are important to accurately describe J_x and J_z current densities at the edges of the strip. This is because the polarization current components represent parallel electric field components, which are intensive at the edges of the strip. Using full roof-top at the edges forces the transversal electric field to be zero, which is physically wrong. On the other hand, half roof-tops allow the transverse field to be non-zero at the edges leading to more accurate representation of the current/field distribution. Figure 3.1 shows that J_x at the left and right

edges of a metallic strip are represented by green arrows denoting half roof-top basis functions. Similarly, the J_z at the top and bottom edges of the strip are also represented by half roof-top basis function represented by the green arrows. On the other hand, full roof-tops indicated by blue arrows are used to express J_x and J_z elsewhere.

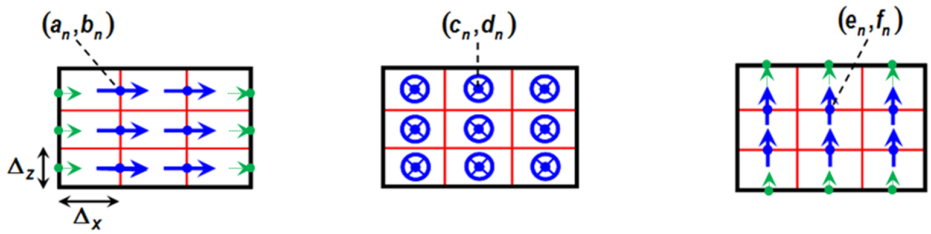

(a) (b) (c)

Figure 3.1: Basis functions used to expand the unknown modal current: (a) *x*-component, (b) *y*-component, and (c) *z*-component. Blue arrows of J_x and J_z denote full roof-top basis functions while green arrows represent half roof-tops basis functions.

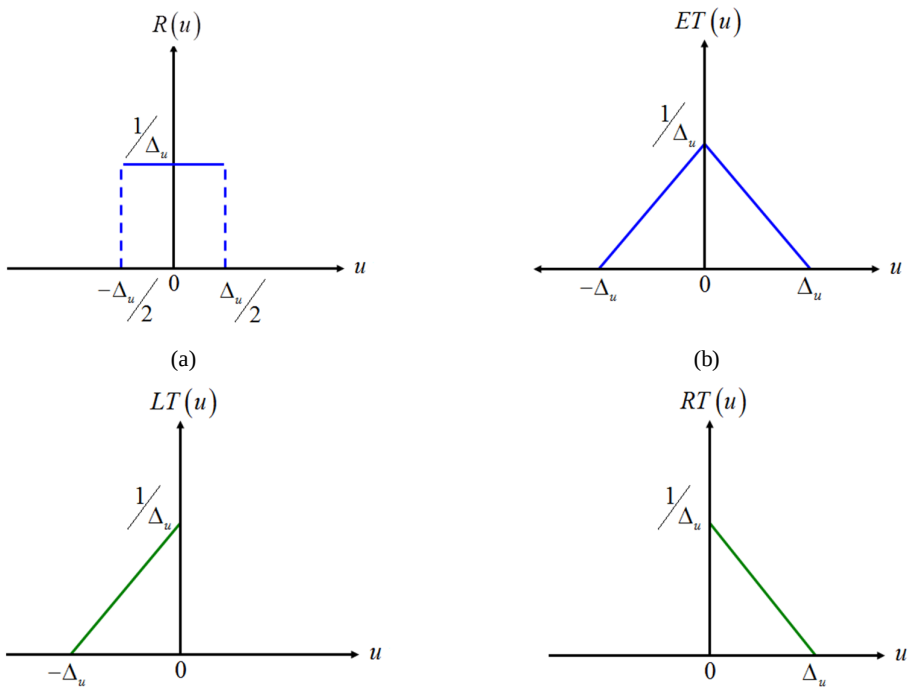

Figure 3.2: Functions used to represent the basis functions of the current density: (a) rectangular function, $R(u)$, (b) even triangular function, $ET(u)$, (c) left-sided triangular function, $LT(u)$, and (d) right-sided triangular function $RT(u)$.

3.3 Impedance Matrix Elements

At this stage, all needed spatial domain Green's functions are prepared. The next step is to insert these expressions in equations (3.1) – (3.3), and apply a suitable testing technique.

Two conventional testing techniques are used in the literature: The Galerkin testing or the razor-blade testing [84]. For the Galerkin technique, the testing current source is assumed to be exactly like the basis function. On the other hand, for the razor-blade testing, rectangular prisms are used to represent the testing current (i.e. $J_{test}(x,z) = R(x - x_m)R(z - z_m)$, where x_m, and z_m are the *x*- and *z*- locations of the current test functions respectively). The razor-blade testing technique is adopted in this work, due to its simplicity compared to the Galerkin testing, especially that the transversal current basis functions have various expressions depending on the location of the segment. Applying the razor-blade testing, the integrally tested electric field components can be expressed in a matrix form as follows:

$$\begin{bmatrix} [E_x] \\ [E_y] \\ [E_z] \end{bmatrix} = \begin{bmatrix} [Z_{xx1}]+[Z_{xx2}] & [Z_{xy}] & [Z_{xz}] \\ [Z_{yx}] & [Z_{yy1}]+[Z_{yy2}] & [Z_{yz}] \\ [Z_{zx}] & [Z_{zy}] & [Z_{zz1}]+[Z_{zz2}] \end{bmatrix} \begin{bmatrix} [A] \\ [B] \\ [C] \end{bmatrix} \tag{3.11}$$

where $[Z_{xx1}]$, $[Z_{xx2}]$, $[Z_{xy}]$, $[Z_{xz}]$, $[Z_{yx}]$, $[Z_{yy1}]$, $[Z_{yy2}]$, $[Z_{yz}]$, $[Z_{zx}]$, $[Z_{zy}]$, $[Z_{zz1}]$, and $[Z_{zz2}]$ are the impedance sub-matrices. The sub-matrices $[A]$, $[B]$, and $[C]$ represent the weights of the modal currents $[J_x]$, $[J_y]$, and $[J_z]$ respectively. The full expressions for the element (m,n) in these matrices are obtained after doing some mathematical work and interchanging the location of the differentiation. The impedance matrix elements are expressed as:

$$Z_{xx1}(m,n) = \frac{-j\omega\mu_0}{2\pi} \int_{z_-}^{z_+} dz \int_{x_-}^{x_+} dx R(x - a_m) R(z - b_m) \int_{z'_-}^{z'_+} dz' \int_{x'_-}^{x'_+} dx' G\begin{pmatrix} x, x' \\ z, z' \end{pmatrix} T(x' - a_n) R(z' - b_n) \tag{3.12}$$

$$\begin{aligned}
Z_{xx2}(m,n) &= \frac{-j}{2\pi\omega\varepsilon_1} \int_{z_-}^{z_+} dz \int_{x_-}^{x_+} dx R(x - a_m) R(z - b_m) \int_{z'_-}^{z'_+} dz' \int_{x'_-}^{x'_+} dx' \frac{\partial^2 G\begin{pmatrix} x, x' \\ z, z' \end{pmatrix}}{\partial x^2} T(x' - a_n) R(z' - b_n) \\
&= \frac{-j}{2\pi\omega\varepsilon_1} \int_{z_-}^{z_+} dz \int_{x_-}^{x_+} dx \frac{-\partial R(x - a_m)}{\partial x} R(z - b_m) \int_{z'_-}^{z'_+} dz' \int_{x'_-}^{x'_+} dx' G\begin{pmatrix} x, x' \\ z, z' \end{pmatrix} \frac{\partial T(x' - a_n)}{\partial x'} R(z' - b_n) \\
&= \frac{j}{2\pi\omega\varepsilon_1} \int_{z_-}^{z_+} dz \int_{x_-}^{x_+} dx \frac{\delta(x - x_-) - \delta(x - x_+)}{\Delta_x} R(z - b_m) \\
&\qquad * \int_{z'_-}^{z'_+} dz' \int_{x'_-}^{x'_+} dx' \, G\begin{pmatrix} x, x' \\ z, z' \end{pmatrix} \left(T'(x' - a_n) + sign * \frac{\delta(x' - a_n)}{\Delta_x} \right) R(z' - b_n) \\
&= \frac{j}{2\pi\omega\varepsilon_1\Delta_x} \int_{z_-}^{z_+} dz \int_{z'_-}^{z'_+} dz' \int_{x'_-}^{x'_+} dx' \left(G\begin{pmatrix} x, x' \\ z, z' \end{pmatrix}\Bigg|_{x=x_-} - G\begin{pmatrix} x, x' \\ z, z' \end{pmatrix}\Bigg|_{x=x_+} \right) R(z - b_m) T'(x' - a_n) R(z' - b_n) \\
&\quad - j\frac{sign}{2\pi\omega\varepsilon_1\Delta_x^2} \int_{z_-}^{z_+} dz \int_{z'_-}^{z'_+} dz' \left(G\begin{pmatrix} x, x' \\ z, z' \end{pmatrix}\Bigg|_{\substack{x=x_-, \\ x'=a_n}} - G\begin{pmatrix} x, x' \\ z, z' \end{pmatrix}_{\substack{x=x_+, \\ x'=a_n}} \right) R(z - b_m) R(z' - b_n)
\end{aligned} \tag{3.13}$$

$$
\begin{aligned}
Z_{xy}(m,n) &= \frac{k_y}{2\pi\omega\varepsilon_1}\int_{z_-}^{z_+} dz \int_{x_-}^{x_+} dx R(x-a_m)R(z-b_m)\int_{z'_-}^{z'_+} dz' \int_{x'_-}^{x'_+} dx' \frac{\partial G\begin{pmatrix} x,x' \\ z,z' \end{pmatrix}}{\partial x} R(x'-c_n)R(z'-d_n) \\
&= \frac{-k_y}{2\pi\omega\varepsilon_1}\int_{z_-}^{z_+} dz \int_{x_-}^{x_+} dx (-1)\frac{\partial R(x-a_m)}{\partial x} R(z-b_m)\int_{z'_-}^{z'_+} dz' \int_{x'_-}^{x'_+} dx'\, G\begin{pmatrix} x,x' \\ z,z' \end{pmatrix} R(x'-c_n)R(z'-d_n) \\
&= \frac{k_y}{2\pi\omega\varepsilon_1}\int_{z_-}^{z_+} dz\, R(z-b_m)\int_{x_-}^{x_+} dx \frac{\delta(x-x_-)-\delta(x-x_+)}{\Delta_x}\int_{z'_-}^{z'_+} dz' \int_{x'_-}^{x'_+} dx'\, G\begin{pmatrix} x,x' \\ z,z' \end{pmatrix} R(x'-c_n)R(z'-d_n) \\
&= \frac{k_y}{2\pi\omega\varepsilon_1}\frac{1}{\Delta_x}\int_{z_-}^{z_+} dz \int_{z'_-}^{z'_+} dz' \int_{x'_-}^{x'_+} dx' \left(G\begin{pmatrix} x,x' \\ z,z' \end{pmatrix}\Bigg|_{x=x_-} - G\begin{pmatrix} x,x' \\ z,z' \end{pmatrix}\Bigg|_{x=x_+} \right) R(z-b_m)R(x'-c_n)R(z'-d_n)
\end{aligned}
\tag{3.14}
$$

$$
\begin{aligned}
Z_{xz}(m,n) &= \frac{-j}{2\pi\omega\varepsilon_1}\int_{z_-}^{z_+} dz \int_{x_-}^{x_+} dx\, R(x-a_m)R(z-b_m)\int_{z'_-}^{z'_+} dz' \int_{x'_-}^{x'_+} dx' \frac{\partial^2 G\begin{pmatrix} x,x' \\ z,z' \end{pmatrix}}{\partial x \partial z} R(x'-e_n)T(z'-f_n) \\
&= \frac{-j}{2\pi\omega\varepsilon_1}\int_{z_-}^{z_+} dz \int_{x_-}^{x_+} dx \frac{-\partial R(x-a_m)}{\partial x}\frac{-\partial R(z-b_m)}{\partial z}\int_{z'_-}^{z'_+} dz' \int_{x'_-}^{x'_+} dx' G\begin{pmatrix} x,x' \\ z,z' \end{pmatrix} R(x'-e_n)T(z'-f_n) \\
&= \frac{-j}{2\pi\omega\varepsilon_1}\int_{z_-}^{z_+} dz \int_{x_-}^{x_+} dx \frac{\delta(x-x_-)-\delta(x-x_+)}{\Delta_x} * \frac{\delta(z-z_-)-\delta(z-z_+)}{\Delta_z} \\
&\qquad * \int_{z'_-}^{z'_+} dz' \int_{x'_-}^{x'_+} dx' G\begin{pmatrix} x,x' \\ z,z' \end{pmatrix} R(x'-e_n)T(z'-f_n) \\
&= \frac{-j}{2\pi\omega\varepsilon_1\Delta_x\Delta_z}\int_{z'_-}^{z'_+} dz' \int_{x'_-}^{x'_+} dx' \left(G\begin{pmatrix} x,x' \\ z,z' \end{pmatrix}\Bigg|_{\substack{x=x_-,\\ z=z_-}} - G\begin{pmatrix} x,x' \\ z,z' \end{pmatrix}\Bigg|_{\substack{x=x_+,\\ z=z_-}} - G\begin{pmatrix} x,x' \\ z,z' \end{pmatrix}\Bigg|_{\substack{x=x_-,\\ z=z_+}} + G\begin{pmatrix} x,x' \\ z,z' \end{pmatrix}\Bigg|_{\substack{x=x_+,\\ z=z_+}} \right) \\
&\qquad * R(x'-e_n)T(z'-f_n)
\end{aligned}
\tag{3.15}
$$

$$
\begin{aligned}
Z_{yx}(m,n) &= \frac{-k_y}{2\pi\omega\varepsilon_1}\int_{z_-}^{z_+} dz \int_{x_-}^{x_+} dx R(x-c_m)R(z-d_m)\int_{z'_-}^{z'_+} dz' \int_{x'_-}^{x'_+} dx' \frac{\partial G\begin{pmatrix} x,x' \\ z,z' \end{pmatrix}}{\partial x} T(x'-a_n)R(z'-b_n) \\
&= \frac{-k_y}{2\pi\omega\varepsilon_1}\int_{z_-}^{z_+} dz \int_{x_-}^{x_+} dx \frac{-\partial R(x-c_m)}{\partial x} R(z-d_m)\int_{z'_-}^{z'_+} dz' \int_{x'_-}^{x'_+} dx'\, G\begin{pmatrix} x,x' \\ z,z' \end{pmatrix} T(x'-a_n)R(z'-b_n) \\
&= \frac{k_y}{2\pi\omega\varepsilon_1}\int_{z_-}^{z_+} dz \int_{x_-}^{x_+} dx \frac{\delta(x-x_-)-\delta(x-x_+)}{\Delta_x} R(z-d_m)\int_{z'_-}^{z'_+} dz' \int_{x'_-}^{x'_+} dx'\, G\begin{pmatrix} x,x' \\ z,z' \end{pmatrix} T(x'-a_n)R(z'-b_n) \\
&= \frac{k_y}{2\pi\omega\varepsilon_1\Delta_x}\int_{z_-}^{z_+} dz \int_{z'_-}^{z'_+} dz' \int_{x'_-}^{x'_+} dx' \left(G\begin{pmatrix} x,x' \\ z,z' \end{pmatrix}\Bigg|_{x=x_-} - G\begin{pmatrix} x,x' \\ z,z' \end{pmatrix}\Bigg|_{x=x_+} \right) R(z-d_m)T(x'-a_n)R(z'-b_n)
\end{aligned}
\tag{3.16}
$$

$$
Z_{yy1}(m,n) = \frac{-j\omega\mu_0}{2\pi}\int_{z_-}^{z_+} dz \int_{x_-}^{x_+} dx\, R(z-d_n)R(x-c_n)\int_{z'_-}^{z'_+} dz \int_{x'_-}^{x'_+} dx\, G\begin{pmatrix} x,x' \\ z,z' \end{pmatrix} R(z-d_m)R(x-c_m) \tag{3.17}
$$

$$Z_{yy2}(m,n)=\frac{jk_y^2}{2\pi\omega\varepsilon_1}\int_{z_-}^{z_+}dz\int_{x_-}^{x_+}dx\,R(z-d_n)R(x-c_n)\int_{z'_-}^{z'_+}dz\int_{x'_-}^{x'_+}dx\,G\begin{pmatrix}x,x'\\z,z'\end{pmatrix}R(z-d_m)R(x-c_m) \tag{3.18}$$

$$\begin{aligned}
Z_{yz}(m,n)&=\frac{-k_y}{2\pi\omega\varepsilon_1}\int_{z_-}^{z_+}dz\int_{x_-}^{x_+}dx\,R(x-c_m)\,R(z-d_m)\int_{z'_-}^{z'_+}dz'\int_{x'_-}^{x'_+}dx'\,\frac{\partial G\begin{pmatrix}x,x'\\z,z'\end{pmatrix}}{\partial z}R(x'-e_n)\,T(z'-f_n)\\
&=\frac{-k_y}{2\pi\omega\varepsilon_1}\int_{z_-}^{z_+}dz\int_{x_-}^{x_+}dx\,R(x-c_m)\,\frac{-\partial R(z-d_m)}{\partial z}\int_{z'_-}^{z'_+}dz'\int_{x'_-}^{x'_+}dx'\,G\begin{pmatrix}x,x'\\z,z'\end{pmatrix}R(x'-e_n)\,T(z'-f_n)\\
&=\frac{k_y}{2\pi\omega\varepsilon_1}\int_{z_-}^{z_+}dz\int_{x_-}^{x_+}dx\,R(x-c_m)\,\frac{\delta(z-z_-)-\delta(z-z_+)}{\Delta_z}\int_{z'_-}^{z'_+}dz'\int_{x'_-}^{x'_+}dx'\,G\begin{pmatrix}x,x'\\z,z'\end{pmatrix}R(x'-e_n)T(z'-f_n)\\
&=\frac{k_y}{2\pi\omega\varepsilon_1\Delta_z}\int_{x_-}^{x_+}dx\int_{z'_-}^{z'_+}dz'\int_{x'_-}^{x'_+}dx'\left(G\begin{pmatrix}x,x'\\z,z'\end{pmatrix}\Bigg|_{z=z_-}-G\begin{pmatrix}x,x'\\z,z'\end{pmatrix}\Bigg|_{z=z_+}\right)R(x-c_m)R(x'-e_n)T(z'-f_n)
\end{aligned} \tag{3.19}$$

$$\begin{aligned}
Z_{zx}(m,n)&=\frac{-j}{2\pi\omega\varepsilon_1}\int_{z_-}^{z_+}dz\int_{x_-}^{x_+}dx\,R(x-e_m)R(z-f_m)\int_{z'_-}^{z'_+}dz'\int_{x'_-}^{x'_+}dx'\,\frac{\partial^2 G\begin{pmatrix}x,x'\\z,z'\end{pmatrix}}{\partial z\partial x}T(x'-a_n)R(z'-b_n)\\
&=\frac{-j}{2\pi\omega\varepsilon_1}\int_{z_-}^{z_+}dz\int_{x_-}^{x_+}dx\,\frac{-\partial R(x-e_m)}{\partial x}\frac{-\partial(z-f_m)}{\partial z}R\int_{z'_-}^{z'_+}dz'\int_{x'_-}^{x'_+}dx'G\begin{pmatrix}x,x'\\z,z'\end{pmatrix}T(x'-a_n)R(z'-b_n)\\
&=\frac{-j}{2\pi\omega\varepsilon_1}\int_{z'_-}^{z_+}dz\int_{x'_-}^{x_+}dx\,\frac{\delta(x-x_-)-\delta(x-x_+)}{\Delta_x}*\frac{\delta(z-z_-)-\delta(z-z_+)}{\Delta_z}\\
&\qquad *\int_{z'_-}^{z'_+}dz'\int_{x'_-}^{x'_+}dx'G\begin{pmatrix}x,x'\\z,z'\end{pmatrix}T(x'-a_n)R(z'-b_n)\\
&=\frac{-j}{2\pi\omega\varepsilon_1\Delta_x\Delta_z}\int_{z'_-}^{z'_+}dz'\int_{x'_-}^{x'_+}dx'\left(G\begin{pmatrix}x,x'\\z,z'\end{pmatrix}\Bigg|_{\substack{x=x_-\\z=z_-}}-G\begin{pmatrix}x,x'\\z,z'\end{pmatrix}\Bigg|_{\substack{x=x_+\\z=z_-}}-G\begin{pmatrix}x,x'\\z,z'\end{pmatrix}\Bigg|_{\substack{x=x_-\\z=z_+}}+G\begin{pmatrix}x,x'\\z,z'\end{pmatrix}\Bigg|_{\substack{x=x_+\\z=z_+}}\right)\\
&\qquad *T(x'-a_n)R(z'-b_n)
\end{aligned} \tag{3.20}$$

$$\begin{aligned}
Z_{zy}(m,n)&=\frac{-k_y}{2\pi\omega\varepsilon_1}\int_{z_-}^{z_+}dz\int_{x_-}^{x_+}dxR(x-e_m)R(z-f_m)\int_{z'_-}^{z'_+}dz'\int_{x'_-}^{x'_+}dx'\,\frac{\partial G\begin{pmatrix}x,x'\\z,z'\end{pmatrix}}{\partial z}R(x'-c_n)R(z'-d_n)\\
&=\frac{-k_y}{2\pi\omega\varepsilon_1}\int_{z_-}^{z_+}dz\int_{x_-}^{x_+}dxR(x-e_m)\frac{-\partial R(z-f_m)}{\partial z}\int_{z'_-}^{z'_+}dz'\int_{x'_-}^{x'_+}dx'\,G\begin{pmatrix}x,x'\\z,z'\end{pmatrix}R(x'-c_n)R(z'-d_n)\\
&=\frac{-k_y}{2\pi\omega\varepsilon_1}\int_{x_-}^{x_+}dx\int_{z_-}^{z_+}dz\,\frac{\delta(z-z_-)-\delta(z-z_+)}{\Delta_z}R(x-e_m)\int_{z'^-}^{z'_+}dz'\int_{x'^-}^{x'_+}dx'\,G\begin{pmatrix}x,x'\\z,z'\end{pmatrix}R(x'-c_n)R(z'-d_n)\\
&=\frac{-k_y}{2\pi\omega\varepsilon_1\Delta_z}\int_{x_-}^{x_+}dx\int_{z'_-}^{z'_+}dz'\int_{x'_-}^{x'_+}dx'\left(G\begin{pmatrix}x,x'\\z,z'\end{pmatrix}\Bigg|_{z=z_-}-G\begin{pmatrix}x,x'\\z,z'\end{pmatrix}\Bigg|_{z=z_+}\right)R(x-e_m)R(x'-c_n)R(z'-d_n)
\end{aligned} \tag{3.21}$$

$$Z_{zz1}(m,n)=\frac{-j\omega\mu_0}{2\pi}\int_{z_-}^{z_+}dz\int_{x_-}^{x_+}dx\,R(x-e_m)R(z-f_m)\int_{z'_-}^{z'_+}dz'\int_{x'_-}^{x'_+}dx'G\begin{pmatrix}x,x'\\z,z'\end{pmatrix}R(x'-e_n)T(z'-f_n) \tag{3.22}$$

$$\begin{aligned}
Z_{zz_2}(m,n)&=\frac{-j}{2\pi\omega\varepsilon_1}\int_{z_-}^{z_+}dz\int_{x_-}^{x_+}dx\,R(x-e_m)R(z-f_m)\int_{z'_-}^{z'_+}dz'\int_{x'_-}^{x'_+}dx'\,\frac{\partial^2 G\begin{pmatrix}x,x'\\z,z'\end{pmatrix}}{\partial z^2}R(x'-e_n)\,T(z'-f_n)\\
&=\frac{-j}{2\pi\omega\varepsilon_1}\int_{z_-}^{z_+}dz\int_{x_-}^{x_+}dx\,R(x-e_m)\frac{-\partial R(z-f_m)}{\partial z}\int_{z'_-}^{z'_+}dz'\int_{x'_-}^{x'_+}dx'(\mp 1)\frac{\partial G\begin{pmatrix}x,x'\\z,z'\end{pmatrix}}{\partial z'}R(x'-e_n)\,T(z'-f_n)\\
&=\frac{(\mp j)}{2\pi\omega\varepsilon_1}\int_{z_-}^{z_+}dz\int_{x_-}^{x_+}dx\,R(x-e_m)\frac{\partial R(z-f_m)}{\partial z}\int_{z'_-}^{z'_+}dz'\int_{x'_-}^{x'_+}dx'G\begin{pmatrix}x,x'\\z,z'\end{pmatrix}R(x'-e_n)\frac{-\partial T(z'-f_n)}{\partial z'}\\
&=\frac{\pm j}{2\pi\omega\varepsilon_1}\int_{z_-}^{z_+}dz\int_{x_-}^{x_+}dx\,\frac{\delta(z-z_-)-\delta(z-z_+)}{\Delta_z}R(x-e_m)\\
&\qquad *\int_{z'_-}^{z'_+}dz'\int_{x'_-}^{x'_+}dx'G\begin{pmatrix}x,x'\\z,z'\end{pmatrix}R(x'-e_n)\left(T'(z'-f_n)+sign*\frac{\delta(z'-f_n)}{\Delta_z}\right)\\
&=\frac{\pm j}{2\pi\omega\varepsilon_1\Delta_z}\int_{x_-}^{x_+}dx\int_{z'_-}^{z'_+}dz'\int_{x'_-}^{x'_+}dx'\left(G\begin{pmatrix}x,x'\\z,z'\end{pmatrix}\Bigg|_{z=z_-}-G\begin{pmatrix}x,x'\\z,z'\end{pmatrix}\Bigg|_{z=z_+}\right)R(x-e_m)R(x'-e_n)T'(z'-f_n)\\
&\pm j\frac{sign}{2\pi\omega\varepsilon_1\Delta_z^2}\int_{x_-}^{x_+}dx\int_{x'_-}^{x'_+}dx'\left(G\begin{pmatrix}x,x'\\z,z'\end{pmatrix}\Bigg|_{\substack{z=z_-\\z'=f_n}}-G\begin{pmatrix}x,x'\\z,z'\end{pmatrix}\Bigg|_{\substack{z=z_+\\z'=f_n}}\right)R(x-e_m)R(x'-e_n)
\end{aligned} \tag{3.23}$$

where m and n are the orders of the test and basis functions, respectively. $x_+(z_+)$ and $x_-(z_-)$ are the maximum and minimum, respectively, limits of the test function along the x-axis (z-axis), while $x'_+(z'_+)$ and $x'_-(z'_-)$ are the maximum and minimum, respectively, limits of the basis function along the x-axis (z-axis). It is worth noting that the integration in equations (3.13) – (3.23) can be simplified analytically where double integrations along the x and x' or z and z' can be reduced to one integration using an identity presented in [85].

As mentioned earlier, the triangular basis function can be an even triangle (*ET*), right-sided triangle (*RT*), or left-sided (*LT*) triangle. The choice between the three cases depends on the location of the current sources. For instance, the left (right) hand side basis functions of the J_x and the upper (bottom) hand side basis functions of the J_z are represented by right-hand (left-hand) side half roof-tops prisms. The rest of the basis functions of J_x and J_z are represented by full roof-top basis functions. The derivative of the triangular functions denoted by $ET'(u)$, $RT'(u)$, and $LT'(u)$, as well as the delta function $\delta(u)$, which appeared in equations (3.13) – (3.23) are defined as follows:

$$ET'(u) = \begin{cases} 1/\Delta_u^2, & -\Delta_u < u < 0 \\ -1/\Delta_u^2, & 0 < u < \Delta_u \\ 0, & \text{otherwise} \end{cases} \tag{3.24}$$

$$RT'(u) = \begin{cases} -1/\Delta_u^2, & 0 < u < \Delta_u \\ 0, & \text{otherwise} \end{cases} \tag{3.25}$$

$$LT'(u) = \begin{cases} 1/\Delta_u^2, & -\Delta_u < u < 0 \\ 0, & \text{otherwise} \end{cases} \tag{3.26}$$

$$\delta(u) = \begin{cases} 1/\Delta_u, & u = 0 \\ 0, & \text{otherwise} \end{cases} \tag{3.27}$$

It is worth noting that in equation (3.23) $\partial G(x, x', z, z')/\partial z$ is replaced by $\mp \partial G(x, x', z, z')/\partial z'$. The negative (positive) sign corresponds to the case when the spectral domain Green's function is proportional to $\frac{e^{\mp jk_{zi}|z-z'|}}{k_{zi}} \left(\frac{e^{\mp jk_{zi}(z+z')}}{k_{zi}} \right)$. The value of the variable "*sign*" is determined according to the type of its corresponding basis function as follows:

Function	$ET(u)$	$RT(u)$	$LT(u)$
sign	0	+1	–1

3.4 Boundary Conditions along the Metallic Strips

After meshing the metal strips and expanding the unknown currents along them, the next step is to satisfy the boundary conditions at these strips. Unlike the perfect conductors where current cannot flow inside their volumes, plasmonic materials allow current to flow inside them. The electric field inside any plasmonic strip is given by [86–87]:

$$E_{(x,y,z)i} = \frac{1}{j\omega\varepsilon_0(\hat{\varepsilon}_{ri} - \hat{\varepsilon}_{rb})} J_{(x,y,z)i} \tag{3.28}$$

where $\hat{\varepsilon}_{ri}$ and $\hat{\varepsilon}_{rb}$ are the relative dielectric constants of the ith plasmonic strip and the background material surrounding it, respectively. Substituting equations (3.4) – (3.6) into equations (3.1) – (3.3), then into equation (3.28) and applying razor-blade testing, the following matrix equation is obtained:

$$\begin{bmatrix} [E_x] \\ [E_y] \\ [E_z] \end{bmatrix} = \begin{bmatrix} [Z_{xx}] & [Z_{xy}] & [Z_{xz}] \\ [Z_{yx}] & [Z_{yy}] & [Z_{yz}] \\ [Z_{zx}] & [Z_{zy}] & [Z_{zz}] \end{bmatrix} \begin{bmatrix} [A] \\ [B] \\ [C] \end{bmatrix} = \begin{bmatrix} [Z'_{xx}] & [0] & [0] \\ [0] & [Z'_{yy}] & [0] \\ [0] & [0] & [Z'_{zz}] \end{bmatrix} \begin{bmatrix} [A] \\ [B] \\ [C] \end{bmatrix} \tag{3.29}$$

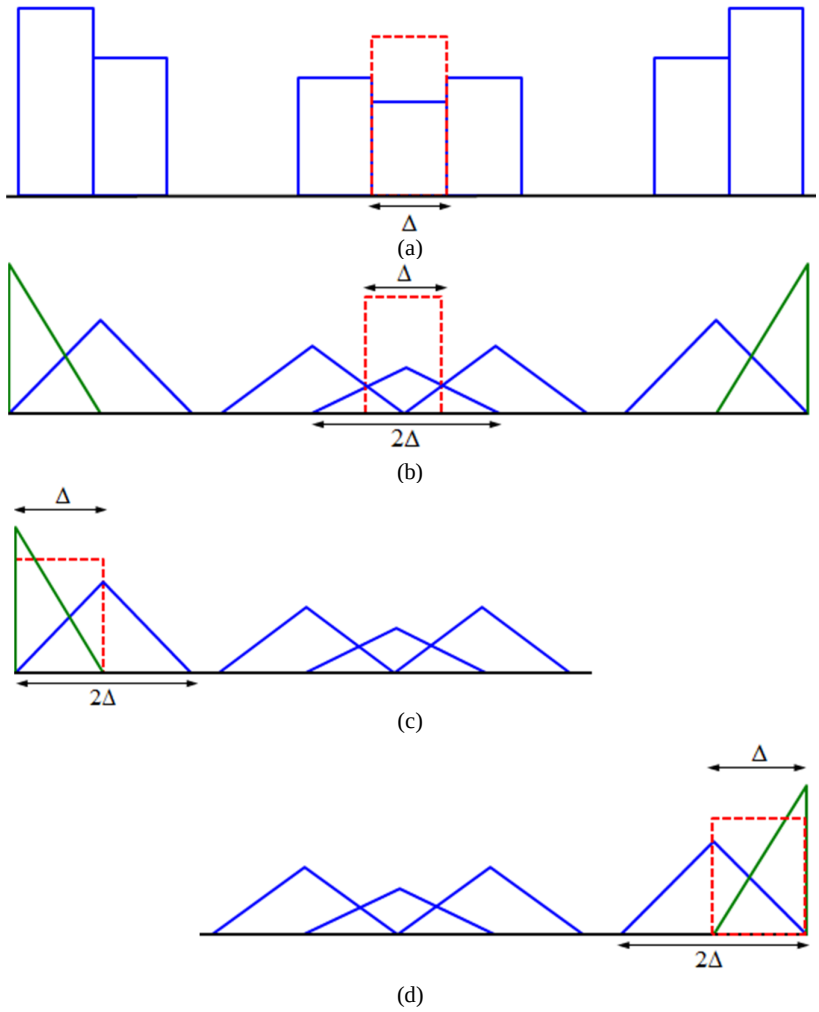

Figure 3.3: Overlap between the basis function (blue and green lines) and the test function (red dashed line) when the basis function is: (a) rectangular prism, (b) even triangular prism, (c) right-hand sided triangular prism, and (d) left-hand sided triangular prism.

where $[Z_{xx}]=[Z_{xx1}]+[Z_{xx2}]$, $[Z_{yy}]=[Z_{yy1}]+[Z_{yy2}]$, and $[Z_{zz}]=[Z_{zz1}]+[Z_{zz2}]$.The majority of elements in the matrices $[Z'_{xx}],[Z'_{yy}]$, and $[Z'_{zz}]$ are zero. The non-zero elements in these matrices are given by:

$$Z'_{xx}(m,n)=\frac{1}{j\omega\varepsilon_0\left(\hat{\varepsilon}_{ri}-\hat{\varepsilon}_{rb}\right)}\int_{z_-}^{z_+}dz\int_{x_-}^{x_+}dxR\left(x-a_m\right)R\left(z-b_m\right)T\left(x-a_n\right)R\left(z-b_n\right),\quad \left|m-n\right|\le 1 \tag{3.30}$$

$$Z'_{yy}(m,n)=\frac{1}{j\omega\varepsilon_0\left(\hat{\varepsilon}_{ri}-\hat{\varepsilon}_{rb}\right)}\int_{z_-}^{z_+}dz\int_{x_-}^{x_+}dxR\left(x-c_m\right)R\left(z-d_m\right)R\left(x-c_n\right)R\left(z-d_n\right),\quad m=n \tag{3.31}$$

$$Z'_{zz}(m,n)=\frac{1}{j\omega\varepsilon_0\left(\hat{\varepsilon}_{ri}-\hat{\varepsilon}_{rb}\right)}\int_{z_-}^{z_+}dz\int_{x_-}^{x_+}dx\,R\left(x-e_m\right)\,R\left(z-f_m\right)\,R\left(x-e_n\right)\,T\left(z-f_n\right),\quad \left|m-n\right|\le 1 \tag{3.32}$$

These non-zero values occur when the basis and test functions have overlapping domains. For $\left[Z'_{yy}\right]$, the basis and test functions overlap only if their centres coincide. Therefore, only the diagonal terms of $\left[Z'_{yy}\right]$ are non-zero. For $\left[Z'_{xx}\right]\left(\left[Z'_{zz}\right]\right)$, the basis and test functions overlap if their *x*-(*z*-) centres coincide or are shifted by a value of $\Delta_x\left(\Delta_z\right)$. This overlap is illustrated in Figure 3.3.

As shown in Figure 3.3(a), when the test and the basis functions are coinciding rectangular prisms, the whole domain overlap, while none of the neighbouring basis functions overlap with the test function. Therefore, the $\left[Z'_{yy}\right]$ matrix can be calculated analytically using equation (3.31) where is takes the following form:

$$\left[Z'_{yy}\right] = \frac{1}{j\omega\varepsilon_0\left(\hat{\varepsilon}_{ri} - \hat{\varepsilon}_{rb}\right)}\frac{1}{\Delta_x\Delta_z}\begin{bmatrix} 1 & 0 & \cdots & 0 & 0 \\ 0 & 1 & \cdots & 0 & 0 \\ \vdots & \vdots & \ddots & \vdots & \vdots \\ 0 & 0 & \cdots & 1 & 0 \\ 0 & 0 & \cdots & 0 & 1 \end{bmatrix} \tag{3.33}$$

On the other hand, for transversal currents, the basis functions are triangular prisms. The overlapping between the basis and test functions for these cases are shown in Figures 3.3(b) – 3.3(d). Clearly, the test function affects the basis function having the same centre and also its neighbouring basis function. For razor-blade testing, the test function is always a rectangular prism while the basis functions can be a full roof-top or a half roof-top. Therefore, the impedance matrix element can be one of five different cases, as illustrated in Figure 3.4. The first case when the basis function is a full roof-top and its centre coincides with the centre of the test function. The second case when the basis function is a half roof-top and its centre coincides with the test function. The third case when the basis function is a full roof-top but the test function is shifted from the basis function with a value of $\Delta_x\left(\Delta_z\right)$ for $J_x\left(J_z\right)$, respectively. The fourth case is when the basis function is a half roof-top and the test function is shifted from the basis function with a value $\Delta_x\left(\Delta_z\right)$ for $J_x\left(J_z\right)$, respectively. The last case occurs when the basis function and the test function do not overlap. For each case, the non-zero impedance matrix elements of Z'_{xx} or Z'_{zz} can be calculated analytically from equations (3.30), and (3.32), where they can be expressed as described in the following table:

Table 3.1: Different cases and the corresponding values of the impedance matrix elements: Z'_{xx} or Z'_{zz}

Case	$Z'_{xx}(m,n)$ or $Z'_{zz}(m,n)$
Case 1	$\frac{3/4}{j\omega\varepsilon_0(\hat{\varepsilon}_{ri}-\hat{\varepsilon}_{rb})\Delta_x\Delta_z}$
Case 2	$\frac{3/16}{j\omega\varepsilon_0(\hat{\varepsilon}_{ri}-\hat{\varepsilon}_{rb})\Delta_x\Delta_z}$
Case 3	$\frac{1/8}{j\omega\varepsilon_0(\hat{\varepsilon}_{ri}-\hat{\varepsilon}_{rb})\Delta_x\Delta_z}$
Case 4	$\frac{1/8}{j\omega\varepsilon_0(\hat{\varepsilon}_{ri}-\hat{\varepsilon}_{rb})\Delta_x\Delta_z}$
Case 5	0

In a compact form, equation (3.29) reduces to:

$$\left[[Z]-[Z']\right][W]=[0] \tag{3.34}$$

where $[Z]$ is the impedance matrix relating the electric fields to the electric current densities, $[Z']$ is the impedance matrix after satisfying the boundary conditions along the metallic strips, and $[W]$ is a vector that represents the weights of the modal current. The non-trivial solution of equation (3.34) implies that the determinant of the matrix $\left[[Z]-[Z']\right]$, should vanish. The dimension of this matrix is $M \times M$ where M represents the total number of the current basis functions (i.e. $M = N_x + N_y + N_z$). It is worth noting that each element of the matrix $\left[[Z]-[Z']\right]$ is k_y dependent. Hence, the "*characteristic equation*" can be written as follows:

$$\left|[Z]-[Z']\right| = f\left(k_y\right)=0 \tag{3.35}$$

The value of the complex propagation constant, k_y, can be obtained using iterative methods such as Müller's method [88] which is adopted in our solver. It is worth noting that plasmonic transmission lines can allow more than one propagating modes depending on the number of metallic strips constructing the transmission line in addition to the geometry of these strips. The last step is to obtain the mode profile of the propagating mode(s). This is achieved by substituting with the value of k_y in equation (3.34) and applying the Singular Value Decomposition (SVD) technique [89–90] to obtain the weights of all current components. This is performed for each value of k_y to obtain their corresponding modal current distribution. The electric field components at any location can then be obtained directly using equations (3.1) – (3.3).

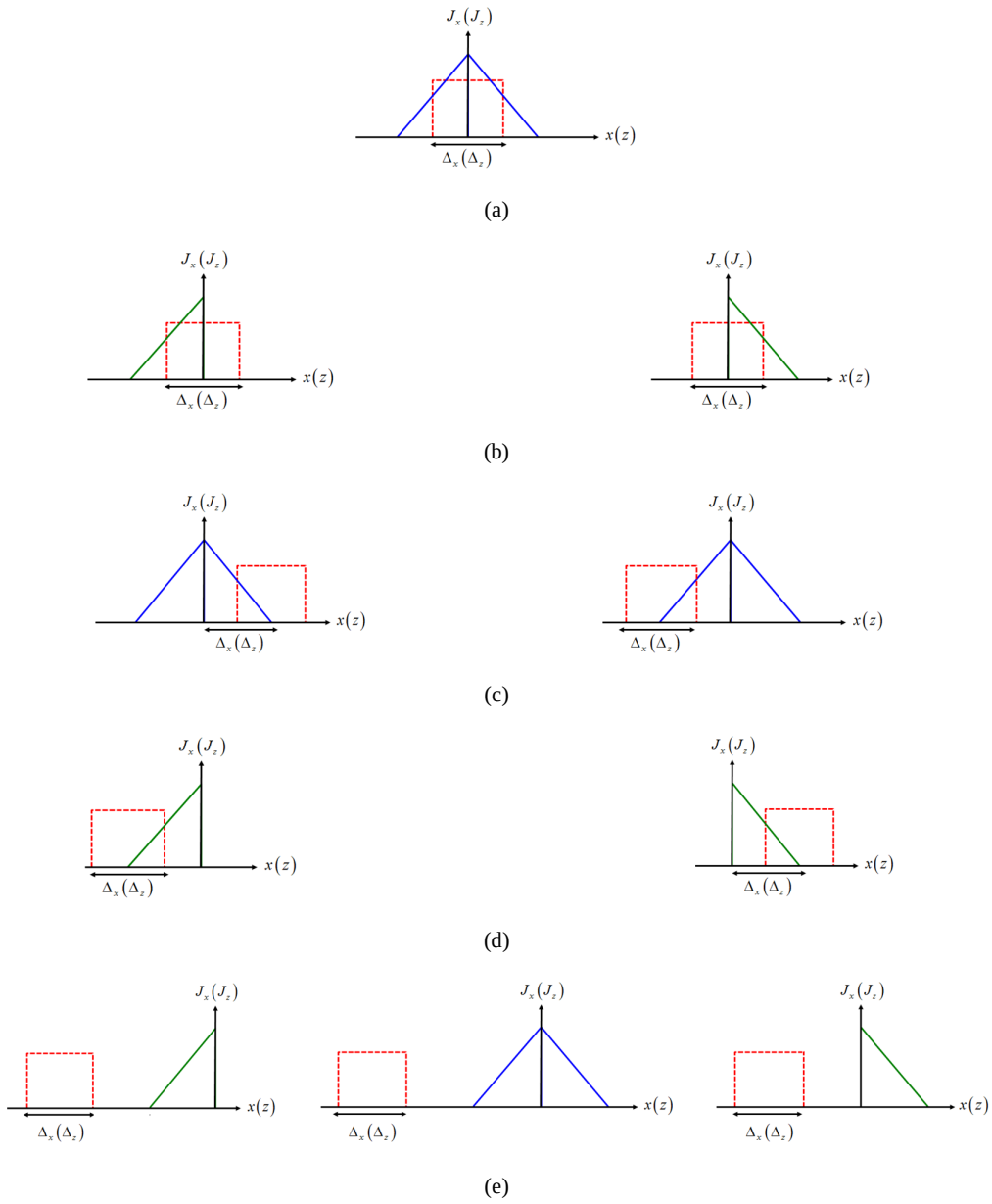

Figure 3.4: Different cases describing the overlap between the current basis and test functions along the *x*- or *z*-axis: (a) the basis and test functions have the same centre, and the basis function is represented by an even triangular prism (b) the basis and test functions have the same centre, and the basis function is represented by either a right or left triangular prism, (c) the basis and test functions are shifted with a value of Δ_x or Δ_z, and the basis function is represented by an even triangular prism, (d) the basis and test functions are shifted with a value of Δ_x or Δ_z, and the basis function is represented by a right or left triangular prism, (e) the basis and test functions do not overlap. The red dashed colour corresponds to the test function while the blue (green) solid lines correspond to the basis function.

3.5 Conclusions

This chapter presents the method of calculating the propagation characteristics of plasmonic transmission lines using the MoM technique. First, the transmission line is meshed into smaller segments where the current is expanded using known basis functions weighted by unknown expansion coefficients. After meshing the plasmonic strip(s), the expressions of the currents are applied to the integral equation relating the electric field to the electric current density. The following step is to apply the boundary condition along the metal strips, which takes the form of a relationship between the electric field and electric current at different test points along the strip(s). In order to enhance the accuracy of satisfying the boundary condition using reasonable number of test points, the boundary condition is satisfied on integral sense using suitable testing technique, such as razor-blade. Doing this, we reach a matrix equation where the unknown(s) is (are) the propagation constant(s) of the modes and the corresponding current weights. This equation has been solved for the propagation constant(s) and its (their) current profile(s) via Müller and singular value decomposition techniques, respectively.

Chapter 4: Numerical Examples for Plasmonic Transmission Lines

In this chapter, the developed MoM-based solver is tested on different plasmonic transmission line topologies in order to verify their calculated propagation characteristics (i.e. guided wavelength, insertion losses and modal current). The transmission lines considered in this work have various cross-sections, number of metallic strips, and/or are arranged in different layer structures. The diversity of these examples demonstrates that the proposed solver is generic. For all examples considered, the metallic strips are made of gold material which has the following Drude model parameters [9] $\varepsilon_\infty = 9.069$, $\omega_p = 1.354 \times 10^{16}$ rad/s, and $f_c = 1.2 \times 10^{14}$ s^{-12}. The frequency considered in this work ranges from 150 THz to 400 THz corresponding to a wavelength (2 µm – 0.75 µm). The chapter starts by the simplest case where the plasmonic transmission line is placed in free-space. Single and coupled strips transmission lines are studied. Additionally, circular and triangular strips are presented in order to verify that the solver is capable of calculating the propagating characteristics of any topology. The second section of this chapter deals with transmission lines located within a layered medium, which is more practical. The Green's functions in this case are more complicated as discussed earlier. Plasmonic strips at the interface of an infinite half-space and on top of finite thickness dielectric material backed with finite plasmonic metals are both considered. The last section deals with plasmonic transmission

lines located at the middle of the layered medium which is the most generic case. An example of a plasmonic strip is studied in this section.

4.1 Plasmonic Transmission Lines in Homogeneous Medium

This section presents a study of different plasmonic transmission lines located in homogeneous medium. Specifically, free-space is considered as the background medium. The topologies include single rectangular strip, horizontally coupled strips, vertically coupled strips, triangular strip, and circular strip. All strips are made up of gold material due to its relatively low losses in the visible and near infrared range compared to other materials [91]. The cross-sectional dimensions of the transmission lines under investigation are shown symbolically in Figure 4.1.

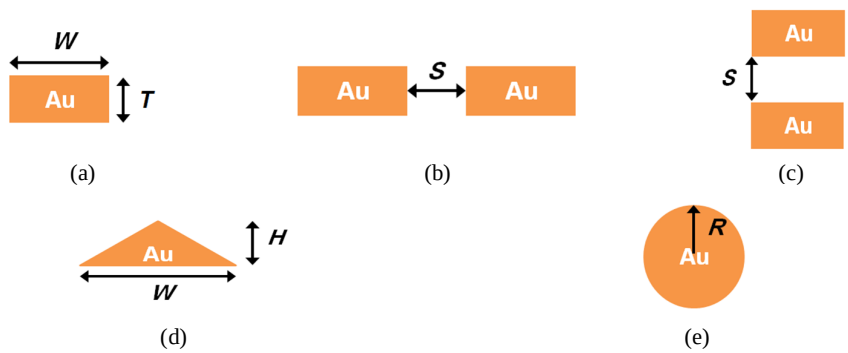

Figure 4.1: Plasmonic transmission lines located in free-space under investigation: (a) single rectangular strip, (b) horizontally coupled strips, (c) vertically coupled strips, (d) triangular strip and (e) circular strip.

4.1.1 Single Rectangular Strip

Unlike microwave transmission lines, a single strip plasmonic transmission line can support a propagating mode. This is due to the fact that a single metal/dielectric interface can guide a SPP wave. The single strip line in Figure 4.1(a) has a width $W = 50$ nm and thickness $T = 20$ nm. Square cells with dimension 2.5 nm (or less) along both x- and z-directions are used to mesh this strip, i.e. $\Delta_x = \Delta_z \leq 2.5$ nm. As the frequency increases, the guided wavelength decreases; thus, smaller mesh is essential to obtain more accurate results. The unknown propagation constant k_y is complex, such that: $k_y = \beta - j\alpha$, where β and α are the phase constant and attenuation constant, respectively. The normalized phase constant represents the effective refractive index, n_{eff}, of the propagating mode, such that: $n_{\text{eff}} = \beta c/\omega$, where c is the velocity of electromagnetic wave propagation in free-space. Figure 4.2 shows n_{eff} and the insertion loss, IL, of the fundamental mode versus frequency as calculated using our solver, and CST [92]. The insertion loss can be calculated from the attenuation constant as follows:

$$IL(\text{dB}/\mu\text{m}) = 20 \log_{10}\left(e^{\alpha \times 10^{-6}}\right) \tag{4.1}$$

Comparing the results of both solvers, it can be noticed that there is a very good agreement between them. Along the calculated bandwidth, the maximum percentage difference between both simulators is 2.21%. It is also clear from Figure 4.2 that as the frequency of operation increases, the effective refractive index and the attenuation constant increase. This can be explained from the fact that at optical frequency range, the skin depth δ is expressed as follows [93]:

$$\delta = \frac{\lambda_0}{2\pi \ \mathrm{Im}(n)} \tag{4.2}$$

where λ_0 is the free-space wavelength, and Im(n) is the imaginary part of the complex refractive index of the metal, which can be calculated as follows [93]:

$$\mathrm{Im}(n) = \sqrt{0.5(\sqrt{\varepsilon'^2 + \varepsilon''^2} - \varepsilon')} \tag{4.3}$$

For gold, the skin depth versus frequency is plotted in Figure 4.3. From this figure, it is clear that the skin depth increases with increasing the frequency of operation. This means more current penetration inside the lossy gold strip leading to higher effective refractive index and more attenuation for the propagating mode.

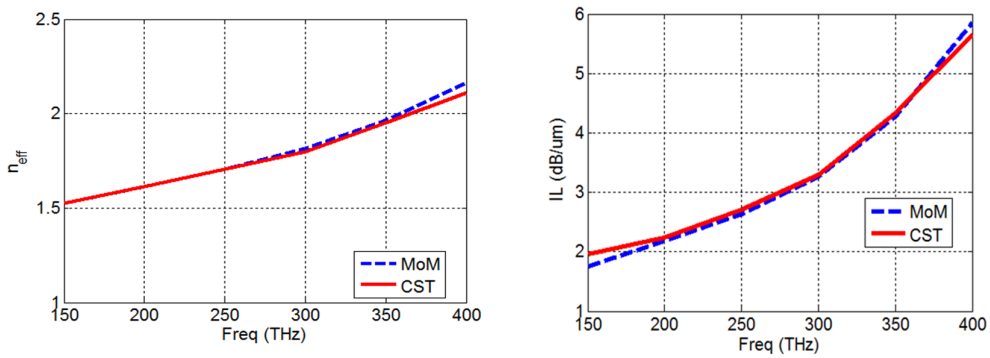

(a) (b)

Figure 4.2: Propagation characteristics versus frequency of the propagating mode along the single gold strip of dimensions W = 50 nm, T = 20 nm: (a) effective refractive index, and (b) insertion loss.

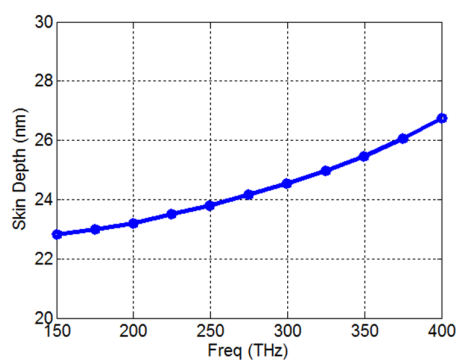

Figure 4.3: Skin depth of gold metal versus frequency.

Using the calculated value of the propagation constant $k_y = 6.286\times10^6 - j\,2.275\times10^5$ rad/m at $\lambda = 1.55$ μm (frequency = 193.55 THz), the unknown modal current distribution along *x*-, *y*-, and *z*-axes is obtained and plotted in Figure 4.4. The dominant current component is the longitudinal J_y component along the direction of wave propagation, with maximum absolute value at the edges of the strip and minimum absolute value at its centre. The J_x component is maximum at the perpendicular right- and left-hand side edges of the strip with odd symmetry. On the other hand, the J_z component can be considered as the rotated version of the J_x component, showing maximum values at the perpendicular upper and lower edges with odd symmetry. It is worth mentioning that the transverse currents J_x, and J_z are in phase, while the longitudinal current J_y lags the transverse currents by 90°. Unlike the microwave transmission lines, the currents of this plasmonic line are no longer along the circumference of the strip, but they penetrate inside the metal strip. This is expected as the imaginary part of the permittivity of gold at optical frequencies is no longer much higher than the real part. In other words, metals at optical frequencies are not totally lossy and they allow field penetration within them to some extent, as mentioned earlier.

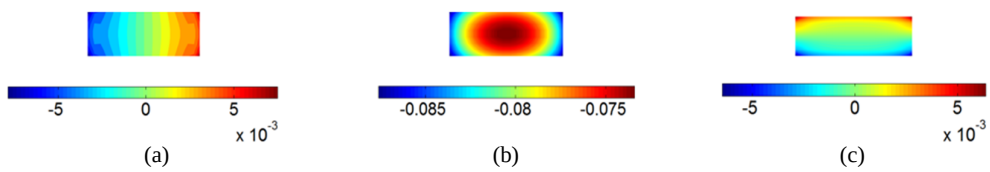

Figure 4.4: Modal current distribution of the propagating mode supported by the single gold strip of dimensions W = 50 nm and T = 20 nm at 193.55 THz (λ = 1.55 μm): (a) *x*-component (J_x), (b) *y*-component (J_y), and (c) *z*-component (J_z).

4.1.2 Horizontally Coupled Strips

In this section, a transmission line consisting of two gold strips of width W = 50 nm and thickness T = 20 nm, are aligned horizontally with a spacing S = 20 nm between them, as shown in Figure 4.1(b). This transmission line supports two propagating modes, which are referred to as the *even* and *odd* modes. The *even* (*odd*) mode corresponds to the case when the longitudinal current is symmetric (anti-symmetric). The modal current distributions of these modes at f = 193.55 THz (λ = 1.55 μm), are shown in Figure 4.5, and 4.6, respectively. According to these figures, the dominant current component, J_y, has even and odd symmetry, respectively. For the even mode, the currents are maximum at the external edges of the two strips. For the odd mode, the maximum current is at the inner edge of each strip. Similar to the single strip case, the longitudinal current J_y lags the transverse currents J_x and J_z by 90° for both modes. Figure 4.7 shows the propagation characteristics of the even and odd modes of this transmission line versus frequency. The developed MoM solver shows a very good agreement with CST for the two propagating modes. Both modes have effective refractive index and insertion loss increasing with the increase of the frequency of operation, which is similar to the single strip case. With respect to the even mode, the odd mode has higher n_{eff}, which means higher percentage energy in the metal strips, leading to more insertion losses.

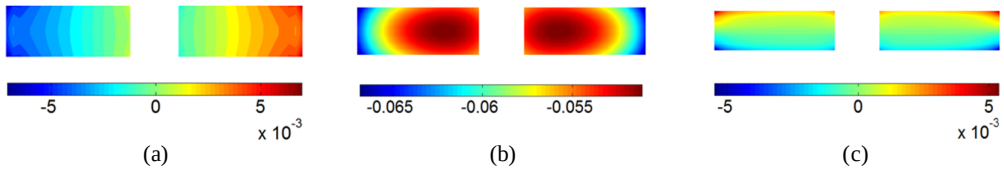

Figure 4.5: Modal current distribution of the even mode of the horizontally coupled strips of dimensions W = 50 nm, T = 20 nm, and S = 20 nm at 193.55 THz (λ = 1.55 μm): (a) x-component (J_x), (b) y-component (J_y), and (c) z-component (J_z).

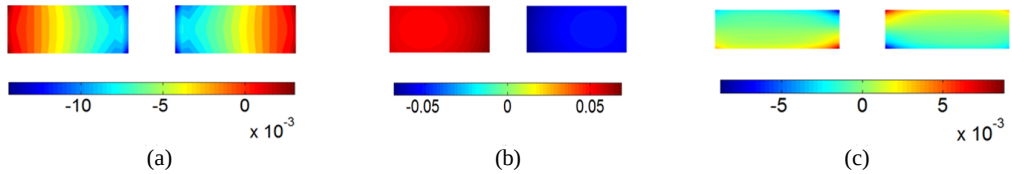

Figure 4.6: Modal current distribution of the odd mode of the horizontally coupled strips of dimensions W = 50 nm, T = 20 nm and S = 20 nm at 193.55 THz (λ = 1.55 μm): (a) x-component (J_x), (b) y-component (J_y), and (c) z-component (J_z).

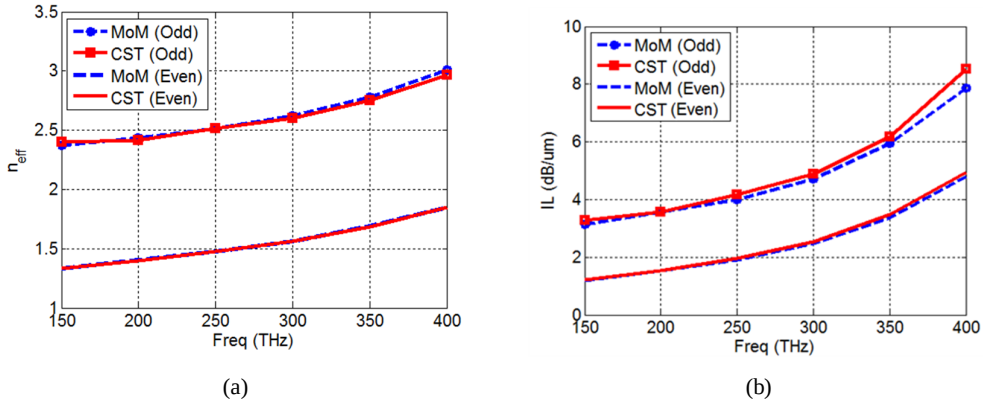

Figure 4.7: Propagation characteristics versus frequency of the propagating modes along the horizontally coupled strips of dimensions W = 50 nm, T = 20 nm and S = 20 nm: (a) effective refractive index, and (b) insertion loss.

4.1.3 Vertically Coupled Strips

Now, the two strips with W = 50 nm and T = 20 nm are placed on top of each other with vertical spacing S = 20 nm, as shown in Figure 4.1(c). Similar to the horizontally coupled transmission line, this structure also supports two propagating modes, whose modal current distribution at λ = 1.55 μm are plotted in Figures 4.8, and 4.9. The longitudinal current components suggest that these are the *even* and *odd* modes, respectively, with 90° phase difference between the transverse and longitudinal currents. The effective refractive index as well as the insertion loss of the two propagating modes is plotted versus frequency in Figure 4.10. Good agreement with CST can be noticed for the two propagating modes.

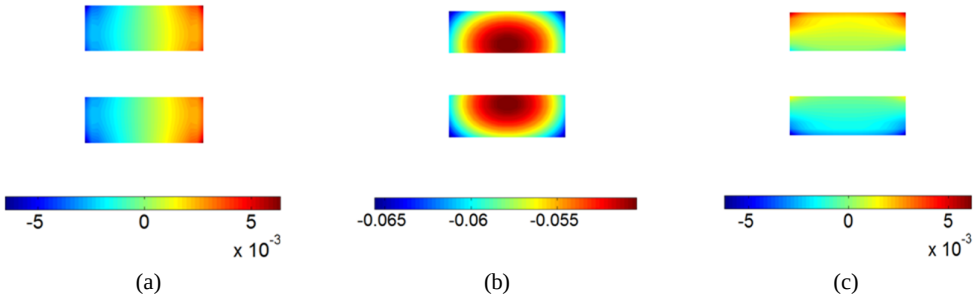

Figure 4.8: Modal current distribution of the even mode of the vertically coupled strips of dimensions W = 50 nm, T = 20 nm, and S = 20 nm at 193.55 THz (λ = 1.55 µm) (a) x-component (J_x), (b) y-component (J_y), and (c) z-component (J_z).

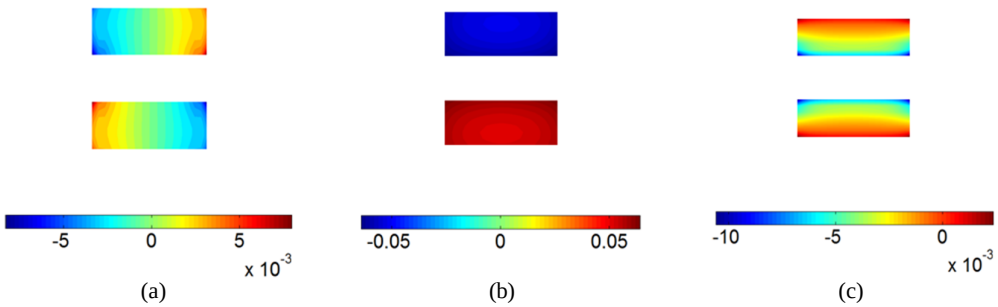

Figure 4.9: Modal current distribution of the odd mode of the vertically coupled strips of dimensions W = 50 nm, T = 20 nm, and S = 20 nm at 193.55 THz (λ = 1.55 µm): (a) x-component (J_x), (b) y-component (J_y), and (c) z-component (J_z).

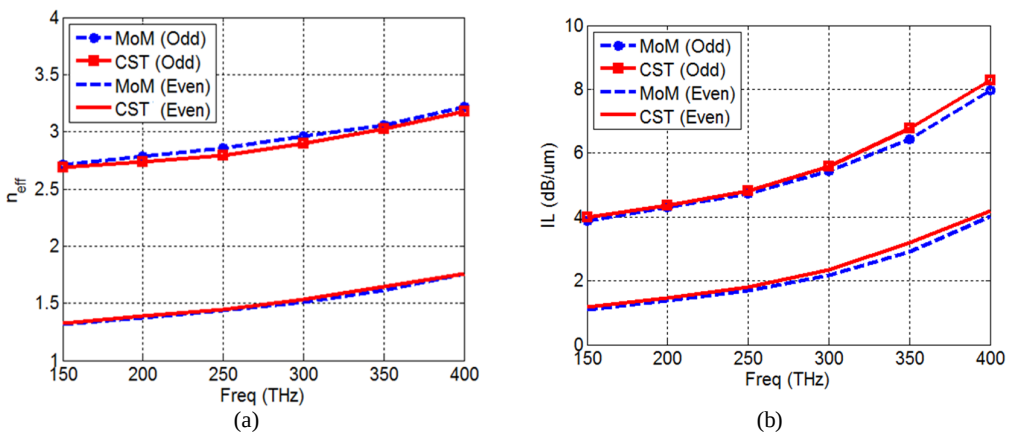

Figure 4.10: Propagation characteristics versus frequency of the propagating modes along the vertically coupled strips of dimensions W = 50 nm, T = 20 nm, and S = 20 nm: (a) effective refractive index, and (b) insertion loss.

Comparing the results of the horizontally and vertically coupled strips, the insertion loss is higher for the later case. This can be attributed to the fact that metallic surfaces facing each other are wider in the later case, which results in more losses within the metal volume. It is worth noting that the developed solver takes into account the coupling between the strips since the test function locations have the same locations as the basis functions.

4.1.4 Triangular and Circular Strips

In order to demonstrate the flexibility of the proposed formulation, strips with non-rectangular cross-section are considered. Specifically, the triangular and circular strips of Figure 4.1(d) and (e) are investigated. The dimensions of these transmission lines are: W = 50 nm, H = 25 nm, and R = 50 nm. For such structures, the cross-section is approximated by a stair-case mesh. The cell size used for both examples has dimensions $\Delta_x = \Delta_z =$ 2.5 nm. Figure 4.11 shows the effective refractive index and the insertion loss of these transmission lines as calculated by our solver, and CST. From the figure, it is clear that the effective refractive index and the insertion loss increase as the frequency increases similar to the previous examples of strips with rectangular cross-section. It is also clear that the agreement between the two solvers is very good, which validates the obtained results and proves the versatility of the proposed formulation.

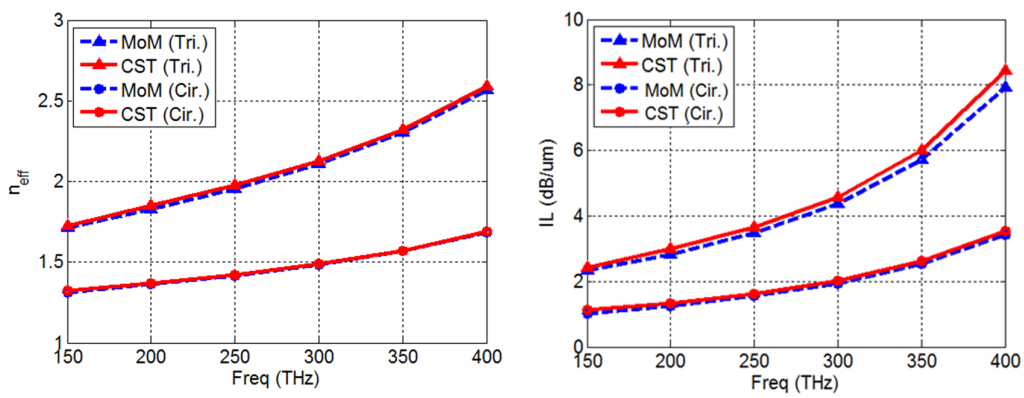

(a) (b)

Figure 4.11: Propagation characteristics versus frequency of the propagating modes along the triangular (Tri.) and circular (Cir.) strips of dimensions W = 50 nm, H = 25 nm, and R = 50 nm at 193.55 THz (λ = 1.55 μm): (a) effective refractive index, and (b) insertion loss.

The MoM is considered a powerful tool for the calculation of the propagation characteristics of transmission lines. The strength of the MoM arises from the fact that it requires meshing for only the surface of the metallic strips. On the other hand, CST, which is based on the finite difference method, requires substantial additional meshing for the space surrounding the strips. This additional space should be made wide enough to ensure that the fields are not strongly disturbed by the truncation boundaries. Consequently, the number of unknowns is way larger than that of the MoM. Table 4.1 shows a comparison of the number of unknowns used in calculating the propagation characteristics of the single rectangular strip, horizontally coupled strips, vertically coupled strips, triangular strip, and circular strip in free-space using both solvers at 193.55 THz (1.55 μm). It is clear that our solver requires much less number of unknowns compared to CST software, illustrating the intrinsic supremacy of this technique for this type of problem.

Table 4.1: Number of unknowns required to calculate the propagation characteristics of the plasmonic transmission lines at 1.55 μm

	MoM Solver	CST
Single Rectangular Strip	1016	39192
Horizontally Coupled Strips	2032	68040
Vertically Coupled Strips	2032	74580
Triangular Strip	900	150672
Circular Strip	2184	102375

4.2 Plasmonic Transmission Lines at the Interface of Two Half-Spaces

This section shows the study of various plasmonic transmission lines located at the interface of two infinite half-spaces. Figure 4.12 shows the various plasmonic transmission lines considered namely: single strip, horizontally coupled strips, and U-shaped strip. As mentioned in chapter 3, the DCIM method is required to obtain the spatial domain Green's functions from their spectral domain counterpart. In this section, the terms β_1 and β_2 appearing in equations (2.131), and (2.132) are considered to be equal to $50k_0$, and $5k_0$ respectively. These values are found suitable for the layered media under investigation. The effects of varying the main geometrical parameters of the transmission lines on their propagation characteristics are also studied in this section.

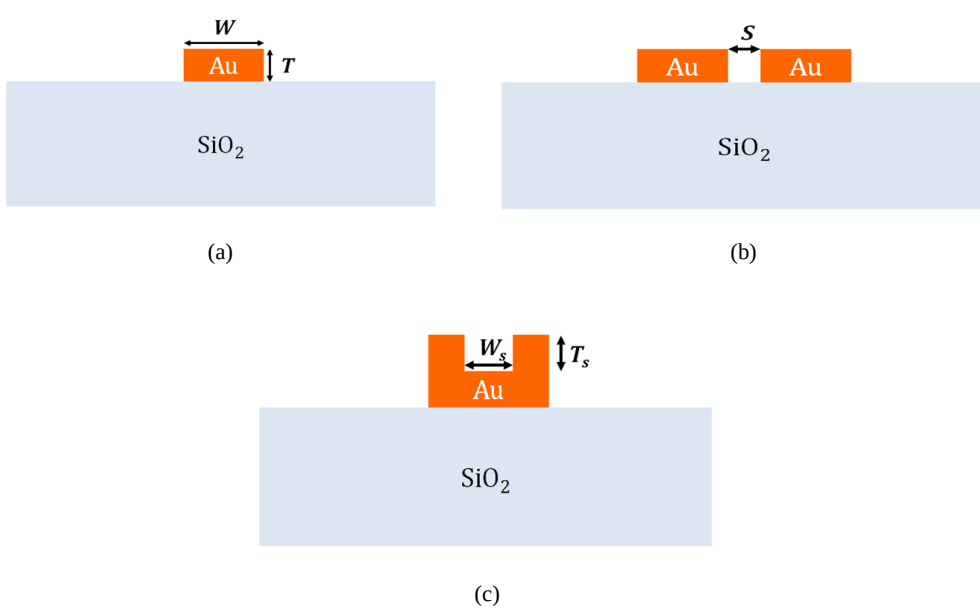

Figure 4.12: The various plasmonic transmission lines under investigation: (a) single gold strip on top of SiO_2 substrate, (b) horizontally coupled gold strips on top of SiO_2 substrate, and (c) U-shaped plasmonic gold strip placed on top of SiO_2 substrate.

4.2.1 Single Strip on Top of SiO_2 Substrate

In this section, the propagation characteristics of the fundamental mode of a rectangular gold strip on top of SiO_2 substrate ($\varepsilon_r = 2.15$), as shown in Figure 4.12(a), are investigated. At optical frequencies, the guided wavelength is in the range of a few micrometres. Therefore, the thickness of the substrate is much larger than the wavelength. As a result, the assumption of a gold strip placed on top of an infinite substrate is considered a valid approximation.

The dimensions of the gold strip considered in this example are: W = 50 nm and T = 20 nm, similar to the previous examples. Figure 4.13 shows the dispersion curves as simulated using our solver and CST. Both solvers have closely matched results. They show that as the frequency increases, the effective refractive index (n_{eff}) and the insertion loss (IL) of the strip increases, similar to the case of plasmonic gold strip in free-space. At 193.55 THz (1.55 µm), the propagation constant calculated using our solver is: $k_y = 8.23\times10^6 - j\,3.14\times10^5$. At this frequency, the x-, y-, and z- current components are shown in Figure 4.14. As expected, the current penetrates the gold strip due to the dielectric nature of gold at optical frequencies. Furthermore, Figure 4.14 shows that the y-component of the current density J_y is dominant, but the x- and z- current components cannot be ignored. For J_y, it is noticed that the current is maximum along the strip edges compared to its centre and it is symmetric along the x-axis. On the other hand, J_y is not symmetric across the z-axis where it has higher values at the lower edge, i.e. along the interface of the gold strip with the silicon dioxide layer. This is expected due to the relatively high dielectric permittivity of SiO_2, the lower half-space compared to free-space, the upper half-space. The x- and z- current components shown in Figure 4.14(a) and (c) have an odd (even) symmetry along the z-axis. The maximum current for J_x (J_z) is along the right and left (upper and bottom) edges of the strip. It is worth mentioning that the longitudinal current J_y lags the transversal currents J_x and J_z with 90 degrees in phase.

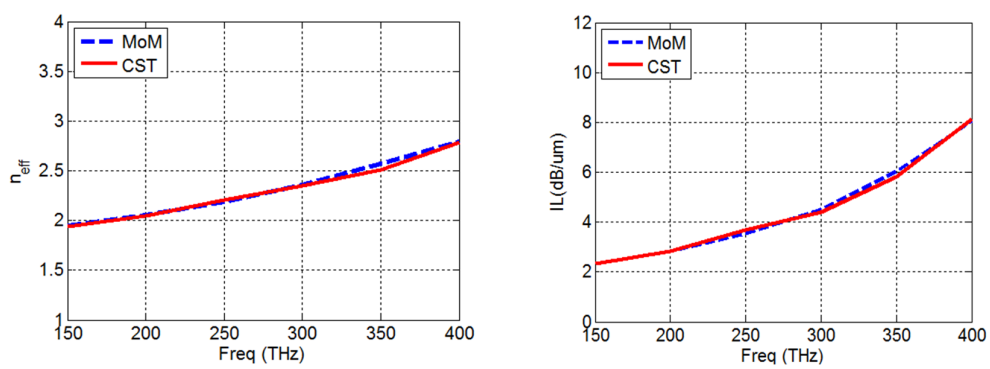

(a) (b)

Figure 4.13: Propagation characteristics of a single gold strip of dimensions W = 50 nm and T = 20 nm on top of an infinite silicon dioxide substrate: (a) effective refractive index, and (b) insertion loss.

The effect of varying the geometrical parameters W and T of the gold strip on its propagation characteristics is shown in Figure 4.15, as simulated using the developed solver

at 193.55 THz. The width (W) is varied from 30 nm till 70 nm while keeping the strip thickness fixed at T = 20 nm. On the other hand, Figure 4.16 shows the effect of varying the thickness (T) from 10 nm till 30 nm at constant width of W = 50 nm. As shown in these figures, decreasing W or T leads to increasing both the effective refractive index and the insertion loss. This is due to the higher confinement of the wave inside the plasmonic gold strip, which is characterized by its high dielectric constant and high losses.

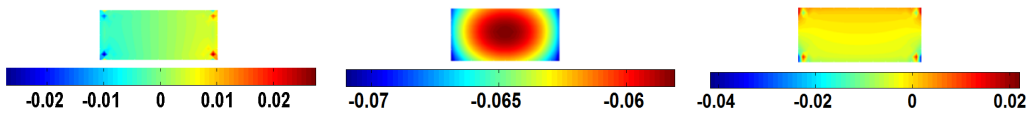

(a) (b) (c)

Figure 4.14: Current distribution along the plasmonic gold strip of dimensions W = 50 nm and T = 20 nm above the SiO_2 substrate at 193.55 THz (1.55 µm) as obtained using our solver: (a) x-component (J_x), (b) y-component (J_y), and (c) z-component (J_z).

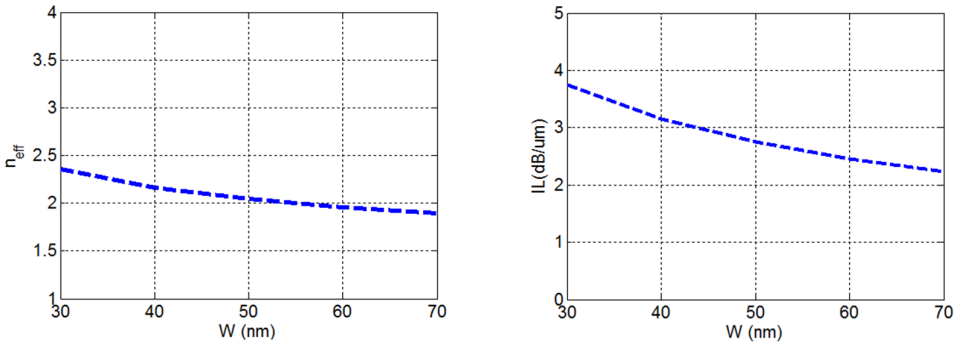

(a) (b)

Figure 4.15: The effect of varying the strip width (W) of the plasmonic gold strip on top of the SiO_2 substrate on the propagation characteristics as simulated using the MoM-solver at 193.55 THz (1.55 µm) when the strip thickness T = 20 nm: (a) the effective refractive index, and (b) the insertion loss.

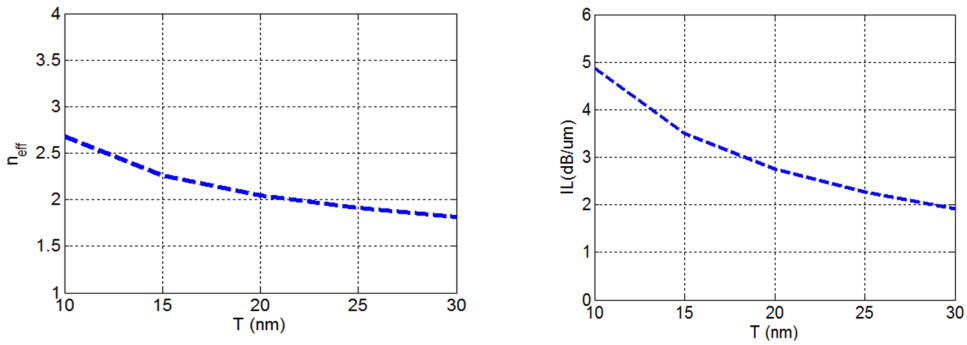

(a) (b)

Figure 4.16: The effect of varying the strip thickness (T) of the plasmonic gold strip on top of the SiO_2 substrate on the propagation characteristics as simulated using the MoM-solver at 193.55 THz (1.55 µm) when the strip width W = 50 nm: (a) the effective refractive index, and (b) the insertion loss.

It is worth noting that the proposed MoM-based solver has the significant advantage of reducing the number of unknowns compared to CST. For instance, in the example of the single plasmonic strip, the proposed solver requires from 160 (20×8) to 460 (40×16) mesh cells for the 50 nm × 20 nm nano-strip. The number of mesh cells is determined according to the operating frequency. On the other hand, CST requires (18,000-35,000) cells to obtain the same results. The significantly reduced number of unknowns (by three orders of magnitude) results in a lower intrinsic need of computational resources when compared to CST.

4.2.2 Horizontally Coupled Strips on Top of SiO_2 Substrate

The horizontally coupled plasmonic transmission line considered in this section consists of two symmetric gold strips of width W and thickness T, separated by a distance S, as shown in Figure 4.12(b). The strips are placed on top of a silicon dioxide substrate like in the previous example. This type of transmission line is capable of supporting two main modes namely the *even* (symmetric) and the *odd* (asymmetric) mode, similar to the coupled strip transmission lines in free-space. Figure 4.17 shows the propagation characteristics of the two modes for gold strips of the following dimensions: W = 50 nm, T = 20 nm, and S = 20 nm. The behaviour of n_{eff} and IL versus frequency is similar to that of the single strip. Increasing the frequency results in higher n_{eff} and IL. Figure 4.17 also shows that the even mode has lower values of the propagation constant, and consequently lower propagation losses, compared to the odd mode. The current mode profiles for the propagating modes along the horizontally coupled strips are shown in Figures. 4.18, and 4.19 at 193.55 THz. The even mode ($k_y = 7.31\times10^6 - j\,2.26\times10^5$ rad/m) has symmetric J_y (longitudinal) and J_z (transversal) currents along the two strips and anti-symmetric J_x (transversal) current. On the contrary, for the odd mode ($k_y = 1.16\times10^7 - j\,4.79\times10^5$ rad/m), the longitudinal current J_y and the transversal current J_z have odd symmetry, while J_x has even symmetry.

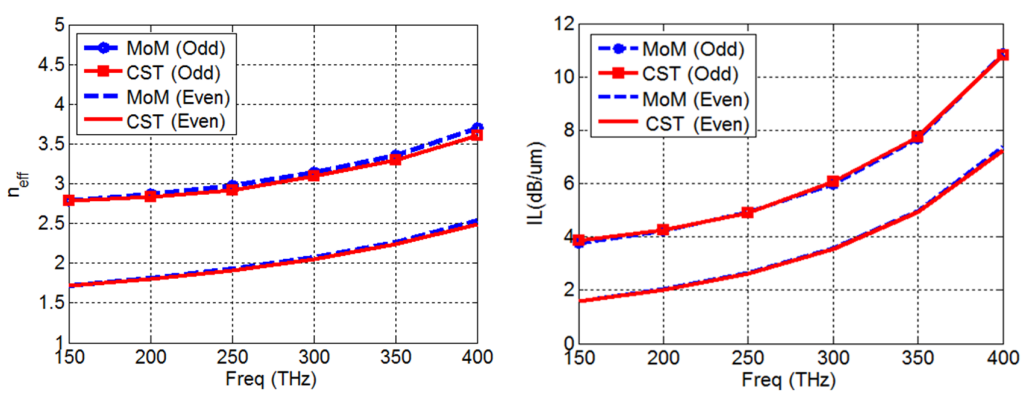

(a) (b)

Figure 4.17: Propagation characteristics of the horizontally coupled gold strips of dimensions W = 50 nm, T = 20 nm, and S = 20 nm on top of an infinite silicon dioxide substrate: (a) effective refractive index, and (b) insertion loss.

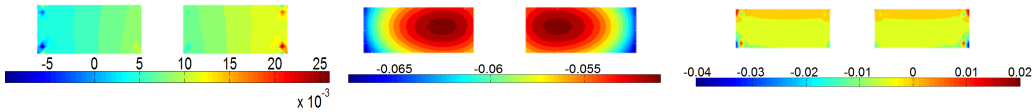

(a) (b) (c)

Figure 4.18: Current distribution of the even-mode along the cross-section of the horizontally coupled gold strips (W = 50 nm, T = 20 nm, and S = 20 nm) on top of SiO_2 substrate at 193.55 THz (1.55 µm) as obtained using the MoM technique(a) x-component (J_x), (b) y-component (J_y), and (c) z-component (J_z).

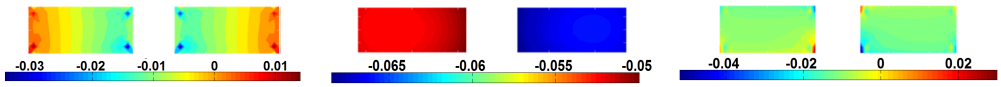

(a) (b) (c)

Figure 4.19: Current distribution of the odd-mode along the cross-section of the horizontally coupled gold strips (W = 50 nm, T = 20 nm, and S = 20 nm) on top of SiO_2 substrate at 193.55 THz (1.55 µm) as obtained using the MoM technique: (a) x-component (J_x), (b) y-component (J_y), and (c) z-component (J_z).

4.2.3 U-shaped Strip on Top of SiO_2 substrate

The developed solver has also been examined for plasmonic transmission lines of various topologies including the U-shaped structure, shown in Figure 4.12 (c). Similar to the previous examples, this transmission line is placed on top of a SiO_2 substrate. The dimensions of this strip are given by W = 80 nm, T = 20 nm, W_s = 40 nm, and T_s = 10 nm. Figure 4.20 shows the variation of n_{eff} and IL versus frequency. Simulations using the MoM solver and CST are in a very good agreement. As can be concluded from the previous examples, the agreement between both solvers demonstrates that the developed solver is capable of solving plasmonic transmission lines of any topology constructed from one or more plasmonic strips.

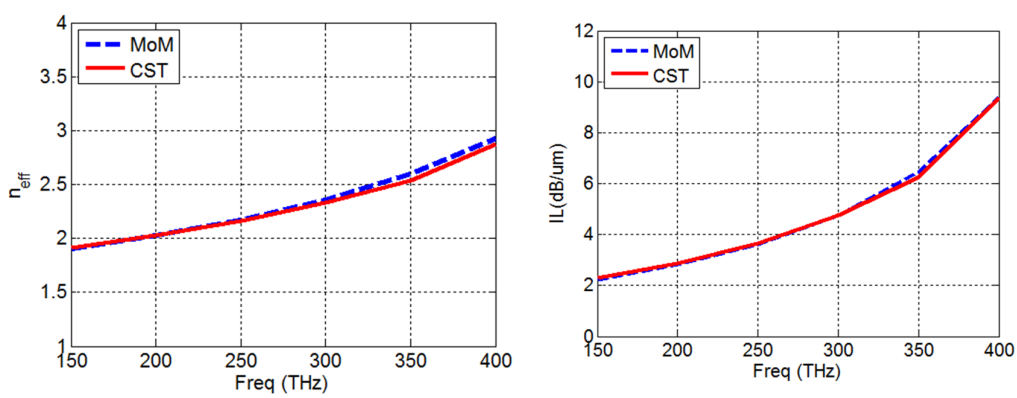

(a) (b)

Figure 4.20: Propagation characteristics of a U-shaped gold strip of dimensions: W = 80 nm, T = 20 nm, W_s = 40 nm, and T_s = 10 nm on top of an infinite silicon dioxide substrate: (a) effective refractive index, and (b) insertion loss.

4.3 Plasmonic Nano-Strip on Top of SiO_2 Layer Backed with Au Ground Layer

For the case of plasmonic transmission line placed in a three-layered structure, the simple nano-strip placed on top of a finite thickness SiO_2 layer backed with a thick Au layer is examined. Figure 4.21 shows the topology of the nano-strip which has width *W*, and thickness *T*, similar to the previous examples. The thickness of SiO_2 layer is denoted by *H*.

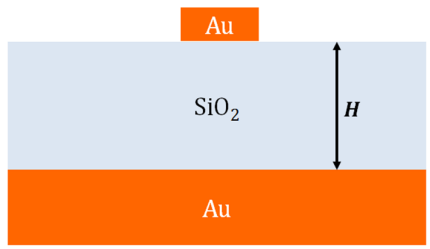

Figure 4.21: Plasmonic gold nano-strip placed on top of SiO_2 substrate backed by gold ground layer.

The dimensions chosen for the nano-strip are as follows: W = 50 nm, T = 20 nm, and H = 100 nm. The propagation characteristics of this transmission line are shown in Figure 4.22. They have quite similar behaviour compared to the single strip transmission line, discussed in section (4.2.1). The effective refractive index and the insertion losses increase with increasing frequency. Comparing with the single strip transmission line, the nano-strip transmission line has higher n_{eff} and *IL*. This is due to the presence of the gold layer, which has higher dielectric permittivity and losses, compared to SiO_2. As shown in Figure 4.23, by increasing the SiO_2 thickness (*H*), n_{eff} and *IL* decrease. This is due to the fact that the gold layer is located further away from the nano-strip and has weaker effect on the transmission line propagation characteristics. Further increasing of the SiO_2 thickness tends to make the propagation characteristics of this transmission line resemble that of the singular rectangular strip of the same dimensions placed on top of infinite SiO_2 substrate.

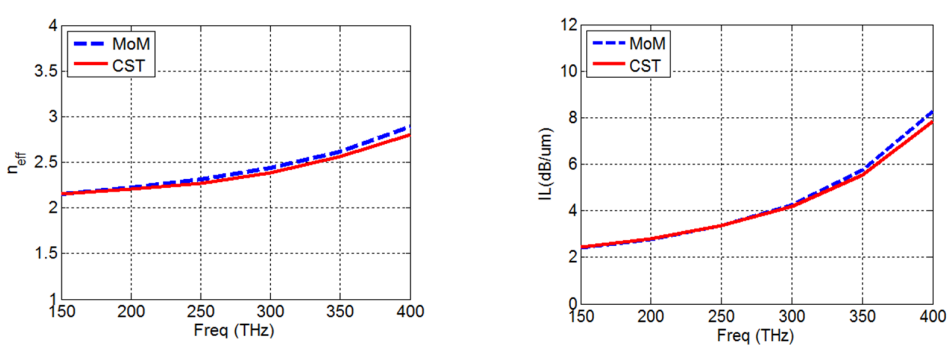

Figure 4.22: Propagation characteristics of a single gold nano-strip of dimensions W = 50 nm and T = 20 nm on top of a 100 nm thick SiO_2 substrate backed with infinite ground gold layer: (a) effective refractive index, and (b) insertion loss.

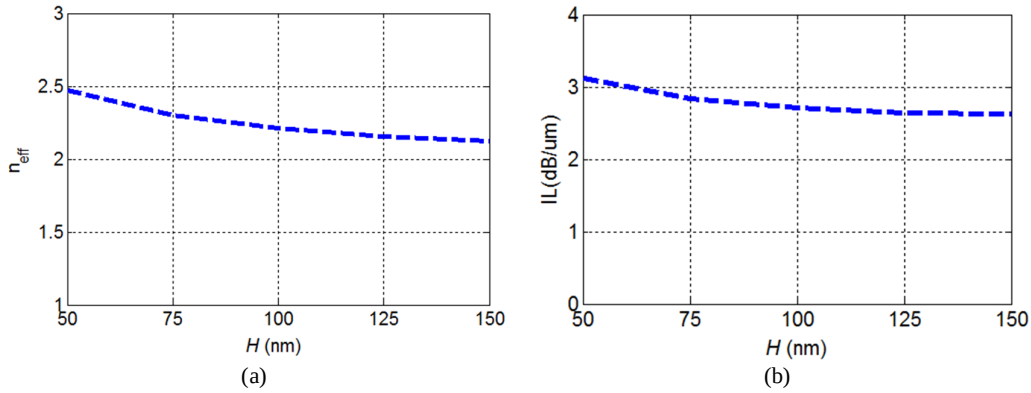

Figure 4.23: The effect of varying the SiO_2 substrate thickness on the propagation characteristics of the plasmonic gold nano-strip (W = 50 nm and T = 20 nm) as simulated using the MoM-based solver at 193.55 THz (1.55 μm): (a) the effective refractive index, and (b) the insertion loss.

4.4 Plasmonic Nano-Strip Embedded in SiO_2 Layer Backed with Thick ITO Layer

In this section, a plasmonic transmission line embedded in a finite thickness layer is studied. Figure 4.24 shows the structure of the transmission line considered. It consists of a simple gold strip with dimensions W = 50 nm, and thickness T = 20 nm. The gold strip is surrounded by SiO_2 layer. The upper half-space is considered to be free-space and the lower half-space is considered to be Indium-Tin Oxide of dielectric constant: $\varepsilon_r = 4$. For this example, the parameters considered for the DCIM are $\beta_1 = 100$, $\beta_2 = 20$, $N_1 = 100$, and $N_2 = 100$. The propagation characteristics of this transmission line are shown in Figure 4.25. It shows that this line has the same increasing behaviour for the refractive index versus frequency like all the previous transmission lines. Compared to the gold strip in free-space and that above an infinite SiO_2 layer, the new transmission line has higher relative effective refractive index and losses. This is due to the higher dielectric permittivity of ITO compared to free-space and SiO_2. It is also clear from the figure that our solver and CST are in a good agreement.

Figure 4.24: Plasmonic gold strip placed inside SiO_2 layer backed by ITO half-space.

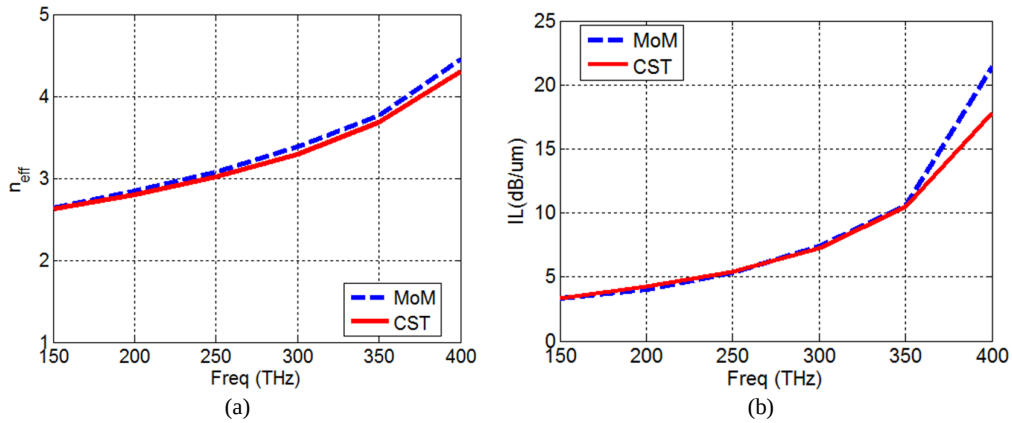

Figure 4.25: Propagation characteristics of a gold nano-strip of dimensions W = 50 nm and T = 20 nm inside 20 nm thick SiO_2 substrate backed with infinite layer of ITO: (a) effective refractive index, and (b) insertion loss.

4.5. Conclusions

In this chapter, the developed MoM mode solver is tested on various plasmonic transmission lines of different topologies, number of metallic strips and/or placed within various layered structures. The first section presents the simplest case where the plasmonic transmission line is placed in a homogeneous medium. In the second and third sections, plasmonic transmission lines placed in layered medium are studied. Section 4.2 presents the case when the transmission line is located at the interface of the first and second layer. Whereas, in section 4.3, a plasmonic transmission line in the middle layer is studied. These examples correspond to the various cases of the Green's functions which are analytically derived in chapter 2. In all examples studied, the results of the developed solver are compared to CST for verification. Generally, a very good agreement between both solvers is demonstrated. Knowing the propagation constant(s) of each transmission line, the solver is then used to provide the modal current distribution for each propagating mode. Additionally, the solver is also used to study the effect of varying the geometrical parameters of plasmonic transmission lines on their propagation characteristics. It is worth noting that by comparing the number of unknowns between our solver and that of CST, our solver has much reduced memory requirements, which is the major advantage of the MoM technique.

Chapter 5: Plasmonic Nano-Antennas

In this chapter, a number of plasmonic nano-antenna arrays are presented. The proposed arrays are in the form of a wire-grid, or brick-wall shape that does not require a separate complicated feeding network [94]. Consequently, these antennas are characterized by the simplicity of their design and fabrication. The wire-grid antennas consist of a number of radiators and perpendicular connectors. The adjustment of the lengths of these wires, results in currents with unified directions through the radiators, while the currents in the connectors are flowing in opposite directions. The radiators and connectors can be considered as plasmonic transmission lines, which guide SPPs. For each design, the basic element of the nano-antenna is first studied using the developed mode solver. The solver gives an approximation for the guided wavelength of the basic nano-rod, as well as the losses encountered per certain unit length. The effect of varying the antenna's geometrical parameters on its propagation characteristics is also studied using the developed solver which provides guidance for the design of the whole nano-antenna arrays. The chapter presents three wire-grid nano-antenna arrays. In section 5.1, the design of a five-element wire-grid array is introduced. For simplicity, the array is assumed to be in free-space. First, the propagation characteristics of the single nano-strip in free-space are studied and followed by the study of the radiation characteristics of the nano-dipole antenna. Afterwards, the whole wire-grid array is optimized for maximum directivity. The section

ends by studying the effect of adding a substrate underneath the antenna. In section 5.2, nano-antenna arrays placed in layered medium are studied. Two nano-antenna arrays are considered in this section. First, an eleven-element wire grid nano-antenna array is considered which is considered as an extended version of the five-element wire-grid array. As all the radiators are oriented in the same direction, the antenna provides linear polarization. The second array presented in this section provides circular polarization, where it is constructed from two groups of orthogonal arrays. The detailed analysis and the optimization procedure for both arrays are presented in this section. Finally, in section 5.3, the experimental results for two fabricated prototypes of wire-grid arrays on top of glass substrate are presented. A comparison between the simulations and experimental results are presented and discussed.

5.1 Wire-Grid Nano-Antenna in Free-Space

In this section, a wire-grid nano-antenna array consisting of five radiators is presented. Before the optimization of the whole structure, the single nano-strip is first studied using the developed plasmonic mode solver. Figure 5.1(a) shows the guided wavelength of the single strip plasmonic transmission line at 193.55 THz versus the width and thickness of the strip. The strip is made up of gold, whose dielectric permittivity is described by a Drude dispersive model. The strip is meshed using 6 segments along both the width and thickness. The insertion loss versus strip's dimensions is plotted in Figure 5.1(b). As these dimensions increase, the strip gains more skin for the current flow, which leads to a decrease in the insertion loss. According to this study, as the dimensions of the strip increase, the guided wavelength increases, while the insertion loss decreases. Consequently, a compromise should be performed between the size of the device, which is directly proportional to the guided wavelength, and the losses within the device.

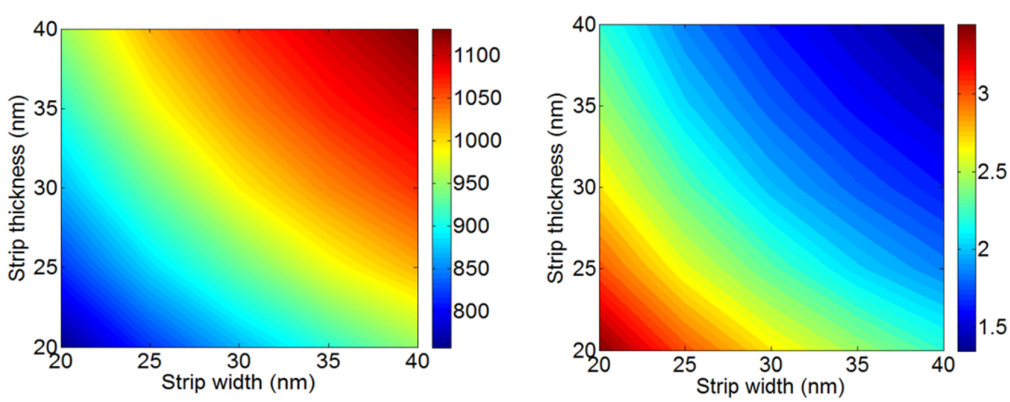

(a) (b)

Figure 5.1: Characteristics of the propagation mode of the single strip plasmonic transmission line versus the width and thickness of the strip at 193.55 THz: (a) guided wavelength (nm), and (b) insertion loss (dB/μm).

The modal current distribution along a strip's cross-section with dimensions of 30×30 nm at 193.55 THz is shown in Figure 5.2. The dominant current component is the longitudinal J_y component along the direction of wave propagation. This component shows cylindrical

symmetry around the centre of the strip with minimum value at the centre and maximum values at its corners due to the symmetry of the strip itself.

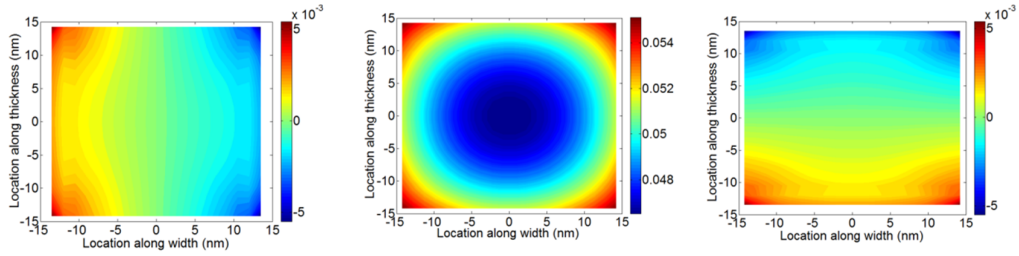

(a) (b) (c)

Figure 5.2: Modal current distribution of the propagating mode supported by the single strip at 193.55 THz: (a) *x*-component, (b) *y*-component, and (c) *z*-component.

For a strip with cross-sectional dimension of 30×30 nm, the guided wavelength and insertion loss are plotted versus frequency in Figures 5.3(a) and 5.3(b), respectively. The calculations are performed using the proposed the proposed MoM-based solver along with the mode solver of CST Microwave Studio. Good agreement can be observed, which validates the calculations.

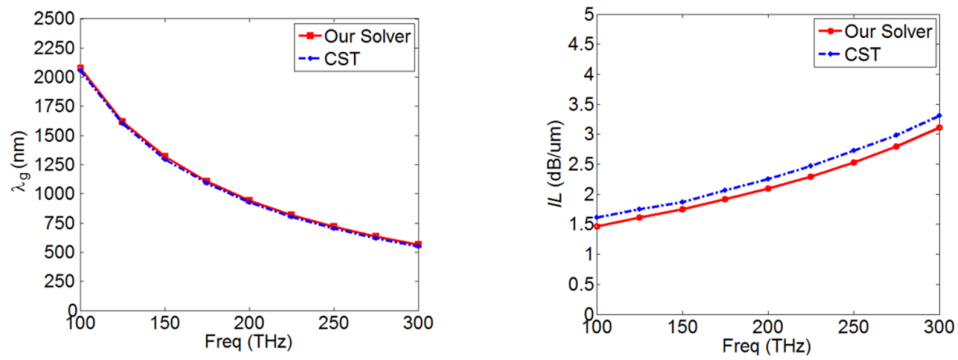

(a) (b)

Figure 5.3: Propagation characteristics versus frequency of the propagating mode along 30×30 nm single strip: (a) guided wavelength, and (b) insertion loss.

5.1.1 Reference Dipole Nano-Antenna

Figure 5.4 shows a single radiator in the form of a gold rod with square cross-section of 30 nm × 30 nm, and a length of L_{rad}. The selected cross-sectional dimensions offer good compromise between the size of the dipole nantenna and the losses within it. The gap width at the centre of the nano-rod is 30 nm. The rod is surrounded by free-space everywhere. The excitation is in the form of a localized voltage difference applied at the gap of the dipole, as shown in Figure 5.4. The selected operating wavelength is 1.55 μm, which is commonly used in optical communication systems. The corresponding frequency is 193.55 THz. The *z*-component of the magnetic field at 193.55 THz in the *xy*-plane containing the dipole is plotted in Figure 5.5 for different values of the dipole's length, L_{rad}. The simulations are

performed using the finite-difference time-domain solver of CST. The domain of calculation is truncated by perfectly matched layers (PML). Numerical convergence tests are always performed to ensure the validity of the used mesh. The red and blue colours in the field distributions of Figure 5.5 indicate positive and negative value of H_z, respectively. Hence, one can easily verify that the magnetic field is circulating around the longitudinal current flowing through the gold nano-rod. The objective of displaying the field distribution in Figure 5.5 is to estimate the value of the guided wavelength of a nano gold rod with 30 nm × 30 nm square cross-section. Comparing these field distributions, with the well-known current distributions of electric dipoles with different lengths [95], it becomes clear that the electrical lengths of the rods in Figure 5.5 are ($\lambda_g/4$), ($\lambda_g/2$), ($3\lambda_g/4$), (λ_g), and ($5\lambda_g/4$). Hence, the guided wavelength of this structure is approximately 700 nm, which is about half of the free-space wavelength of 1.55 μm.

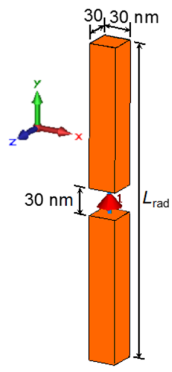

Figure 5.4: Single gold nano-rod in free-space.

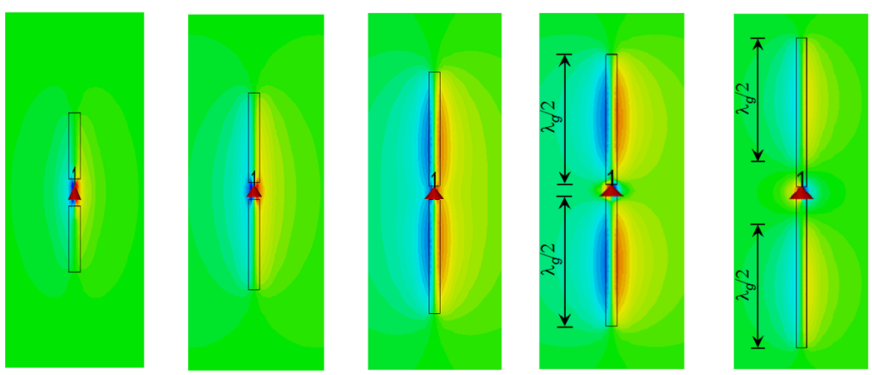

(a) (b) (c) (d) (e)

Figure 5.5: *z*-component of the magnetic field in the *xy*-plane containing the nano-rod at 193.55 THz (log scale): (a) L_{rad} = 175 nm, (b) L_{rad} = 350 nm, (c) L_{rad} = 525 nm, (d) L_{rad} = 700 nm, and (e) L_{rad} = 875 nm. Dark red and dark blue colours represent maximum positive and maximum negative value, respectively.

According to Figures 5.1(a) and 5.3(a), the guided wavelength calculated using the mode solver is 990 nm, which is higher than the predicted value using the field distribution. This difference is attributed mainly to the fringing of the field at the open circuit terminations, which does not occur in the case of an infinitely long strip analysed by the mode solver.

The 3D directivity pattern of the half-wavelength 350 nm dipole of Figure 5.5 (b) is shown in Figure 5.6 as obtained using CST at 193.55 THz. It takes the well-known "donut" shape [95], as expected. The principal cuts in this radiation pattern along the *E*-plane (*yz*) and *H*-plane (*xz*) are shown in Figure 5.7(a) and 5.7(b), respectively. The calculations are performed using CST and MAGMAS 3D [96], which is an in-house developed MoM solver. For the self and side-self terms, when there is an overlap between the test and basis functions, the (1/*R*) singularity is extracted from the Green's functions. The remaining is treated numerically, while the singular term is added analytically [97]. Very good agreement between CST and MAGMAS can be seen, which validates the presented results. The cross-polarization levels in the *E*- and *H*-plane are −30 dB and −35 dB, respectively. The directivity of this half-wavelength nano-rod is quite low, 1.8 dBi according to the CST calculation. Such quasi-uniform distribution of the radiated power is inconvenient for point-to-point communication systems, since most of the total power is wasted along unwanted directions. For such systems, a directive radiation pattern is required, which can be achieved via arraying a number of radiating elements. In the following section, a novel arraying technique extremely suitable for nantennas is presented and discussed. The calculated radiation efficiency of the single nano-rod is 52%. The only reason for losses in this nano-rod is the metallic losses. If silver is used instead of gold, the radiation efficiency is expected to increase, which will be shown in sections 5.2, and 5.3. Nevertheless, the disadvantage of using silver material is its tendency for oxidation, which is not the case for gold material.

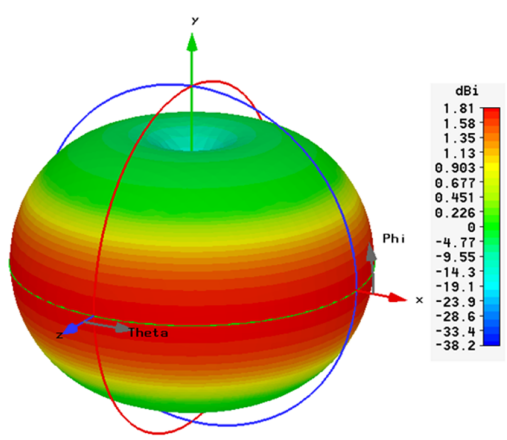

Figure 5.6: 3D directivity pattern of the 350 nm half-wavelength nano-rod calculated at 193.55 THz using CST.

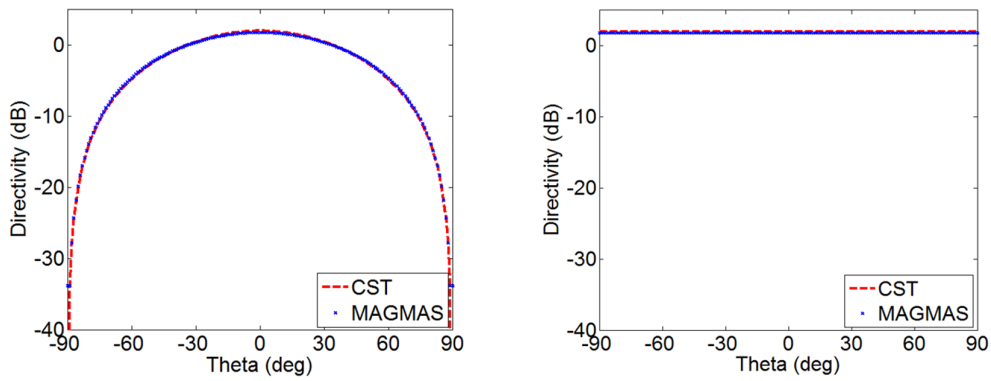

(a) (b)

Figure 5.7: Radiation patterns along the principal planes of the 350 nm half-wavelength nano-rod at 193.55 THz simulated using both CST and MAGMAS: (a) *E*-plane, and (b) *H*-plane.

5.1.2 Structure of the Wire-Grid Nano-Antenna Array

The proposed wire-grid nano-rod array is shown in Figure 5.8. This array consists of five vertical radiators and four horizontal connectors [98-99]. For maximum directivity, currents flowing along the radiators should be in phase such that their radiations add constructively. On the other hand, currents along the connectors have to be in opposite directions such that their radiations cancel out. This condition is achieved by making the electrical length of each radiator and connector equals $\lambda_g/2$ [100]. This way, the proposed wire-grid can be looked at as an array of five dipoles, which results in an array factor and enhanced directivity. As shown in Figure 5.8, the lengths of radiators and connectors are denoted by: L_{rad} and L_{con}, respectively. It is worth mentioning here that this wire-grid array does not require a ground metal plane below the wire network. This is mainly because of the fact that SPP waves can propagate through this network, where the fields of these waves are guided to the metal/free-space interfaces. This is the main difference between the proposed plasmonic wire-grid array and the microwave counterparts [101] in which slot lines and microstrip lines, respectively, are used to form the array. In the former case the electric field is guided between the two metals surrounding the slot, while in the later case the field is guided between the strip and the ground plane underneath.

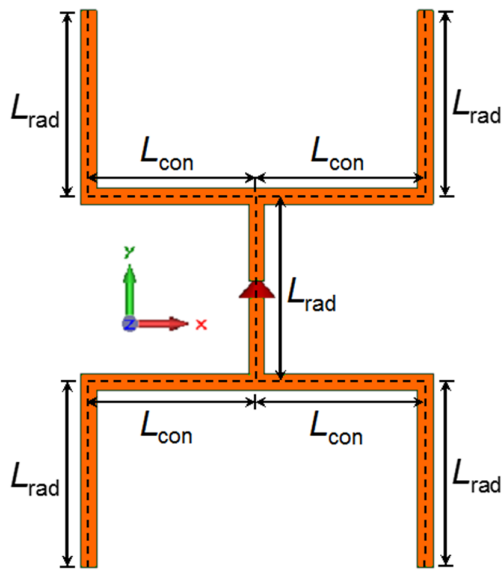

Figure 5.8: Structure of the wire-grid array of five nano-rods.

A directive beam can be achieved by optimizing the values of these two geometrical parameters for maximum directivity. The contour plot in Figure 5.9 illustrates how the directivity function is varying with L_{rad} and L_{con}. According to this figure and the parametric study that has been performed using CST, a maximum directivity of 9.25 dBi is obtained when L_{rad} = 350 nm and L_{con} = 325 nm. These values are very close to the predicted value of ($\lambda_g/2$) using field distribution. This electrical length forces the currents on the vertical rods to add constructively. The achieved value of directivity is much higher than that of a single rod with the same L_{rad} of 350 nm.

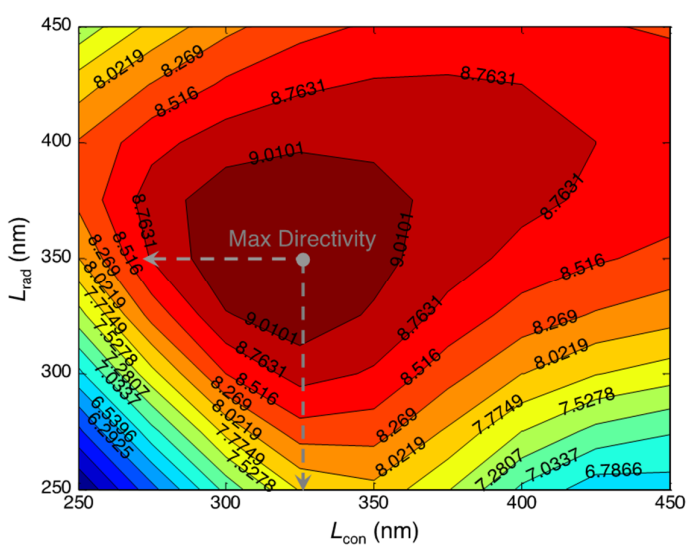

Figure 5.9: Directivity of the nano-wire-grid array versus L_{rad} and L_{con} calculated using CST at 193.55 THz.

5.1.3 Modal Field Distribution along the Wire-Grid Array

To illustrate the operation of the proposed optimal wire-grid nano array, the distribution of the *z*-component of the magnetic field in the *xy*-plane calculated using CST at 193.55 THz is shown in Figure 5.10. This component of the magnetic field is linked to the electric current flowing through the gold arms of the array, as illustrated in Figure 5.5. The half-wavelength field distribution terminated by two nulls can be clearly seen along the four outer vertical radiators. The direction of current along these elements is the same, which gives rise to an array factor. On the other hand, the field distribution along the horizontal connecting arms reveals that their currents are flowing in opposite directions, and hence no radiation is expected from these connectors. The field distribution along the central radiator does not follow the conventional half-wavelength pattern, and consequently its contribution to the radiation is less than that of the outer radiators.

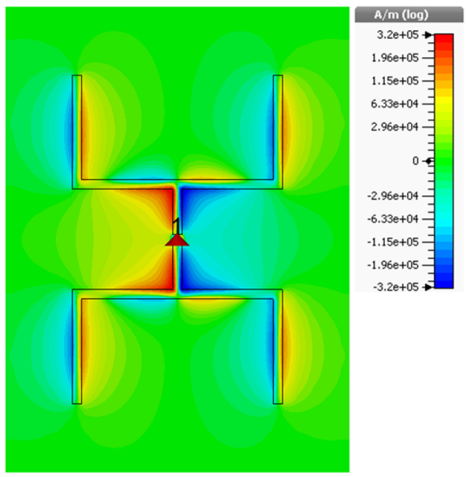

Figure 5.10: Distribution of H_z along the *xy*-plane of the optimal wire-grid array at 193.55 THz (log scale): L_{rad} = 350 nm, and L_{con} = 325 nm.

5.1.4 Radiation Characteristics of the Wire-Grid Array

The directivity pattern of the optimum wire-grid array is shown in Figure 5.11, as calculated using CST at 193.55 THz. Now, the beam is narrow and hence more suitable for point-to-point communication systems. The calculated directivity is 9.25 dBi, which is significantly higher than that of the single nano-rod. The radiation patterns along the *E*- and *H*-planes are shown in Figure 5.12, obtained using both CST and MAGMAS. The two simulators agree well with each other. The side-lobe-levels in the *E*- and *H*-planes are –2.5 dB and –10.2 dB, respectively. The level of the cross-polar components is zero in both principal planes, due to the perfect symmetry of the proposed structure around these planes. This symmetry leads to perfect cancellation of the radiation from the connectors' currents.

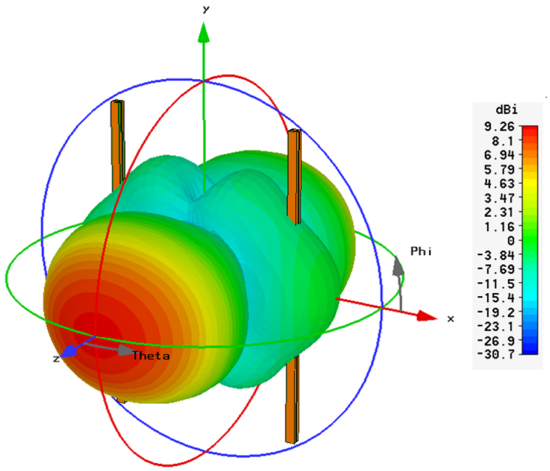

Figure 5.11: 3D directivity pattern of the proposed wire-grid array at 193.55 THz, L_{rad} = 350 nm and L_{con} = 325 nm, obtained using CST.

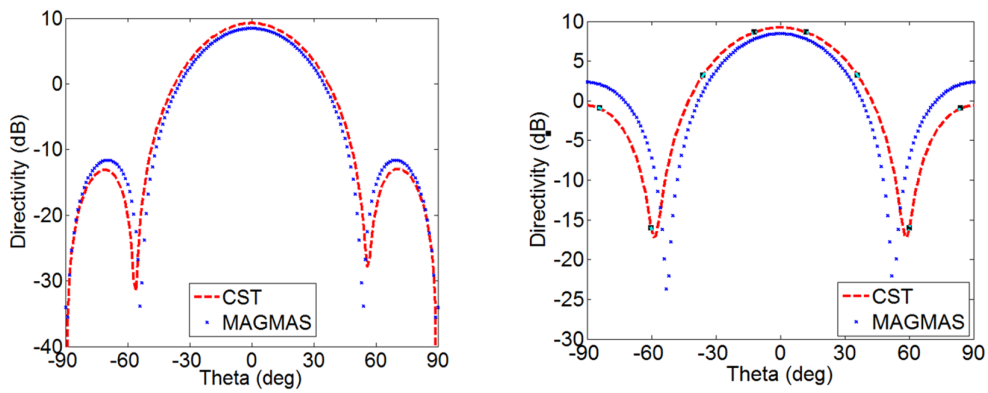

(a) (b)

Figure 5.12: Radiation patterns along the principal planes of the optimum wire-grid array at 193.55 THz simulated using both CST and MAGMAS: (a) *E*-plane, and (b) *H*-plane.

5.1.5 Effect of Adding a Substrate underneath the Wire-Grid Array

In this section, the effect of adding a substrate underneath the wire-grid nantenna array is studied. The substrate is assumed to cover the entire half-space below the nantenna. Figure 5.13 shows the radiation patterns of the wire-grid array in the *E*- and *H*-planes as simulated using MAGMAS for different values of the substrate's refractive index *n*: 1 (air), 1.5, and 2. As the substrate's refractive index increases, the front-to-back ratio decreases. This means more radiation in the substrate side compared to that in the air side. This is expected as the substrate has lower intrinsic wave impedance. Moreover, the pattern gets wider in the air side and narrower in the substrate side. Consequently, the side lobes disappear in the air side and their level increases in the substrate side, as the refractive index of the substrate increases. According to MAGMAS calculations, the directivity of the proposed wire-grid

nantenna array is 7.01, 10.56, and 15.24 dBi for n = 1, 1.5, and 2, respectively. The increase in the directivity value is due to the beam narrowing in the dominant radiation side, i.e. the substrate side.

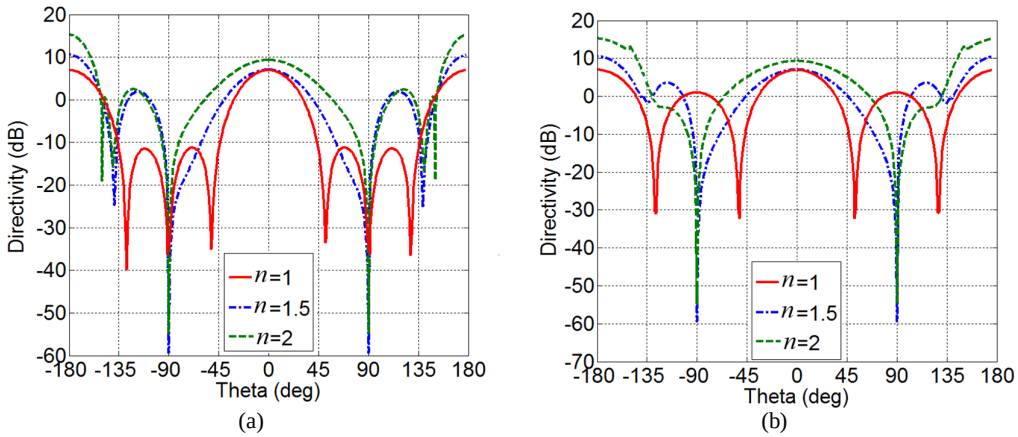

Figure 5.13: Radiation patterns along the principal planes of the optimum wire-grid array at 193.55 THz calculated using MAGMAS for different values of the substrate refractive index: (a) *E*-plane, and (b) *H*-plane.

5.2 Wire-Grid Nano-Antennas on Top of Finite SiO_2 Backed by Plasmonic Metal Layer

In this section, two wire-grid nano-antenna arrays are presented. These arrays are placed within a layered medium, which represents a practical case, unlike the previous section where the array is placed in a homogeneous medium (free-space). For this purpose, we start by the study of the single nano-dipole antenna which is the building block of the proposed arrays. The dipole consists of two silver $\lambda_g/4$ nano-rods. The width of the rod is denoted by W_{rad}, while its thickness is denoted by T_{rad}. The dipole is mounted on top of a finite SiO_2 substrate (thickness = T_{SiO2}) backed by a thick layer of silver (thickness = T_{Ag}). The nano-antenna is fed in between the two nano-rods, as shown in Figure 5.14. The analysis of the nano-dipole starts by studying the effect of varying the transversal rod dimensions on the guided wavelength and propagation loss of the corresponding infinitely long rod. For this task, the developed MoM solver is used to establish a starting point for estimating the dimensions of the $\lambda_g/2$ nano-rod. Afterwards, the optimization of the whole nano-antenna array is performed using CST, similar to the nano-antenna presented in section 5.1.

Using the developed solver, the nano-rod transmission line of width W_{line}, and thickness T_{line} is studied. Figure 5.15 shows the effect of varying W_{line} on the guided wavelength and propagation loss of the rod. The thicknesses of the SiO_2 layer and Ag ground plane are kept constant at T_{SiO2} = 150 nm, and T_{Ag} = 100 nm, respectively. The study of the plasmonic transmission line is also performed at 193.55 THz (1.55 µm), similar to the previous example as the antenna is designed for optical communication application. It is clear from Figure 5.15(a) that increasing the rod width leads to increasing the guided wavelength. When the width increases, the wave becomes less confined to the silver nano-rod. As a result, the wave possesses lower losses, as demonstrated in Figure 5.15(b). This means that

the wave propagation length inside the silver transmission line increases. It is worth mentioning that further increase of the width above a certain value (W_{line} = 90 nm in this case) has lower impact on the propagation characteristics of the nano-rod transmission line. The second parametric study shows the effect of varying the rod thickness, T_{line}. Two cases have been considered in this study: W_{line} = 30 nm and W_{line} = 90 nm, representing the minimum and maximum values considered for the width variation. Similar to the previous case, increasing the rod thickness leads to increasing the guided wavelength and decreasing the propagation loss, as shown in Figure 5.16.

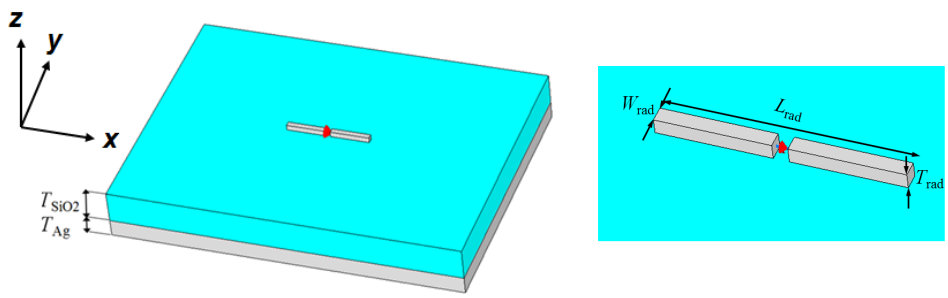

(a) (b)

Figure 5.14: Structure of the single nano-rod antenna on top of finite SiO_2 substrate backed by silver layer: (a) zoom-out, and (b) zoom-in.

It can be concluded from this study that for a $\lambda_g/2$ nano-dipole, if W_{line} = 30 nm (90 nm), the length of the rod should be 377 nm (443.5 nm) approximately. Therefore, wide nano-dipoles should be longer and have lower losses compared to thin dipoles. As a result, when designing a wire-grid nano-antenna array, one can control the distances between the array elements by varying the width or thickness of the plasmonic rods. In this work, the thickness of the nano-rods is kept constant at T_{line} = 30 nm, while the variation of the rod width is mainly chosen to control the array parameters, as will be shown in the following section.

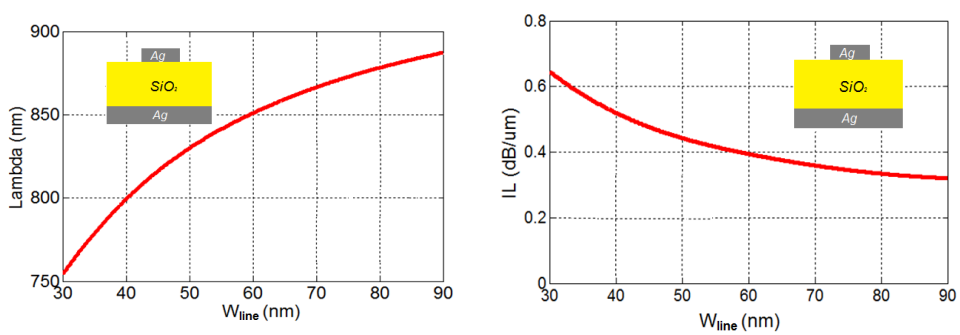

(a) (b)

Figure 5.15: Effect of varying the nano-rod width on: (a) guided wavelength, and (b) insertion loss. The thickness of the rod is kept constant at T_{line} = 30 nm, while the thickness of the SiO_2 layer is 150 nm.

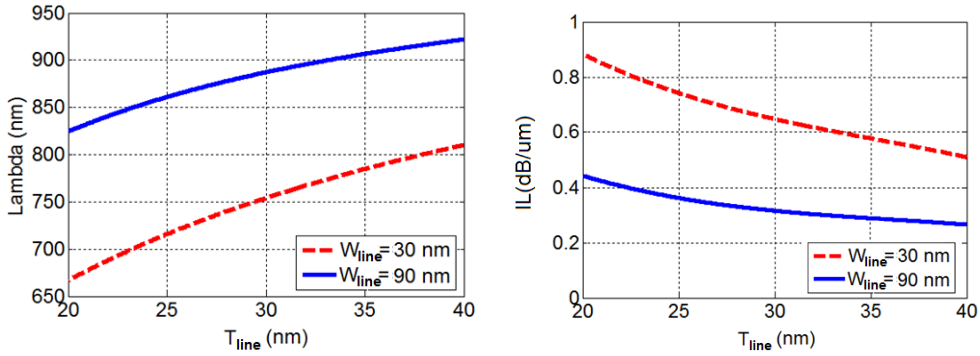

(a) (b)

Figure 5.16: Effect of varying the nano-rod thickness on: (a) guided wavelength, and (b) insertion loss. The width of the rod is either W_{line} = 30 nm or W_{line} = 90 nm, while the thickness of the SiO_2 layer is kept fixed at T_{SiO2} = 150 nm.

5.2.1 Single Nano-Dipole Antenna

After estimating the length of the $\lambda_g/2$ nano-dipole, the structure of the nano-dipole is simulated in CST for verification. The two cases: (W_{rad} = 30 nm, L_{rad} = 377 nm), and (W_{rad} = 90 nm, L_{rad} = 433.5 nm) are considered in this study. In both cases, the gap width is considered to be 30 nm and T_{SiO2} = 150 nm. Figure 5.17 shows the normal component of the magnetic field (H_z) at 193.55 THz. It is shown that the estimated dipole length using our developed solver gives the expected field distribution around the dipole where the field is maximum at the centre of the dipole, while it vanishes at the dipole edges. The 3D radiation patterns (directivity) of the nano-dipoles under investigation are shown in Figure 5.18. The antenna has a directivity, gain and radiation efficiency of 5.99 dBi (5.21 dBi), 4.88 dBi (4.71 dBi), and 77.63% (89.23%) respectively, for the narrow (wide) dipole at 193.55 THz. As expected, the narrower dipole has higher losses compared to the wide one, which is obvious from the radiation efficiency results. Figure 5.18 also shows that the nano-rod radiates only at the top side of the substrate. The presence of the bottom silver layer prevents backside radiation. This means that this structure as a whole can be placed above any substrate without affecting its radiation performance.

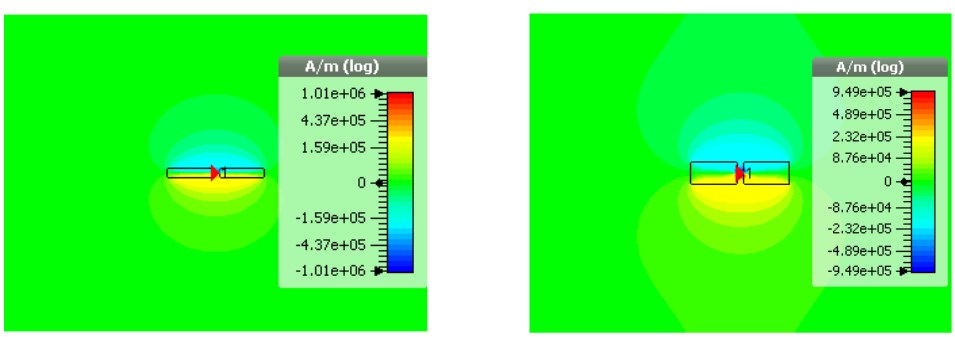

(a) (b)

Figure 5.17: Normal component of the magnetic field (H_z) along the *xy*-plane at T_{SiO2} = 150 nm: (a) W_{rad} = 30 nm, L_{rad} = 377 nm and (b) W_{rad} = 90 nm, L_{rad} = 433.5 nm (log scale).

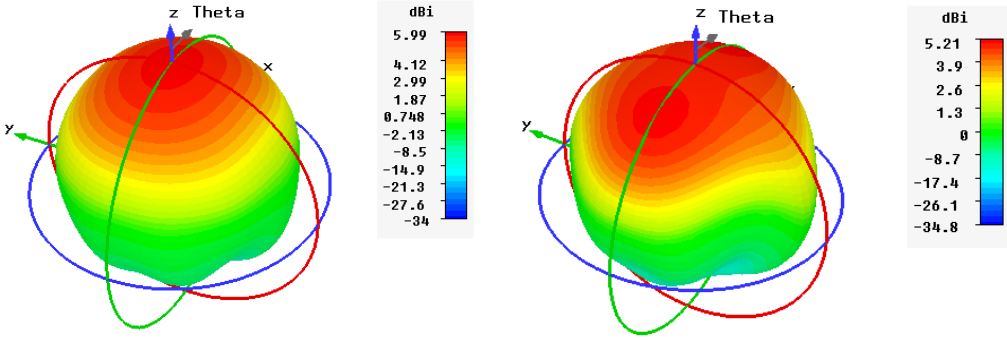

(a) (b)

Figure 5.18: 3D directivity patterns of the dipole antenna at T_{SiO2} = 150 nm: (a) W_{rad} = 30 nm, L_{rad} = 377 nm and (b) W_{rad} = 90 nm, L_{rad} = 433.5 nm.

5.2.2 Eleven-Element Wire-Grid Nano-Antenna Array

In this section, we introduce an array consisting of eleven nano-rods, shown in Figure 5.19, for the sake of enhancing the directivity. Similar to the five-elements wire-grid antenna presented in section 5.1.2, this array also consists of a number of horizontal radiators and vertical connectors, each of which has a length corresponding to half guided wavelength. Compared to the wire-grid array presented in section 5.1.2, this design is different in the following aspects:

1- The number of radiators is increased to eleven rods instead of five.

2- The radiators and connectors are constructed from Ag material rather than Au. This is due to the relatively lower losses of Ag compared to Au, which affects the radiation efficiency especially for larger arrays.

3- The whole array is placed on top of a finite thickness SiO_2 substrate backed by am Ag layer, which acts as a ground plane and prevents backward radiation. Consequently, the whole antenna structure can be placed above any substrate without affecting its performance. This is different from the antenna proposed in section 5.1 which is designed in free-space. Thus adding a substrate underneath the array plays a major role in determining the array radiation characteristics.

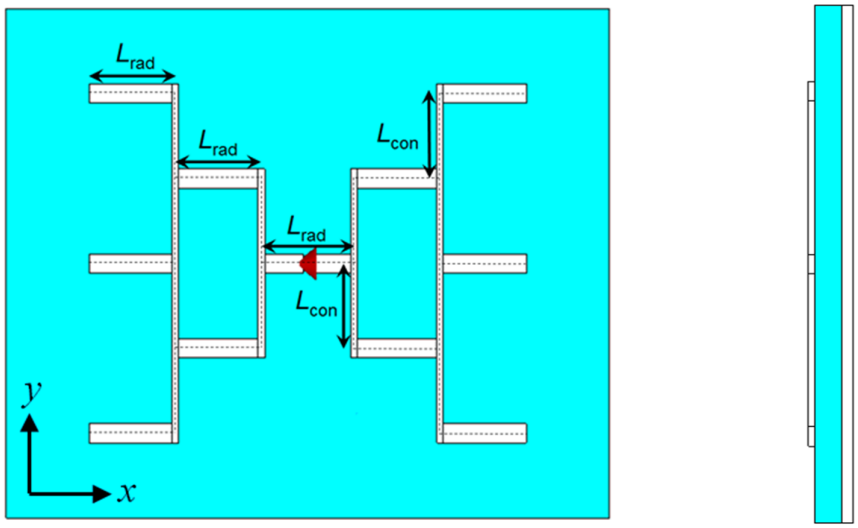

(a) (b)

Figure 5.19: Eleven-element wire-grid nano-antenna array placed on top of a finite SiO_2 substrate backed by Ag layer: (a) Top-view, and (b) Side-view.

5.2.2.1 Operation of the Wire-Grid Antenna Array

The operation of the array is similar to the five-element wire-grid array where the antenna is excited when a voltage difference is created between the two rods constructing the centred radiator. This causes current to flow along the connectors and radiators. As the lengths of the radiators and connectors are $\lambda_g/2$, currents along all radiators will be in-phase while currents along the connectors will be out-of-phase and cancel out. Compared to the five-element wire-grid array, this array provides higher directivity due to the increased number of radiators. It is worth mentioning that since plasmonic metals are lossy at optical frequencies, the current will fade as it propagates. This means that the outer radiators will suffer from lower current strengths compared to the centre and middle radiators.

5.2.2.2 Parametric Study of the 11-Elements Wire-Grid Array

In this section, the variation of the geometrical parameters of the eleven-element wire-grid nano-antenna array is studied. It is assumed that the radiators and connectors have the same lengths while their widths are different. The thickness of SiO_2 is fixed at T_{SiO2} = 100 nm. The array is optimized for maximum gain. The optimum geometrical parameters of the array are: L_{rad} = L_{con} = 395 nm, W_{rad} = 90 nm, and W_{con} = 30 nm. To show the effect of varying each of the antenna parameters, Table 5.1 presents a sensitivity analysis for the gain when the geometrical parameters are varied by 10% (increase) of their optimum values. Only one variation at a time is considered while the rest of parameters are kept at their optimum values. The table shows that the radiators' and connectors' lengths are the most effective parameters in determining the value of the gain. The other parameters, W_{rad} and W_{con} have much lower sensitivity compared to L_{rad} and L_{con}.

Table 5.1: Sensitivity of the antenna array gain (at 193.55 THz) to 10% perturbation of its geometrical dimensions

Geometrical Parameter	Gain Sensitivity (dB/10% perturbation)
L_{rad} (L_{con})	**–0.88**
W_{rad}	–0.04
W_{con}	–0.04

To illustrate the effect of varying the lengths of the radiators and connectors, Figure 5.21 shows the normal component of the magnetic field (H_z) along the *xy*-plane at: $L_{rad} = L_{con}$ = 370 nm, and $L_{rad} = L_{con}$ = 420 nm. Figure 5.20(a) shows that at $L_{rad} = L_{con}$ = 370 nm, the current along the outer radiators are in-phase. On the other hand, the centre radiator behaves as a short dipole which is due to the relatively small lengths of the radiators and connectors with respect to the resonance frequency. Thus, the radiation of the array at 193.55 THz is mainly resulting from the outer radiators. Figure 5.20(b) shows the 3D radiation pattern (directivity) of the array at $L_{rad} = L_{con}$ = 370 nm. The figure demonstrates the presence of side lobes along the *xz*-plane which can be due to the relatively large horizontal distance between the array elements since the centred radiator has weak contribution to the array's radiation.

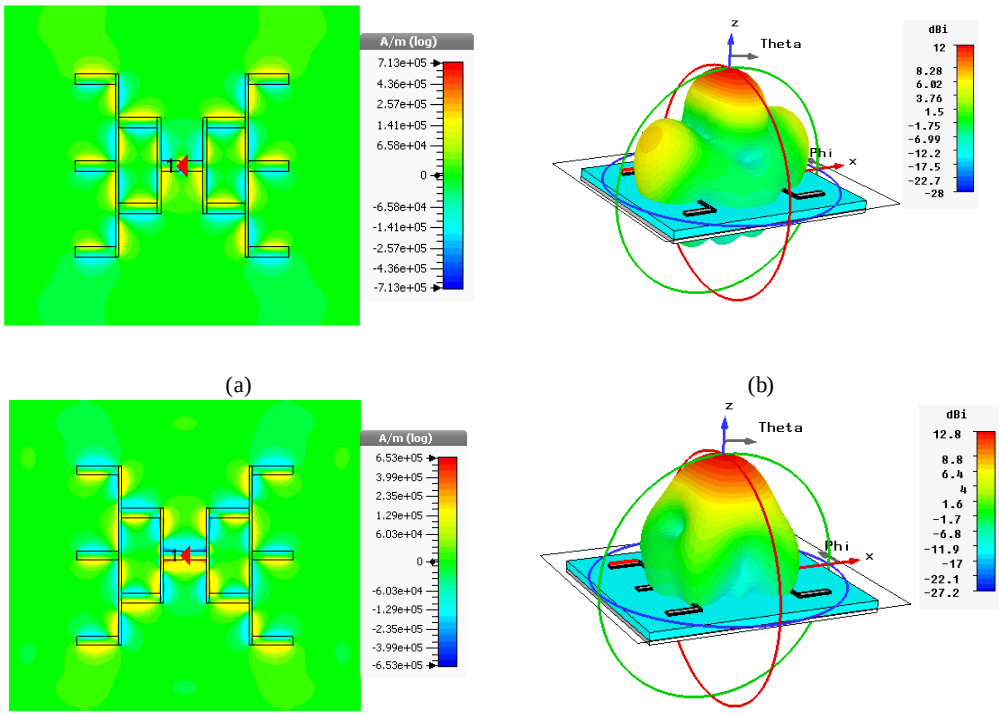

(a) (b)

(c) (d)

Figure 5.20: Normal magnetic field component (H_z) along the *xy*-plane and the corresponding 3D directivity radiation pattern for the wire-grid array at 193.55 THz: (a) H_z at $L_{rad} = L_{con}$ = 370 nm (log scale), (b) directivity at $L_{rad} = L_{con}$ = 370 nm, (c) H_z at $L_{rad} = L_{con}$ = 420 nm (log scale), (d) directivity at $L_{rad} = L_{con}$ = 420 nm.

At $L_{rad} = L_{con} = 420$ nm, it is clear that the normal magnetic field components are in-phase, as shown in Figure 5.20(c). Meanwhile, the lengths of the rods are slightly bigger than half the guided wavelength which is obvious from the field distribution. Figure 5.20(d) shows the directivity of the array. The figure shows a directive beam along the broadside direction, as desired, while there are almost no side-lobes. It is worth noting that this antenna does not radiate at the bottom side, due to the presence of the silver ground plane.

5.2.2.3 Characteristics of the Optimum 11-Elements Wire-Grid Array

Similar to the five-element wire-grid array presented in section 5.1, the proposed wire-grid array is also is designed to operate at the optical communication range with central frequency of 193.55 THz. At this frequency, the normal magnetic field component, H_z, is shown in Figure 5.21(a) for the optimum case where $L_{rad} = L_{con} = 395$ nm. Obviously from the figure, the field distributions along all radiators are in-phase. The 3D radiation pattern of the array antenna at 193.55 THz is shown in Figure 5.21(b). The antenna radiates in the broadside with no back-side radiation, as expected. The simulated directivity, gain, and radiation efficiency are 13 dBi, 12.2 dBi, and 78.2% respectively at 193.55 THz.

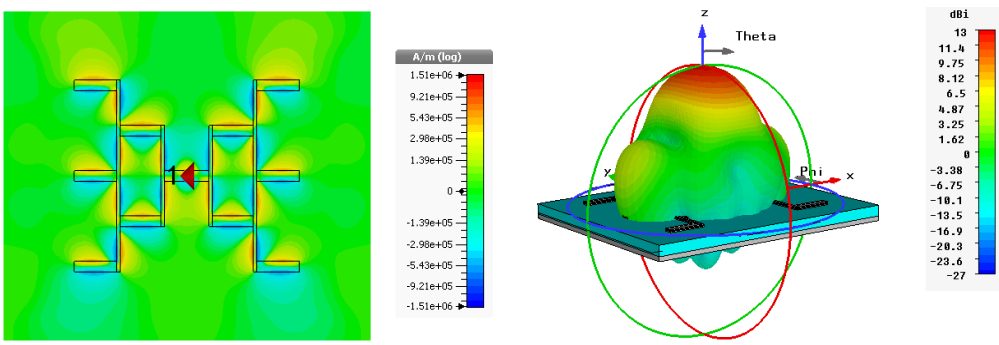

(a) (b)

Figure 5.21: (a) Normal component of the magnetic field (H_z) at 193.55 THz (log scale), and (b) the directivity of the optimum 11-elements wire-grid nano-antenna array at 193.55 THz for the optimum 11-element wire-grid array where $L_{rad} = L_{con} = 395$ nm.

The 2D radiation pattern of the proposed array is shown in Figure 5.22 along both the *E*- and *H*-planes. The antenna has a directive radiation toward the broadside especially along the *E*-plane (*xz*-plane) where the simulated beam width is 28.8°. On the other hand, the beam width along the *H*-plane (*yz*-plane) of the antenna is 40.2°. It is worth noting that the beam is narrower along the *E*-plane due to the non-uniform arrangement of the array elements along the *xy*-plane. As can be seen from Figure 5.19, there are more radiators along the *E*-plane compared to the *H*-plane leading to a narrower beam along the *E*-plane. The cross-polar component along the *E*- and *H*- planes are almost zero due to the perfect cancellation for the currents along the connectors at these planes.

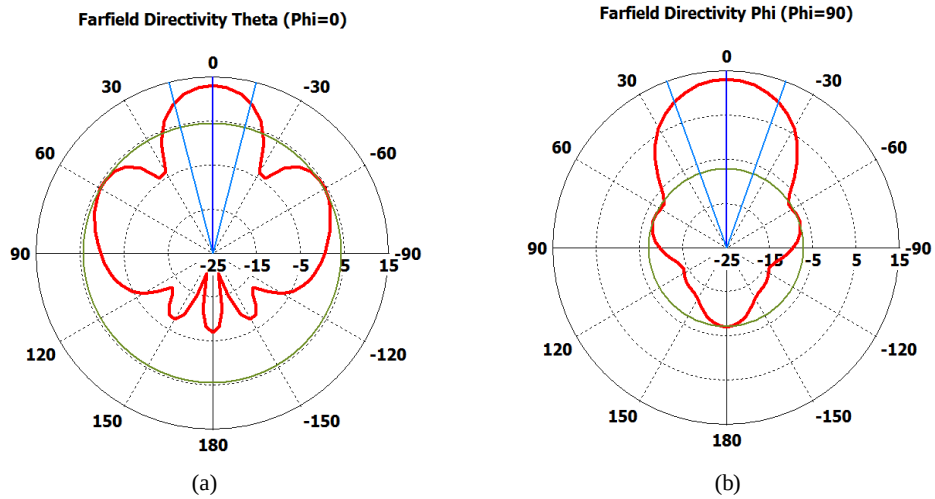

Figure 5.22: 2D radiation patterns of the optimum 11-elements wire-grid nano-antenna array at 193.55 THz (a) *E*-plane (Phi = 0°), and (b) *H*-plane (Phi = 90°).

5.2.3 Circularly Polarized Wire-Grid Nano-Antenna Array

The nano-dipole investigated in section 5.2 is now used again as the basic element for the circularly polarized nano-antenna array. Although the nano-dipole provides linear polarization, one is able to construct a circularly polarized array, as will be discussed in this section. As shown in Figure 5.23, the proposed circularly polarized wire-grid array is constructed from four sub-arrays forming an angle of 45˚, 135˚, 225˚, and 315˚ with the horizontal axis. Each sub-array consists of three radiators connected via non-radiating connectors. All connectors have the same length, L_{con}, and width, W_{con}. On the other hand, the lengths of the inner radiators (L_{rin1}, L_{rin2}) are different from the length of the outer ones (L_{rout}). The whole antenna structure is placed on top of a SiO_2 layer of thickness T_{SiO2} =150 nm that is backed by a thick layer of silver (T_{Ag} = 100 nm) to prevent backside radiation.

The proposed structure can be viewed as two orthogonal groups of antennas each consisting of six radiators parallel to each other and connected via narrow connectors. To differentiate between them, groups 1 and 2 are marked with different colours, see Figure 5.23, where the yellow (white) colour corresponds to group 1 (group 2). With this configuration, the first condition for a circularly polarized antenna is achieved, which is to have two orthogonal polarizations. The second essential condition for obtaining a circularly polarized radiation is to have a 90˚ phase difference between these two orthogonal polarizations. This is achieved by breaking the similarity between the two antenna groups by inserting a gap of length "*S*" along the inner radiators of one of these groups. The gap length is defined by $S = L_{rin1} - L_{rin2} - W_{rad}$. This gap acts as a capacitance which provides the required phase difference if its dimensions are well adjusted [102, and 103]. Since the two orthogonal arrays are similar, the electric field along them is almost the same. Circular polarization is achieved with this nano-antenna array.

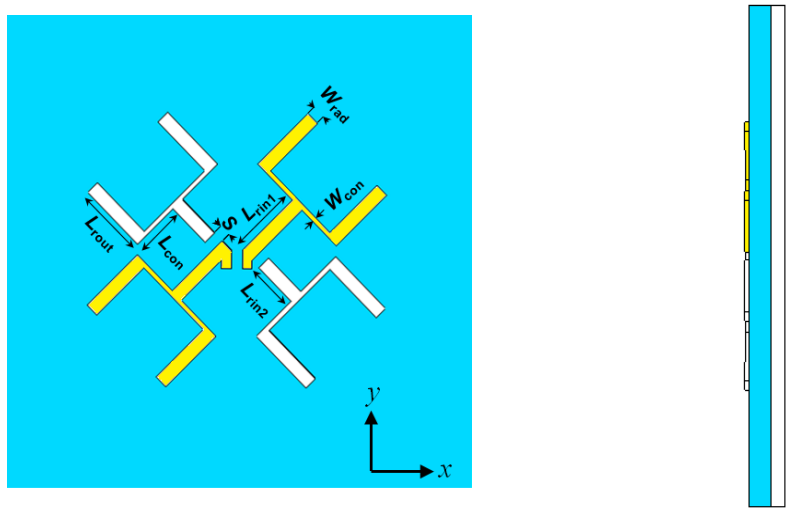

(a) (b)

Figure 5.23: Structure of the proposed circularly polarized wire-grid nano-antenna array: (a) top-view, and (b) side-view.

As shown in Figure 5.23, the outer radiators of both antenna groups have the same dimensions. Their lengths and widths are denoted by L_{rout} and W_{rad}, respectively. The inner radiators of the two groups have different lengths (L_{rin1} and L_{rin2}) but their width is the same and equals that of the outer radiators (i.e. W_{rad}). All radiators and connectors are made of Ag of 30 nm thickness. A short "coupled strips (CPS) transmission line" is directly connected to the inner radiators of group 1. The inner radiators of group 2 are excited via electromagnetic coupling through the capacitive gap introduced between them.

In order to obtain constructive interference along the broadside direction, the polarization current, i.e. the longitudinal electric field, along the radiators should be in-phase while the currents along the perpendicular connectors should be out-of-phase. To reach these two conditions simultaneously, the length of the radiators and connectors should be $\lambda_g/2$, similar to the previously studied arrays. It is worth mentioning that for the proposed array, the inner radiators should be long enough while the length of the connectors should be relatively shorter. This is essential in order to avoid any overlapping between the radiators and connectors of the four sub-arrays. In section 5.2, it is demonstrated that wide nano-rods have longer wavelengths compared to narrow ones. Therefore, the radiators should be wider than the connectors to obtain relatively long (short) radiators (connectors) in order to maintain the distance between the sub-arrays.

The antenna operates when the differential mode of the CPS transmission line is excited creating polarization currents along the radiators of group 1. As the length of the radiators and connectors is $\lambda_g/2$, the currents along the radiators are in phase while those along the connectors are out-of-phase. For group 2, the radiators are not directly excited. Nevertheless, electromagnetic coupling takes place through the gap, leading to indirect excitation. Similar to group 1, the currents along its radiators (connectors) are in- (out-of-) phase. The presence of the gap introduces a phase difference between the two groups of

radiators. By adjusting the gap size, a phase difference of 90˚ can be obtained. Consequently, circularly polarized radiation is achieved. Figure 5.24 shows the normal component of the magnetic field (H_z) along the *xy*-plane at 193.55 THz at two different times: $t = 0$ and $t = T/4$, where T is the time of one cycle, which equals 5.166 fs. As shown in the figure, at $t = 0$, H_z is maximized along the radiators of group 1 while it is minimized along group 2. The opposite happens at $t = T/4$.

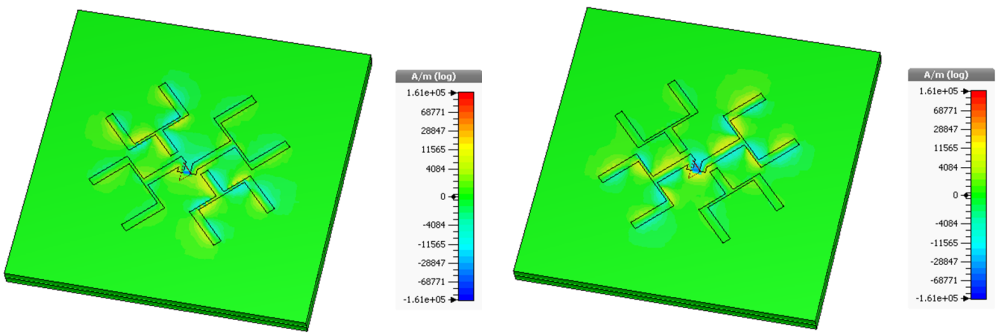

(a) (b)

Figure 5.24: Normal component of the magnetic field (H_z) for the optimized circularly polarized nano wire-grid antenna array at 193.55 THz: (a) $t = 0$, and (b) $t = T/4$ (log scale).

5.2.3.1 Parametric Study of the Circularly Polarized Wire-Grid Array

In this section, the effect of varying the antenna geometrical parameters on the axial ratio and gain is studied at 193.55 THz. In order to determine the most effective parameters, a sensitivity analysis is first performed. All the parameters: L_{rin1}, L_{rin2}, L_{rout}, W_{rad}, L_{con}, and W_{con}, are considered in this study. The list of the optimized antenna parameters is shown in Table 5.2, while in Tables 5.3 and 5.4 the sensitivity analysis is presented. These tables show the variation in dB of the antenna's Axial Ratio (A.R.) and gain when each parameter is deviated (increased) by 5% from its optimum value. The other parameters are kept at their optimum values. The table shows that even small variations of the array parameters have a strong impact on its radiation characteristics. Specifically, the lengths of the inner radiators (L_{rin1}, L_{rin2},) have the strongest impact on the axial ratio and gain of the array. As L_{rin2} increases, S decreases, leading to increasing the capacitance between the inner radiators of group 2 and the feeding CPS lines. As a result, the phase difference between the two arrays is altered. Therefore, the axial ratio increases. On the other hand, when L_{rin1} increases, the distance between the outer radiators increases, which leads to decreasing the coupling between the outer radiators and the connectors. Consequently, the axial ratio is affected.

Table 5.2: Optimum dimensions of the circularly polarized nano wire-grid antenna array

Geometrical Parameter	Value	Geometrical Parameter	Value
L_{con}	330 nm	W_{con}	30 nm
L_{rin1}	460 nm	W_{rad}	90 nm
L_{rin2}	285 nm	L_{rout}	485 nm

Table 5.3: Sensitivity of the axial ratio of the antenna array to 5% perturbation of the array geometrical dimensions

Geometrical Parameter	Axial Ratio Sensitivity (dB/5% perturbation)	Geometrical Parameter	Axial Ratio Sensitivity (dB/5% perturbation)
L_{con}	0.47	W_{con}	2.23
L_{rin1}	**3.07**	W_{rad}	2.36
L_{rin2}	**4.12**	L_{rout}	1.90

Table 5.4: Sensitivity of the gain of the antenna array to 5% perturbation of the array geometrical dimensions

Geometrical Parameter	Gain Sensitivity (dB/5% perturbation)	Geometrical Parameter	Gain Sensitivity (dB/5% perturbation)
L_{con}	+0.05	W_{con}	–0.18
L_{rin1}	**–0.57**	W_{rad}	–0.43
L_{rin2}	**–0.97**	L_{rout}	–0.01

Figure 5.25 shows a contour plot of the axial ratio when both L_{rin1}, and L_{rin2} are varied. Clearly, the minimum axial ratio is obtained at L_{rin1} = 415 nm and L_{rin2} = 285 nm. If the length of the inner radiator L_{rin1} is increased (decreased), this has to be compensated by an increase (decrease) of L_{rin2} to obtain a low axial ratio.

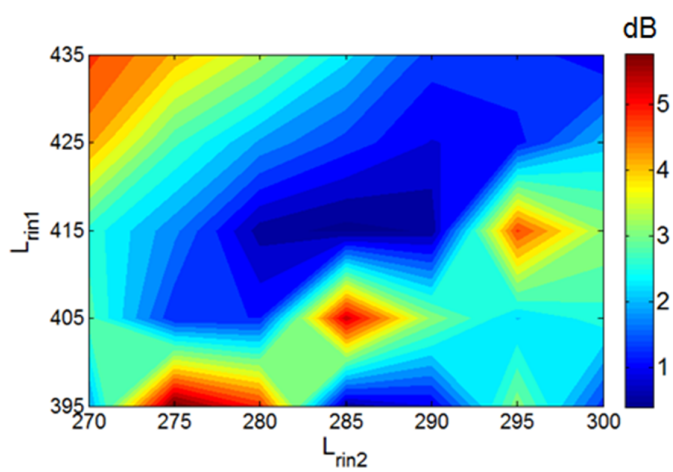

Figure 5.25: Contour plot showing the axial ratio of the circularly polarized wire-grid nano-antenna array versus the lengths of the inner radiators L_{rin1} and L_{rin2}.

5.2.3.2 Characteristics of the Optimum Wire-Grid Nano-Antenna Array

The 3D radiation pattern of the optimized nano wire-grid antenna array is shown in Figure 5.26 as simulated by CST at 193.55 THz (1.55 µm). The array has a directive beam in the broadside direction and negligible backside radiation due to the presence of the silver layer underneath the substrate. The array has a directivity, gain, and radiation efficiency of 10.8 dBi, 10.01 dBi, and 82.75% at 193.55 THz. The 2D radiation patterns are shown in Figure 5.27 at Phi = 0˚, and Phi = 90˚. It is clear that the antenna has right-hand circular polarization radiation. Additionally, the antenna is characterized by its high polarization purity in both principal planes. The cross-polarization level at broadside is –32.87 dB whereas the maximum cross-polarization level along the Phi = 0˚ (Phi = 90˚) plane is –12.12 dB (–16.52 dB). The axial ratio of the antenna versus frequency is plotted in Figure 5.28. The plot shows that the array has very low axial ratio at 193.55 THz (A.R. = 0.39 dB). Additionally, the array provides a wide axial-ratio bandwidth which extends from 188.2 THz till 197.8 THz (4.95%). Over this range, the array has a directivity, gain and radiation efficiency of about 10.75 dB, 9.75 dBi, and 79%, respectively, with little variations around these values, as shown in Figure 5.29.

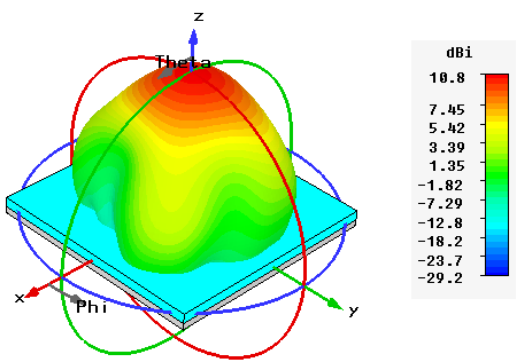

Figure 5.26: 3D radiation pattern of the optimum circularly polarized nano wire-grid antenna array at 193.55 THz.

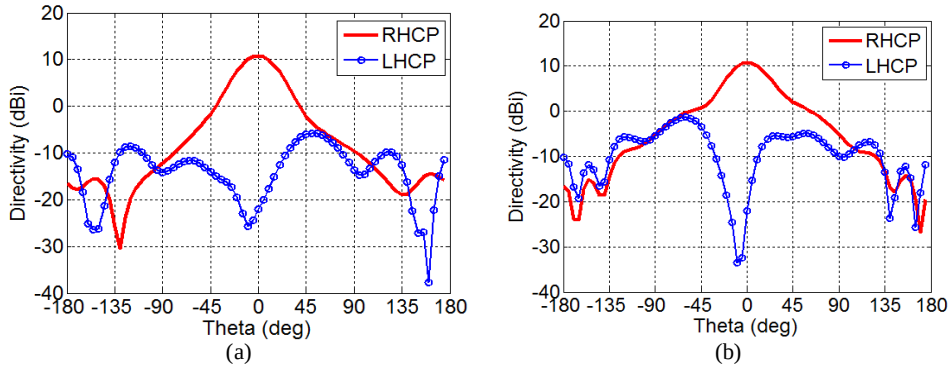

Figure 5.27: 2D radiations pattern of the optimum circularly polarized nano wire-grid antenna array at 193.55 THz (a) Phi = 0˚, and (b) Phi = 90˚.

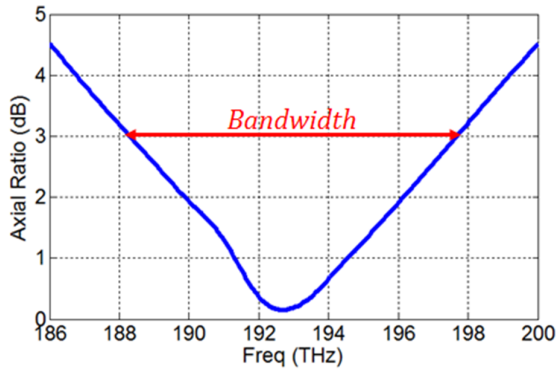

Figure 5.28: Axial Ratio versus frequency of the optimum circularly polarized nano wire-grid antenna array.

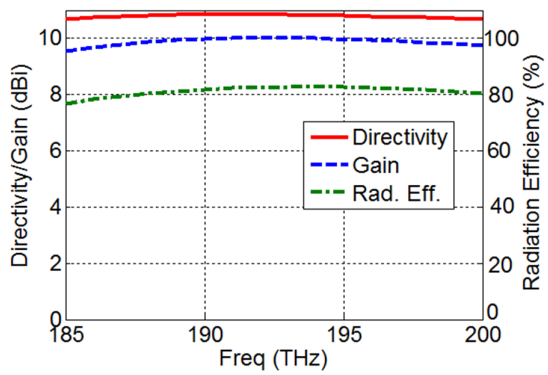

Figure 5.29: Variation of the directivity, gain and radiation efficiency of the optimum circularly polarized nano wire-grid antenna array versus frequency.

It is worth noting that the proposed nano-antenna can be used in the receiving mode where it converts the electromagnetic waves in free-space into localized field. In such case, the nano-antenna has the advantage of being insensitive to the polarization of the incident electromagnetic wave.

5.3 Fabrication and Measurements

This section presents the results of the fabricated wire-grid nano-antenna arrays. Two array versions are considered for this study; the five-element, and the eleven-element wire-grid arrays, shown in Figure 5.30. As shown, the middle radiators of these arrays are different from those presented in sections 5.1 and 5.2, since they do not include an inner gap. The reason behind this difference is that the fabricated arrays will be excited not via a voltage difference at the antenna gap, but via an incident plane wave. The dimensions of the fabricated antennas are given by: L_1 = 165 nm, L_2 = 145 nm, W_1 = 90 nm, and W_2 = 60 nm. These dimensions are chosen for the array designed to operate at 400 THz. The fabrication of the antenna is performed using electron beam lithography (20 kV, ZEP-resist), evaporation of Au, and subsequent lift-off at 30 nm. The antennas are characterized by

measuring their transmittance. Thus, in order to obtain reasonable signal strength all over the spectrum of interest, it is necessary to fabricate many arrays in a periodic configuration. In our case, the array is designed with pitch length of 1.75 µm. This distance is large enough to ensure that there is no coupling between the arrays. Figure 5.31 shows the SEM photos of the fabricated arrays. It is clear that the fabricated structures have round corners, unlike the designed rectangular ones. Additionally, the dimensions of the rods are slightly different than the design.

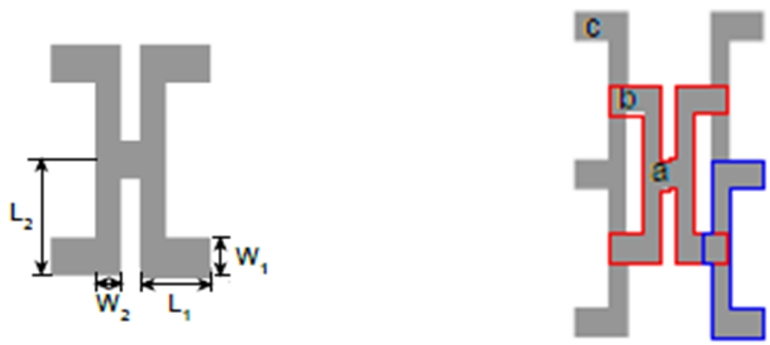

(a) (b)

Figure 5.30: Structure of the wire-grid nano-antenna arrays: (a) five-elements, and (b) eleven-elements.

(a) (b)

Figure 5.31: SEM photos for the fabricated wire-grid nano-antenna arrays: (a) five-elements, and (b) eleven-elements.

The characterization of the arrays is made by measuring the transmittance over the range extending from 50 THz up to 500 THz with transceiver polarization parallel to the radiators. Using the measured transmittance, the extinction cross-section can be obtained using the following equation:

$$\sigma_{ext}(f) = \left(1 - \frac{T(f)}{T_{ref}(f)}\right) A_{cell} \tag{5.1}$$

where $\sigma_{ext}(f)$ is the extinction cross-section, $T(f)$ is the transmittance of the array, $T_{ref}(f)$ is the transmittance of the substrate without the presence of the array, and A_{cell} is the area of the unit cell which in this case equals 3.1 μm^2. Figure 5.32 shows the measured and simulated extinction cross-section along the frequency spectrum (50 THz – 500 THz). It is clear that the measurements and simulations predict the locations of the peaks with little shift and disagreement in the values which can be attributed to the slightly different geometrical shape of the fabricated arrays compared to the designed ones. For the five-element array, simulations show four peaks centred around 96 THz, 274 THz, 358 THz, and 436 THz. On the other hand, measurements only show the presence of three peaks. For the eleven-element wire-grid array, both simulations and measurements show four peaks. Simulations show that these peaks occur at 60 THz, 180 THz, 264 THz, and 374 THz.

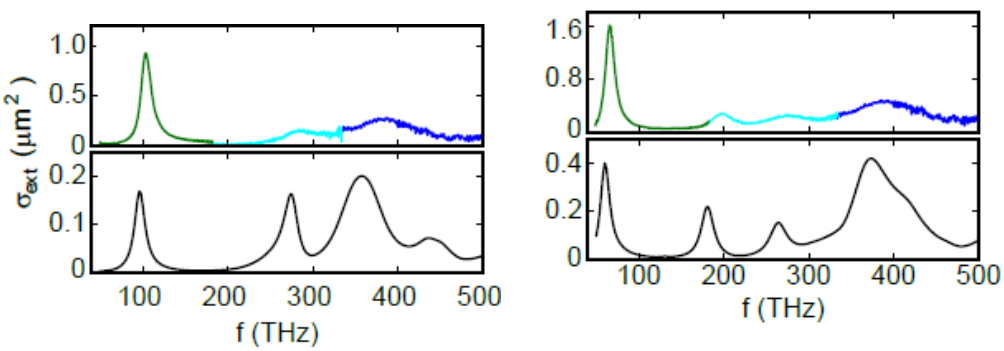

(a) (b)

Figure 5.32: Measured (coloured) versus simulated extinction cross-section for the wire-grid arrays: (a) five-elements, and (b) eleven-elements.

In order to understand the origin of the measured peaks, the modal current distribution along the plasmonic rods is simulated using a finite element method. The modal current distribution is calculated at frequencies where the extinction cross-section shows peaks. The mode is denoted by (*n*-*m*), where *n* =1 (*n*=2) for the five- (eleven-) element wire-grid array, and *m* corresponds to the mth resonance. The excitation of the antenna is achieved by assuming a plane-wave polarized along the direction of the radiators and propagating perpendicular to the plane of the array. The simulated current distribution of the five-element wire-grid array is presented in Figure 5.33. It shows that at 96 THz, the radiation is mainly resulting from the centre radiator, since the lengths of the radiators is much less than $\lambda_g/2$. At 274 THz, the radiators' and connectors' lengths are still below $\lambda_g/2$, leading to the opposite current for the middle radiator compared to the outer ones. At 358 THz, and 436 THz, currents along all radiators are in-phase. However, at 436 THz, the connectors have stronger currents compared to that at 358 THz.

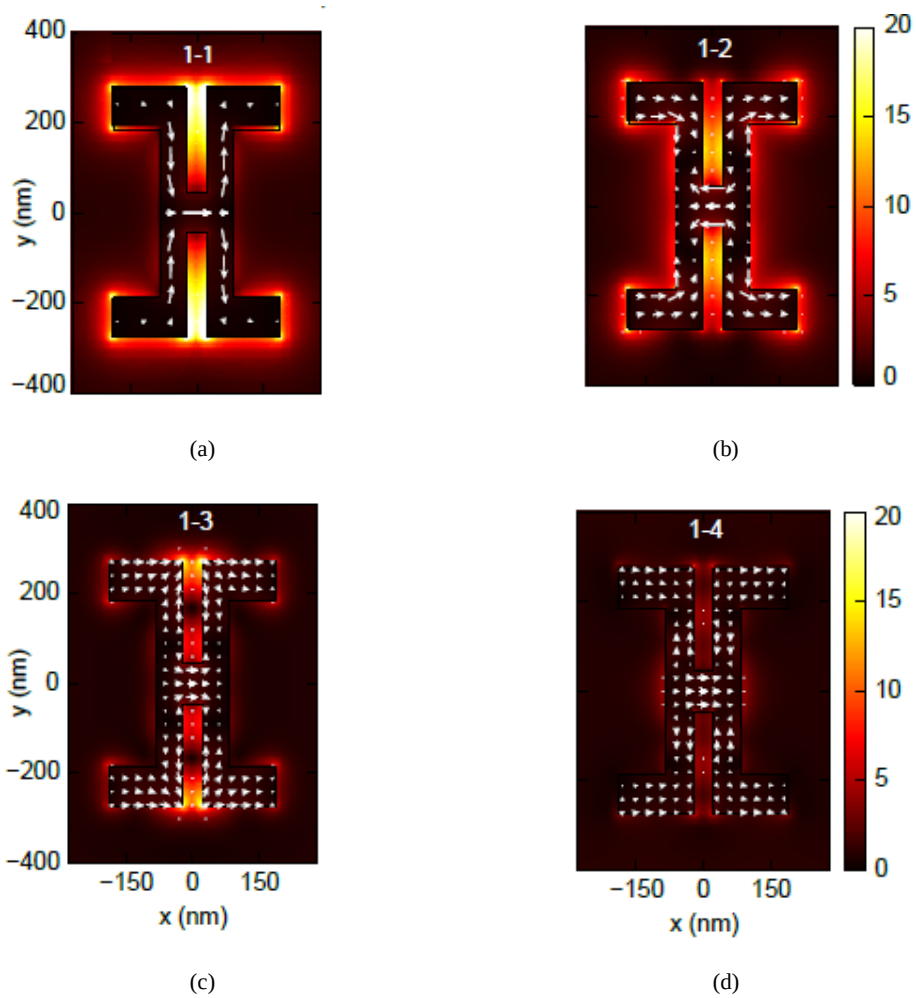

Figure 5.33: Modal current distribution along the five-element wire-grid array at (a) 96 THz, (b) 274 THz, (c) 358 THz, and (d) 436 THz.

In a similar way, one can explain the modal current distribution along the eleven-element wire-grid array, which is shown in Figure 5.34. At 60 THz, 180 THz, and 264 THz, the radiators' and connectors' lengths are less than $\lambda_g/2$. Therefore, the currents along the radiators are not all in-phase. For mode (2–1), the centred radiator is considered the main radiator. As for mode (2–2), currents along both the outer and middle radiators are in-phase while that along the centred radiator is out-of-phase. For mode (2–3), the currents along the outer and centred radiators are in-phase while that along middle radiators are out-of-phase. At 374 THz, mode (2–4), all radiators' currents are in-phase. This demonstrates that their dimensions correspond to $\lambda_g/2$.

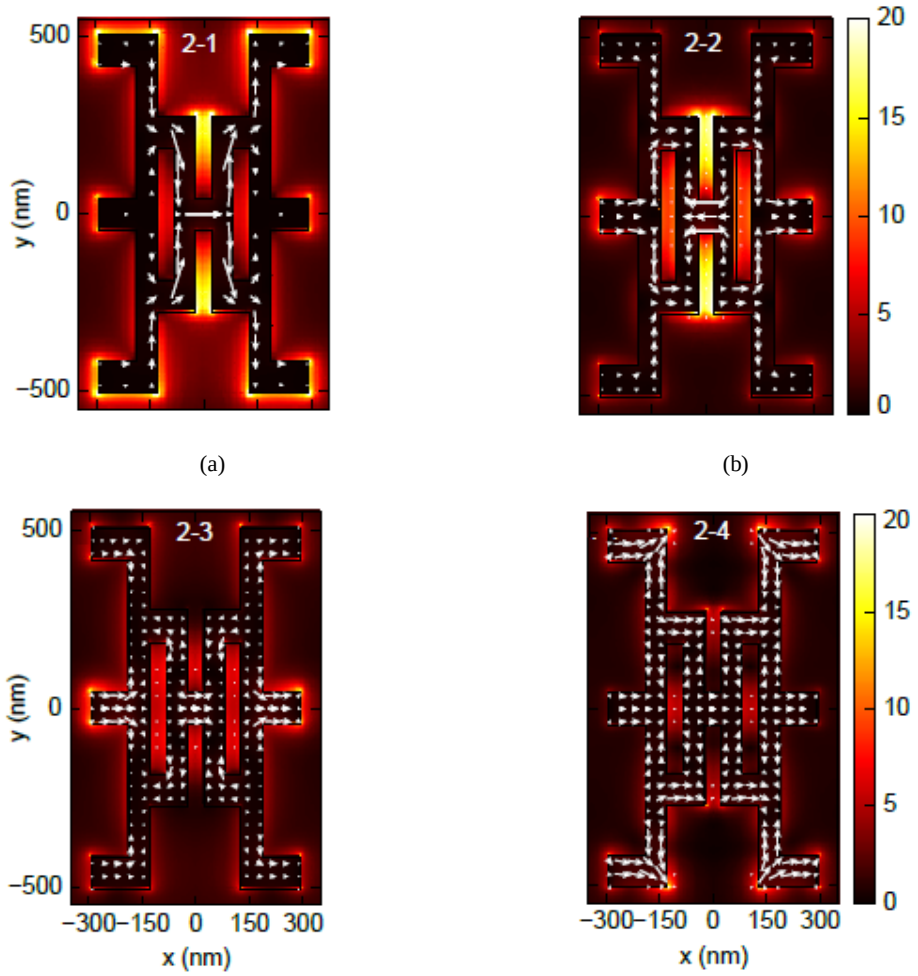

(a) (b)

(c) (d)

Figure 5.34: Modal current distribution along the eleven-element wire-grid array at: (a) 60 THz, (b) 180 THz, (c) 264 THz, and (d) 374 THz.

5.4 Conclusions

This chapter presents a number of wire-grid nano-antenna arrays designed for optical communication applications. The basic element of these arrays is a nano-dipole, i.e. a nano-rod, which can be seen as a finite plasmonic transmission line. Therefore, the initial dimensions of the proposed wire-grid nano-antennas can be determined using the developed mode solver where the guided wavelength and the losses are estimated. The chapter starts by presenting a five-element wire-grid array located in free-space. The antenna is optimized for maximum directivity which reaches 9.25 dBi. Since there is no substrate underneath the antenna, the radiation is symmetric in the direction normal to the array's plane. For this design Au is used to construct the antenna which is lossy leading to a radiation efficiency of 52% at the desired frequency (193.55 THz). The second design aims at increasing the gain

of the antenna, so it is important to enhance the radiation efficiency, which is achieved by using Ag material instead of Au due to its relatively lower losses at 193.55 THz. Additionally, for this design the number of radiators are increased to eleven rods instead of five in order to increase the directivity of the antenna. The antenna is optimized for maximum gain and the chosen bandwidth is around the 193.55 THz frequency. Moreover, a substrate is added for the design to be practical. A ground plane is placed on the top of the substrate and below the wire-grid antenna array in order to prevent the radiation from the backside leading to an increase in the directivity. Both the aforementioned arrays provide linear polarization since all rods have the same orientation. In order to obtain a circular polarization, a novel wire-grid array constructed from twelve rods is presented. Each six rods have the same orientation and the two groups of radiators are placed orthogonal to each other. Furthermore, a 90˚ phase shift is introduced between the excitation of the two groups of wire-grids so that the whole array is capable of radiating circular polarization. The optimized antenna provides a high directivity (10.75 dBi), gain (9.75 dBi) and a relatively wide axial-ratio bandwidth of 9.6 THz. The last section in this chapter presents two fabricated nano-antenna prototypes which are designed for operation at 400 THz. The arrays are characterized where the transmission of a periodic array of wire-grids illuminated by a plane wave is measured and compared with the simulated transmission. Both data shows good agreement except for the presence of a small frequency shift and some variations for the amplitude which can be due to the difference in the dimensions of the fabricated prototypes compared to the simulated design.

Chapter 6: Conclusions and Future Work

6.1 Summary of the Thesis

Plasmonics received great attention due to their superior capability of squeezing light beyond the diffraction limit. Thus, their dimensions are much smaller compared to photonic devices. This important characteristic enabled bridging the size gap between electronic and photonic devices. The term *"plasmonics"* refer to the characteristics of some metals (e.g. gold, silver, copper, and aluminium) at the terahertz (THz) and infrared range in which metals behave like lossy dielectric medium whose electric characteristics are described by complex and dispersive dielectric permittivity. Consequently, plasmonic metals are different from classical ones which are characterized by their very high conductivity, i.e. losses. The dimensions of plasmonic devices are in the range of nano-meters, which is comparable to the skin depth of plasmonic metals. As a result, current is allowed to flow inside the volume of these devices, unlike classical metals whose currents can only flow along their surface. Therefore, when designing plasmonic devices, these differences must be taken into consideration to obtain accurate results. Most importantly, the meshing technique considered should be volumetric to account for the volumetric current. In this thesis, we are concerned with the development of a plasmonic transmission line mode solver which calculates the propagation characteristics and the modal current distributions of plasmonic

transmission lines. The thesis also introduces a number of novel plasmonic wire-grid nano-antenna arrays designed for optical communication applications where they can be used for inter-/intra-chip communication in which they replace the lossy transmission lines. The proposed nano-antenna arrays are characterized by their high directivity making them suitable for point-to-point optical communication.

In chapter 2, the spectral domain Green's functions of a filament source are obtained using a recursive technique. These functions represent the system response due to a hypothetical unit source, while the response of the system due to generalized sources can be obtained using the superposition technique. In spatial domain, the Green's functions can be obtained from their spectral domain counterparts using Sommerfeld integral. Nevertheless, the numerical calculation of this integration is inefficient and time consuming since the integrands are oscillatory and slowly decaying. On the other hand, a closed form of the integration can be obtained if the spectral domain Green's functions are expressed in terms of exponentials. In order to achieve this, the discrete complex image method technique, DCIM, is adopted. Since the spectral domain Green's functions are characterized by their fast variations along the low-spectral values, while they are slowly decaying at high spectral values, a two-level DCIM is used. In the first level, sampling takes place along the high spectrum with low sampling rate; meanwhile, at the low spectrum, sampling takes place with high sampling rate. In order to avoid the poles and branch points at the low spectrum, sampling is performed along a path which deviates from the real axis around the poles and branch points of the spectral domain Green's functions. The spatial domain Green's functions are then obtained using an identity in which they are expressed as a summation of weighted Bessel functions which is dependent on the unknown propagation constant, i.e. the spectral variable that corresponds to the longitudinal direction of the plasmonic transmission line under investigation.

In chapter 3, the Method of Moments (MoM) technique is presented. The method starts by discretising the metal strips constructing the transmission line into segments whose dimensions are much smaller than the wavelength. The unknown current along the strips forming the plasmonic transmission line is expanded in terms of known basis functions with unknown weights. The choice of the basis functions is a crucial factor in determining the accuracy of the solution. For the transversal currents, they are represented by either a full roof-top or a half roof-top according to the location of the basis function. On the other hand, longitudinal currents are represented by rectangular prism basis functions. The following step is to apply a suitable testing technique. In this thesis, the razor-blade testing is adopted. At this stage the electric fields are represented in terms of the unknown propagation constant(s) and the unknown current weights. In order to obtain these unknowns, the boundary conditions are applied, where the electric field is related to the current flowing through the plasmonic strips. This results in obtaining a "*characteristic equation*", which is only function in the propagation constant(s) of the propagating mode(s). Using an iterative Müller method, all the possible propagation constants can be obtained. After calculating the propagating mode(s), the modal current distributions are obtained from the matrix equation describing the system using the singular value decomposition technique.

In chapter 4, the developed mode solver is used to calculate the propagation characteristics of several plasmonic transmission lines. The obtained results are compared to those obtained using CST for the aim of verification. In free-space, single strips of various topologies are studied including a rectangular, triangular and circular transmission lines. Additionally, multi-strip transmission lines like the horizontally and the vertically coupled strips are studied. These transmission lines allow the propagation of two modes: the *even* and the *odd* mode since they are constructed from two strips. For all the examples, the effective refractive index and the insertion losses are calculated at the frequency ranging from 150 THz – 400 THz. The obtained results are compared to CST for verification, which shows a very good agreement between them. The modal current distributions are plotted along the metallic strips. It shows that current penetration inside the metallic strips is strong, which demonstrates the significance of using volumetric current representation. This chapter also presents a study for plasmonic transmission lines placed in layered medium in which the propagation characteristics and modal current distributions are also studied. Additionally, the effect of varying the transmission line geometrical parameters on its propagation characteristics is presented. It is shown that increasing the width or the thickness of plasmonic strips leads to decreasing the effective refractive index and the propagation losses inside the plasmonic transmission lines due to the lower confinement of the modes inside the plasmonic strips.

In chapter 5, three designs of plasmonic wire-grid nano-antenna arrays are presented. The basic unit cell of these arrays is a nano-dipole which can be viewed as a finite-length plasmonic transmission line. So, before the optimization of the array, the developed MoM-based solver is used to estimate the propagation characteristics of the single nano-dipole. Afterwards, the optimization of the whole array is performed using CST. The wire-grid arrays are constructed from a number of radiators connected via orthogonal connectors. The length of each of the radiators and connectors is set to $\lambda_g / 2$ in order to achieve maximum directivity. The chapter starts with the design of a five-element wire-grid array located in free-space in order to understand well the radiation mechanism of this class of nantennas, namely wire-grid nantennas. This wire-grid radiates along the broadside direction with directivity and radiation efficiency of 9.26 dBi and 52% respectively. The low efficiency is attributed to the high losses of gold at the operating frequency. The effect of adding a substrate underneath the antenna is also studied which showed a strong impact on the radiation characteristics of the array. The second proposed array consists of eleven radiators instead of five in order to increase the directivity. To enhance the radiation efficiency, silver material is used instead of gold. In order to exclude the substrate effects on the radiation characteristics of the array and to turn the bi-directional radiation into unidirectional with double the directivity value, a finite thickness SiO_2 layer backed with silver ground plane is placed underneath the antenna. As such, any supporting substrate can be located below the ground plane without affecting the antenna radiation performance. A study for the effect of varying the antenna geometrical parameters on its gain has been presented. The optimized array has directivity, gain and efficiency of 13 dBi, 12.2 dBi, and 78.2% respectively. It is demonstrated that both arrays provide very high linear polarization purity, where the cross-polar component is almost zero. For the two previous designs, the arrays provide linear polarization since all radiators are aligned parallel to each other. The last example

considered in this chapter is a novel structure for a circularly polarized wire-grid array. It consists of a total of twelve radiators. Each six parallel aligned radiators form one group while the two groups are orthogonal to each other. The circular polarization is achieved by inserting a gap at the centre radiator of one of the two antenna groups creating a 90˚ phase difference between them. The proposed array is characterized by its relatively wide axial-ratio bandwidth, high directivity and high radiation efficiency whose values are 9.6 THz, 10.75 dBi, and 79% respectively. The last section in this chapter shows two prototypes of fabricated wire-grid arrays which are designed for operation at 400 THz. The antennas are experimentally characterized in which the transmitted power from a periodic array of wire-grids is measured. A comparison between simulations and measurements are performed which generally shows good agreement.

6.2 Future Work

This thesis included two correlated research lines. For each research line, there are a number of ideas which are considered of great interest for future work.

In the first research line, a plasmonic volumetric transmission line mode solver is developed. The developed solver analyses wave-guiding structures of any topology that are placed within a general stratified layer structure. One suggested modification is to upgrade the solver to include slot-based transmission lines. As has been shown in this thesis, only strip-based transmission lines are considered. The developed solver can calculate the propagation characteristics of slot transmission lines by assuming very wide plasmonic strips separated by gap(s) of certain dimensions. Nevertheless, this problem will take relatively long calculation time as it will require dense meshing for the wide metallic strips. On the other hand, this problem can be solved in another way in which the slot is treated like a strip which has a certain dielectric constant while the surrounding layer is the plasmonic metal. In such case, the meshing occurs inside the slot and not along the plasmonic metal layer. This will tremendously reduce the number of unknowns and save much of the calculation time. Another interesting issue is to investigate the usage of non-uniform meshing. In the presented work, uniform meshing has been considered for simplicity. However, it is noticed that currents along the strip edges is very intense compared to its centre. For uniform meshing, this means that dense mesh is essential to obtain accurate results. Consequently, this increases the number of unknowns leading to longer calculation time. To avoid this, non-uniform meshing can be considered where a finer mesh along the edges of the transmission lines compared to its centre can reduce the number of unknowns. As a result, the calculation time can be reduced. Finally, the solver can also be used in the future to study other waveguide topologies like hybrid waveguides which consists of both dielectric and metallic structures. In this case, the non-uniform mesh will be of great importance since the metallic structures will require denser mesh compared to the dielectric ones.

The second research line is concerned with the design of plasmonic nano-antenna arrays which are characterized by their high directivity. Different nano-antenna arrays were proposed which are capable of providing linear or circular polarizations. In the future, this

work can be extended to include nantennas with reconfigurable radiation pattern and/or polarization diversity properties. One way to achieve this is using graphene material, which has the superior advantage of controlling its electric conductivity by applying voltage. Therefore, it can be tuned from being a highly conductive material to a lossy one. In other words, it can be used as a switch which controls the wave propagation or attenuation along a certain direction. For antennas with radiation pattern reconfiguration capability, one suggestion is to design two antennas connected via a T-junction. Two unconnected graphene sheets will be placed underneath the two arms of this T-junction. Thus, when a voltage is applied along one of the two arms, the corresponding antenna will not radiate while the other one will radiate and vice versa. On the other hand, if no voltage is applied, both antennas will contribute to the overall radiation. For a nano-antenna with polarization diversity, two graphene sheets can be placed underneath the two groups of the proposed circularly polarized antenna array. When no voltage is applied, the antenna will provide circular polarization in a similar way as discussed in chapter 5. On the other hand, if voltage is applied across one of the two graphene sheets, the wave will propagate across one of the two antenna groups while the other group of antennas will face wave attenuation and will not radiate. Thus, a linear polarization can be obtained. It is worth mentioning that this configuration enables to obtain both vertical and horizontal linear polarization, besides the circular polarization. Since the two group of arrays are perpendicular to each other, the polarization will be determined based on the location of the applied voltage. These ideas should be studied and optimized carefully before their fabrication. Nano-antennas for other applications like sensing applications are also of great interest. The resonance location of these devices varies according to the surrounding medium. Thus, various nantenna topologies can be studied and compared in order to achieve the highest sensitivity. In addition to the design of the various nano-antennas, the fabrication of these antennas is very crucial. As noticed from chapter 6, the fabrication does not provide the exact desired topology. For example, the lengths of the rods and the round corners of the fabricated prototypes resulted in shifting the resonance locations. The sensitivity of the antenna to these differences should be studied in future work to get a feedback for the future nantenna designs. Finally, this work can further be extended to include the design of other optical devices like optical modulators, couplers, interferometers, etc. which are considered as essential components in optical communication systems.

Bibliography

[1] P. R. West, S. Ishili, G. V. Naik, N. K. Emani, V. M. Shalaev, A. Boltasseva, "Searching for better plasmonic materials," *Laser Photonics Review*, vol.4, no.6, pp.795–808, 2010.

[2] Q. Li and M. Qiu, "Plasmonic wave propagation in silver nanowires: guiding modes or not?" *Optics Express*, vol.21, no.77, pp.8587–8595, 2013.

[3] E. Ozbay, "Plasmonics: merging photonics and electronics at nanoscale dimensions," *Science*, vol.311, no.5758, pp.189– 193, 2006.

[4] G. Veronis, S. E. Kocabas, D. A. B. Miller, and S. Fan, "Modeling of plasmonic waveguide components and networks," *J. Computational Theoretical Nanoscience*, vol.6, no.8, pp.1808–1826, 2009.

[5] A. Hosseini, H. Nejati, and Y. Massoud, "Design of a maximally flat optical low pass filter using plasmonic nanostrip waveguides," *Optics Express*, vol.15, no.23, pp.15280–15286, 2007.

[6] W. L. Barnes, A. Dereux, and T. W. Ebbesen, "Surface plasmon subwavelength optics," *Nature*, vol. 424, pp. 824-830, 2013.

[7] M. L. Brongersma and P. G. Kik, *Surface Plasmon Nanophotonics*, 2007 Springer.

[8] D. M. Solis, J. M. Tabaoda, L. Landesa, J. L. Rodriguez, and F. Obelleiro, "Squeezing Maxwell's Equations into the Nanoscale," *Progress in Electromagnetics Research*, vol.154, pp.35–50, 2015.

[9] S. Maier, "Plasmonics: Fundamentals and Applications, 2007 Springer.

[10] G. A. E. Vandenbosch, "On the use of the method of moments in plasmonic applications," *Radio Science*, vol.46, no.5, 2011.

[11] G. Veronis and S. Fan, "Modes of subwavelength plasmonic slot waveguides," *IEEE Journal of Lightwave Technology*, vol.25, no.9, pp.2511–2521, 2007.

[12] D. F. P. Pile, D. K. Gramotnev, M. Haraguchi, T. Okamoto, and M. Fukui, "Numerical analysis of coupled wedge plasmons in a structure of two metal wedges separated by a gap," *Journal of Applied Physics*, vol.100, no.1, pp.013101, 2006.

[13] T. Holmgaard and S. I. Bozhevolnyi, "Theoretical analysis of dielectric-loaded surface plasmon-polariton waveguides," *Physical Rview B*, vol.75, no.24, pp.245405, 2007.

[14] T. T. Minh, K. Tanaka, and M. Tanaka, "Complex propagation constants of surface plasmon polariton rectangular waveguide by method of lines," *Optics Express*, vol.16, no.13, pp.9378–9390, 2008.

[15] H. Giefers, C. Plessl, and J. Forstner, "Accelerating finite difference time domain simulations with reconfigurable dataflow computers," *in Proceedings of 4th International Symposium on*

Highly-Efficient Accelerators and Reconfigurable Technologies, pp.33–38, Edinburgh, Scotland, UK, 2013.

[16] J. Hoffmann, C. Hafner, P. Leidenberger, J. Hesselbarth, and S. Burger, "Comparison of electromagnetic field solvers for the 3D analysis of plasmonic nano-antennas," *Proc. SPIE*, vol.7390, pp.73900J, 2009.

[17] J. M. Taboada, J. Rivero, F. Obelleiro, M. G. Araújo, and L. Landesa, "Method-of-moments formulation for the analysis of plasmonic nano-optical antennas," *Journal of Optical Society of America A*, vol.28, no.7, pp.1341–1348, 2011.

[18] A. M. Kern and O. J. F. Martin, "Modeling near-field properties of plasmonic nanoparticles: a surface integral approach," *Proc. SPIE*, vol.7395, no.739518, pp.739518, 2009.

[19] E. A. Soliman, G. A. E. Vandenbosch, E. Beyne, and R. P. Mertens, "Full-wave analysis of multiconductor multislot planar guiding structures in layered media," *IEEE Transaction on Microwave Theory and Techniques*, vol.51, no.3, pp.874–886, 2003.

[20] A. Gholipour, R. Faraji-Dana, G. A. E. Vandenbosch, and S. Safavi-Naeini, "Surface impedance modeling of plasmonic circuits at optical communication wavelengths," *IEEE Journal of Lightwave Technology*, vol.31, no.20, pp.3315–3322, 2013.

[21] M. Fuluhara, M. Ota, T. Aihara, H. Sakai, Y. Ishii, and M. Fukuda, "Surface-Plasmon Waveguides as Transmission Lines for Optical signal and Electrical Bias," *IEEE Journal of Lightwave Technology*, vol.32, no.23, pp.4490–4495, 2014.

[22] W. Park, "Optical interactions in plasmonic nanostructures," *Nano convergence*, vol.1, no.2, pp.1–27, 2014

[23] H. Wei and H. Xu, "Nanowire-based plasmonic waveguides and devices for integrated nanophotonic circuits," *Nanophotonics*, vol.1, no.2, pp.155–169, 2012.

[24] T. Srivastava and A. Kumar, "Propagation characteristics of channel plasmon polaritons supported by a dielectric filled trench in a real metal," *Journal of Applied Physics*, vol.106, no.4, pp. 043104, 2009.

[25] J. Park, K.-Y. Kim, I.-M. Lee, H. Na, S.-Y. Lee, and B. Lee, "Trapping light in plasmonic waveguides," *Optics Express*, vol.18, no.2, pp.598–623, 2010.

[26] I. E. Hashem, N. H. Rafat, and E. A. Soliman, "Dipole nantennas terminated by traveling wave rectifiers for ambient thermal energy harvesting," *IEEE Transaction on Nanotechnology*, vol.13, no.4, pp.767–778, 2014.

[27] K. Leosson, T. Nikolajsen, A. Boltasseva, and S. I. Bozhevolnyi, "Long-range surface plasmon polariton nanowire waveguides for device applications," *Optics Express*, vol.14, no.1, pp.314–319, 2006.

[28] S. I. Bozhevolnyi, "Plasmonic waveguides: challenges and opportunities," *Optical Fiber Communication Conference and Exposition and the National Fiber Optic Engineers Conference*, Los Angeles, CA, USA, 2012.

[29] X. Sun, M. Z. Alam, J. S. Aitchison, and M. Mojahedi, "Comparison of confinement and loss of plasmonic waveguides," *IEEE Photonics Conference (IPC)*, pp.618–619, Burlingame, CA, USA, 2012.

[30] A. R. Camara, P. M. P. Gouvêa, A. C. M. S. Dias, A. M. B. Braga, R. F. Dutra, R. E. de Araujo, and I. C. S. Carvalho, "Dengue immunoassay with an LSPR fiber optic sensor," *Optics Express*, vol.21, no.22, pp.27023–27031, 2013.

[31] S. Park and S. H. Song, "Polymeric variable optical attenuator based on long range surface plasmon polaritons," *Electronics Letters*, vol.42, no.7, pp.402–404, 2006.

[32] F. Liu, Y. Rao, X. Tang, R. Wan, Y. Huang, W. Zhang, and J. Peng, "Hybrid three-arm coupler with long range surface plasmon polariton and dielectric waveguides," *Applied Physics Letters*, vol.90, no.24, pp.241120, 2007.

[33] J. Lee, F. Lu, and M. A. Belkin, "Broadly wavelength tunable bandpass filters based on long-range surface plasmon polaritons," *Optics Letters*, vol.36, no.19, pp. 3744–3746,2011.

[34] T. Nikolajsen, K. Leosson, and S. I. Bozhevolnyi, "Surface plasmon polariton based modulator and switches operating at telecom wavelengths," *Applied Physics Letters*, vol.85, no.24, pp.5833, 2004.

[35] D. Dai and S. He, "A silicon-based hybrid plasmonic waveguide with a metal cap for a nano-scale light confinement," *Optics Express*, vol.17, no.19, pp.16646–16653, 2009.

[36] Y. Zhao, "Optical Nanoantennas and their applications", *IEEE Radio and Wireless Symposium*, pp.58–60, 2013.

[37] G. A. E. Vandenbosch, and Z. Ma, "Upper bounds for the solar energy harvesting efficiency of nano-antennas," *Nano energy*, vol.1, no.3, pp.494–502, 2012.

[38] M. F. Garcia-Parajo, "Optical antennas focus in on biology," *Nature Photonics*, vol.2, no.4, pp.201–203, 2008.

[39] C. D'Andea, J. Bochterle, A. Toma, C. Huck, F. Neubrech, E. Messina, B. Fazio, OM. Marago. E. Di Fabrizio, M. L. de La Cahpalle, P. G. Gucciardi, and A. Pucci, "Optical Nanoantennas for Multibans Surface-Enhanced Infrared and Raman Spectroscopy," *ACS Nano*, vol.7, pp.3522–3531, 2013.

[40] M. Castro-Lopez, N. de Sousa, A. Garcia-Martin, F. Y, Gardes, and R. Sapienza, "Scattering of a plasmonic nanoantenna embedded in a silicon waveguide," *Optics Express*, vol.23, pp.28108–28118, 2015.

[41] P. Bharadwaj, B. Deutsch, and L. Novotny, "Optical antennas," *Advances in Optics and Photonics*, vol.1, pp.438–483, 2009.

[42] S. M. Kandil, T. Ali, S. Sedky, and E. A. Soliman, "Highly sensitive mushroom-shaped gold-silica nano-antenna array for refractive index sensing,"*10th European Conference on Antennas and Propagation*, 2016.

[43] M. Donelli, "Design of broadband metal nanosphere antenna arrays with a hybrid evolutionary algorithm," *Optics Letters*, vol.38, no.4, pp.401–403, 2013.

[44] G. W. Hanson, "Radiation efficiency of nano-radius dipole antennas in the microwave and far-infrared regimes," *IEEE Antennas and Propagation Magazine*, vol.50, no.3, pp.66–77, 2008.

[45] E. Cubukcu, N. Yu, E. J. Smythe, L. Diehl, K. B. Crozier, and F. Capasso, "Plasmonic laser antennas and related devices," *IEEE Journal of Selected Topics in Quantum Electronics*, vol.14, no.6, pp.1448–1461, 2008.

[46] L. Zou, W. Withayachumnankul, C. M. Shah, A. Mitchell, M. Bhaskaran, S. Sriram, and C. Fumeaux, "Dielectric resonator nanoantennas at visible frequencies," *Optics Express*, vol.21, no.1, pp.1344–1352, 2013.

[47] L. Y. Wu, B. M. Ross, and L. P. Lee, "Optical properties of the crescent-shaped nanohole antenna," *Nano letters*, vol.9, no.5, pp.1956–1961, 2009.

[48] P. Biagioni, J. S. Huang, L. Duò, M. Finazzi, and B. Hecht, "Cross resonant optical antenna," *Physical Review Letters*, vol.102, no.25, pp.256801, 2009.

[49] L. Novotny, and N. Van Hulst, "Antennas for light," *Nature Photonics*, vol.5, pp.83-90, 2011.

[50] C. D. Stanciu, F. Hansteen, A. V. Kimel, A. Kirilyuk, A. Tsukamoto, A. Itoh, and T. Rasing, "All-optical magnetic recording with circularly polarized light," *Physical Review Letters*, vol.99, pp. 047601, 2007.

[51] K. Vahaplar, A. M. Kalashniknova, A. V. Kimel, D. Hinzke, U. Nowak, R. Chantrell, A. Tsukamoto, A. Itoh, A. Kirilyuk, and T. Rasing, "Ultrafast path for optical magnetization reversal via a strongly nonequilibrium state," *Physical Review Letters*, vol.103, pp.117201, 2009.

[52] S. L. Neale, M. P. MacDonald, K. Dholakia, and T. F. Krauss, "All-optical control of microfluidic components using form birefringence," *Nature Materials*, vol.4, pp.530–533, 2005.

[53] J. M. Kikkawa, and D. D. Awschalom, "All-optical magnetic resonance in semiconductors," *Science*, vol.287, pp.473–476, 2000.

[54] E. Ogut, and K. Sendur, "Tuning the polarization states of optical spots at the nanoscale on the poincare' sphere using plasmonic nanoantenna," *Applied Physics A*, vol.103, no.3, pp.855–858, 2011.

[55] X. Peng, N. Komatsu, S. Bhattachary, T. Shimawaki, S. Aonuma, T. Kimura, and A. Osuka, "Optically active single-walled carbon nanotubes," *Nature Nanotechnology*, vol.2, pp.361–365, 2007.

[56] Y. Ohdaira, T. Inoue, H. Hori, and K. Kitahara, "Local circular polarization observed in surface vortices of optical near-fields," *Optics Express*, vol.16, no.5, pp.2915–2921, 2008.

[57] A. Drezet, C. Genet, and T. W. Ebbesen, "Miniature plasmonic wave plates," *Physical Review Letters*, vol.101, no.4, pp.043902, 2008.

[58] T. Li, H. Liu, S.-M. Wang, X.-G. Yin, F.-M. Wang, S.-N. Zhu, and X. Zhang, "Manipulating optical rotation in extraordinary hybrid plasmonic excitations," *Applied Physics Letters*, vol.93, no.2, pp.021110, 2016.

[59] M. H. El Sherif, M. H. Bakr, and E. A. Soliman, "E-shaped wideband plasmonic nantennas with linear and dual-linear polarizations," *Optics Express*, vol.3, no.4, pp.140–145, 2015.

[60] L. Yousefi, and A. C. Foster, "Waveguide-fed optical hybrid plasmonic patch nano-antenna," *Optics Express*, vol.20, no.16, pp.18326–18335, 2012.

[61] G. N. Malheros-Silveira, G. S. Wiederhecker, and H. E. Hernandez-Figueroa, "Dielectric resonator antenna for applications in nanophotonics," *Optics Express*, vol.21, no.1, pp.1234–1239, 2013.

[62] E. Ogut, G. Kiziltas, and K. Sendur, “Circularly polarized localized near-field radiation at the nanoscale,” *Applied Physics B*, vol.99, no.1, pp.67–74, 2009.

[63] D. Lin, and J.-S. Huang, “Slant-gap plasmonic nanoantennas for optical chirality engineering and circular dichroism enhancement,” *Optics Express*, vol.22, no.7, pp.7434–7445, 2014.

[64] E. S. Unlu, R. U. Tok, K.Sendur, “Broadband plasmonic nanoantenna with an adjustable spectral response,” *Optics Express*, vol.19, no.2, pp.1000–1006, 2011.

[65] S. Halawa, “Green’s functions of generalized sources in plasmonic layered media,” *M.Sc. Thesis*, The American University in Cairo, Egypt (2014).

[66] K. Li, “General full-wave Green’s functions in spectral domain for arbitrarily multilayered dielectric media,” *IEEE International Microwave Symposium*, 1997.

[67] K. A. Michalski, “Missing boundary conditions of electromagnetics,” *Electronics Letters*, vol.22, pp.921–922, 1986.

[68] F. Demuynck, G. A. E Vandenbosch, A. Van de Capelle, “The expansion wave concept, part I: efficient calculation of spatial Green's functions in a stratified dielectric medium,” *IEEE Transactions on Antennas and Propagation*, vol.46, pp.397-406, 1998.

[69] C. –U.G. Hsu, R. F. Harrington, K. A. Michalski, ans D. Zheng, “Analysis of multiconductor transmission lines of arbitrary cross section in multilayered uniaxial media,” *IEEE Transactions on Microwave Theory and Techniques*, vol.41, no1, pp.70-78, 1993.

[70] M. Vrancken and G. A. E. Vandenbosch, “Semantics of dyadic and mixed potential field representation for 3-D current distributions in planar stratified media,” *IEEE Transaction on Antennas and Propagation*, vol.51, no.10, pp. 2778–2787, 2003.

[71] E. A. Soliman and G. A. E. Vandenbosch, “Green's functions of filament sources embedded in stratified dielectric media,” *Progress in Electromagnetics Research*, Vol. 62, 21-40, 2006.

[72] W. C. Chew, *Wave and Fields in Inhomogeneous Media*, IEEE Press, 1995.

[73] Sommerfeld, A., *Partial Differential Equations in Physics*, Academic, New York, 1949.

[74] C-I G. Hsu, R. F. Harrington, K. A. Michaliski, and D. Zheng, “Analysis of multiconductor transmission lines of arbitrary cross section in multi-layered uni-axial media,” *IEEE Transaction in Microwave Theory and Techniques*, vol.MTT-41, pp.70-78, 1993.

[75] E. A. Soliman, “Planar microwave structure in layered media: full-wave analysis, design, and characterization,” *Ph.D. Dissertation*, Katholieke Universteit Leuven, Belgium (2000).

[76] Gradshteyn, I. S. And I. M. Ryzhik, *Table of Integrals, Series and Products*, Academic Press, 1980.

[77] Mahmoud, S. F. and A. Mohsen, "Assessment of image theory for field evaluation over a multi-layer earth," *IEEE Trans. Antennas Propagat.*, Vol. 33, 1054-1058, 1985.

[78] Chow, Y. L., J. J. Yang, and G. E. Howard, "Complex images for electrostatic field computation in multilayered media," *IEEE Trans. Microwave Theory Tech.*, Vol. 39, 1120-1125, 1991

[79] Yang, J. J., Y. L. Chow, and D. G. Fang, "Discrete complex images of a three-dimensional dipole above and within a lossy ground," *IEE Proc. Pt. H.*, Vol. 138, 319-326, 1991.

[80] Y. Hua, and T. Sarkar, "Generalized Pencil-of-Function Method for extracting Poles of an EM System from its Transient Response," *IEEE Transaction on Antennas and Propagation*, vol.37, pp.229–234, 1989.

[81] Y. L. Chow, J. J. Yang, D. G. Fang, and G. E. Howard, "A closed-form spatial Green's function for the thick microstrip substrate," *IEEE Transaction on Antennas and Propagation*, vol.39, no. 3, pp.588–592, 1991.

[82] E. Soliman, P. Pieter, E. Beyn, and G. Vandenbosch, "Numerically efficient spatial domain moment method for multislot transmission lines in layered media – Application to multislot lines in MCM-D technology, "*IEEE Transactions on Microwave Theory and Techniques*, vol.47, pp.1782–1787, 1999.

[83] M. Aksun, "A robust approach for the derivation of closed-form Green's functions," *IEEE Transaction on Microwave Theory Technology*, vol.44, pp.651–658, 1996.

[84] E. A. Soliman, G. A. E. Vandenbosch, and E. Beyne, "Galerkin versus razor-blade testing in the method of moments formulation for multi-conductor transmission line," *International Journal of RF and Microwave computer-aided engineering*, vol.10, pp.132–138, 2000.

[85] E. A. Soliman, "Semi-analytical calculation for sensitivities of the method of moments impedance and excitation matrices," RF and Microwave Computer-Aided Engineering, vol.17, no.9, 2007.

[86] M. O. Sallam, G. Gielen, G. A. E. Vandenbosch, and E. A. Soliman, "Integral equations formulation of plasmonic transmission lines," *Optics Express*, vol.22, no.19, pp.22388–22402, 2014.

[87] M. O. Sallam, G. Gielen, G. A. E. Vandenbosch, and E. A. Soliman, "Plasmonic transmission line mode solver based on the method of moments," *5th European Conference on Antennas and Propagation*, pp.1–5, 2015.

[88] S. D. Conte and C. de Boor, *Elementary Numerical Analysis: An algorithmic Approach* (McGraw-Hill, 1990).

[89] MATLAB, version 7.9.0. Natick, Massachusetts: The MathWorks Inc., 2009.

[90] G. E. Stewart, "On the early history of the singular value decomposition," SIAM Review, vol.35, no.4, pp.551–566, 1993.

[91] P. R. West, S. Ishii, G. V. Naik, N. K. Emani, V. M. Shalaev, and A. Boltasseva, "Searching for better plasmonic materials," *Laser Photonics Review*, vol.4, no.6, pp.795–808, 2010.

[92] CST Microwave Studio, 2012. www.cst.com

[93] F. Wooten, *Optical Properties of Solids*, Academic Press, 1972, Chap.3.

[94] E. A. Soliman, S. Brebels, G. A. E. Vandenbosch, and E. Beyne, "Antenna arrays in MCM-D technology fed by coplanar CPW networks," *IEEE Transactions on Microwave Theory and Techniques*, vol.48, pp.1065–1068, 2000.

[95] C. A. Balanis, *Antenna Theory: Analysis and Design*, John Wiley & Sons, 2005.

[96] F. Pelayo Garcia de Arquer, V. Volski, N. Verellen, G. A. E. Vandenbosch, and V. V. Moshchalkov, "Engineering the input impedance of optical nano dipole antennas: materials, geometry and excitation effect," *IEEE Transactions on Antennas and Propagation*, vol.59, pp.3144–3153, Sept. 2011.

[97] I. Hanninen, M.Taskinen, and J. Sarvas, "Singularity subtraction integral formula for surface integral equations with RWG, rooftop and hybrid basis functions," *Progress In Electromagnetics Research*, vol.63, pp.243–278, 2006.

[98] E. A. Soliman, M. O. Sallam, and G. A. E. Vandenbosch, "Plasmonic grid array of gold nanorods for point-to-point optical communications," *IEEE Journal of Lightwave Technology*, vol.32, no.24, pp.4296-4302, 2014.

[99] E. A. Soliman, M. O. Sallam, and G. A. E. Vandenbosch, "Novel wire-grid nantenna array for optical communication systems," *International Workshop on Antenna Technology*, pp.109-112, 2013.

[100] E. A. Soliman, S. Hassan, O. El Katteb, M. O. Sallam, M. Serry, and S. Sedky, "77-GHz MEMS brick-wall antenna fed by coupled microstrip lines," *International Symposium on Antennas and Propagation Society (APSURSI)*, pp. 1–4, 2010.

[101] R. Conti, J. Toth, T. Dowling, and J. Weiss, "The wire grid microstrip antenna," *IEEE Transactions on Antennas and Propagation*, vol.29, pp.157–166, 1981.

[102] M. O. Sallam, E. A. Soliman, and S. Sedky, "Novel linearly and circularly polarized 60 GHz MEMS antennas on low- and high- resistivity silicon," *5th European Conference on Antennas and Propagation*, pp. 1194–1198, 2011.

[103] R.-L. Li, V. F. Fusco, "Circularly polarized twisted loop antenna," *IEEE Transactions on Antennas and Propagation*, vol.50, no.10, pp.1377–1381, 2003.